LIÈGE université
Sciences

Thermally and dynamically driven magnetic flux penetration in type-II superconductors

Sylvain Blanco Alvarez

University of Liège, Faculty of Sciences

CESAM Research Unit, Q-MAT Center

Experimental Physics of Nanostructured Materials

Liège 2020

Thermally and dynamically driven magnetic flux penetration in type-II superconductors

Experimental Physics of Nanostructured Materials,
Q-MAT Center, CESAM Research Unit,
Faculty of Sciences, University of Liège

Jury:
Prof. Dr. Ir. N. D. Nguyen (Chairman, ULiège)
Prof. Dr. S. Dorbolo (Secretary, ULiège)
Dr. A. Palau (ICMAB-CSIC, Spain)
Dr. M. Menghini (Instituto IMDEA Nanociencia, Spain)
Dr. J. Brisbois (Centre Spatial de Liège, ULiège)
Prof. Dr. S. Melinte (Co-supervisor, UCLouvain)
Prof. Dr. A. V. Silhanek (Supervisor, ULiège)

Dissertation presented in partial
fulfilment of the requirements for the
degree of Doctor in Science by
Sylvain Blanco Alvarez

October 2020

Abstract

Superconductors have the fantastic abilities to spark the interest of people from numerous and varied backgrounds, from theoretical physicists to applied engineers. On the one hand, it constitutes one of the few systems exhibiting quantum properties at the macroscopic scale, the structural electronic conditions for a material to possess such a phase staying partially unknown. On the other hand, this macroscopic quantum state allows for applications such as dissipationless electrical current transport, production of strong magnetic fields largely exceeding those generated by permanent magnets, creation of the finest detectors of magnetic fields or of single-photon detectors, to name but a few.

In the intermediate scale, resulting from the quantum nature of superconductors and explaining the behaviour of macroscopic superconducting circuitry is the vortex. Vortices are magnetic flux quanta present in most of the technologically relevant superconductors and ruling their electromagnetic response. It is therefore of direct interest to study the behaviour of these entities not only for applications but also as a realization of a multi-particle system of fundamental interest in physics. Vortex physics in superconductors can be approached from a number of angles, from the dynamics of a single vortex to the collective motion of hundreds of thousands of them.

The present thesis concentrates on the macroscopic response of vortex bundles and studies two of the possible scenarios of vortex penetration in superconductors. The first, called dynamically driven magnetic flux penetration, is a smooth reorganization of the vortex landscape, akin to the motion of sand grains when adding new grains on a pile. The second, named thermally driven magnetic flux penetration, is a much more violent phenomenon resembling the physics of dielectric breakdown. The experimental technique of choice for revealing these regimes is the magneto-optical imaging, allowing to translate local variations of magnetic field is rotation of light polarization. Using magneto-optical imaging, we observe the magnetic landscape in thin film superconducting samples and analyze the spatially resolved vortex pattern to answer questions about both types of phenomena and their interactions.

For dynamically driven flux penetration, critical state models or Maxwell based finite element methods are able to predict broadly the landscape resulting from an externally applied magnetic field. Contrary to a normal conductor, any defect present at the edge of a superconducting sample can have a perturbing effect on

scales comparable to the size of the sample. Recent experimental studies of these perturbations on micro-indented Nb films showed a discrepancy between the predicted and the actual landscapes. In order to further investigate the origin of this discrepancy, we study YBCO films with various micro-indentations geometries and show that contrary to the Nb case, critical state models are able to accurately predict the influence of border indentations. We associate this contrasting difference in behaviour to the role of surface barriers, neglected in both the critical state models and the Maxwell based simulations.

In the second part, we study the statistical properties of magnetic flux penetration in Nb films. We show the possibility to discriminate between dynamically driven and thermally driven flux motions using magneto-optical imaging despite the technique's inability to pick up thermal differences and without the need to invoke time-resolved measurements. Having separated both types of phenomena, we show the existence of preferential nucleation spots for thermal events and point out an unexpected anti-correlation with the loci where dynamical events take place. We show the fundamental difference between both flux reorganizations by looking at the size distribution associated with each of them. While we recover the expected power law between the size and the probability of occurrence associated with self-organized criticality from the dynamically driven vortex motion, the thermally driven part creates a clear deviation from this trend by adding a second mode to the distribution. The visual resemblance of thermally driven vortex motion with Lichtenberg figures obtained during dielectric breakdown invite us to consider the problem from the point of view of breakdown phenomena. In fact, the repeatable nature of the experiment provides the possibility of infinite repetitions of the breakdown on a single sample, completely discarding the sample-to-sample spread typical for these kind of measurements. We conclude that the remaining spread is associated with competing nucleating points each having their own thresholds. Finally, observing the evolution of this threshold with temperature, we correlate the well-known change of morphology with the transition between two distinct types of events, each occurring at separate magnetic thresholds. We are convinced that the findings reported here may transcend the domain of superconducting systems to reach other disciplines involving catastrophic effects and reliability tests.

Résumé

Les supraconducteurs ont la fantastique capacité d'éveiller la curiosité des scientifiques, depuis les physiciens théoriciens jusqu'aux ingénieurs. Pour les uns, ils constituent l'un des rares systèmes montrant des propriétés quantiques à l'échelle macroscopique, les structures électroniques sous-jacentes nécessaires à leur existence restant partiellement mystérieuses. Pour les autres, cet état macroscopique permet des applications telles que le transport de courant sans perte, la production de fort champs magnétiques excédant largement ceux générés par les aimants permanents, la création des détecteurs de champs magnétiques les plus sensibles et de détecteurs de photon unique pour ne citer qu'une partie des applications possibles.

Entre ces deux visions, résultant directement de la nature quantique du supraconducteur et expliquant le comportement de circuits supraconducteurs macroscopiques, se trouve le vortex. Les vortex sont des quanta de champ magnétique présent dans la plupart des applications technologiques utilisant des supraconducteurs, gouvernant la réponse magnétique desdites applications. Il est donc d'un intérêt évident d'étudier le comportement de ces entités, tant pour des applications concrètes que comme la réalisation d'un système multi-particules, d'intérêt fondamental en physique. La physique des vortex peut s'aborder selon plusieurs points de vue, allant de la dynamique d'un simple vortex jusqu'au comportement collectif de milliers d'entre eux.

La présente thèse s'intéresse à la réponse macroscopique de groupes de vortex en étudiant deux scénarios possibles pour leur réorganisation dans un supraconducteur. Le premier cas, appelé réorganisation dynamique de la pénétration de flux magnétique, est une réorganisation douce du paysage de vortex, s'apparentant aux mouvements de grains de sable empilés lorsque l'on viendrait les saupoudrer de nouveaux grains. Le deuxième, appelé réorganisation thermique de la pénétration de flux magnétique, est un phénomène beaucoup plus violent, ressemblant plus à la physique de phénomènes tels que le claquage diélectrique. La technique expérimentale de choix pour observer ces deux régimes est l'imagerie magnéto-optique, permettant de traduire les variations locales de champ magnétique en rotation du plan de polarisation d'une lumière incidente. En utilisant cette technique d'imagerie magnéto-optique, nous observons le paysage magnétique de fins échantillons supraconducteurs et analysons les motifs de vortex associés afin de répondre aux questions concernant les deux types de phénomènes et leurs interac-

tions.

Concernant la réorganisation dynamique de flux, les modèles d'état critique ou les simulations par éléments finis basées sur les équations de Maxwell permettent de prédire grossièrement le paysage résultant de l'application d'un champ magnétique externe. Contrairement à un conducteur classique, chaque défaut présent à la surface du supraconducteur peut créer une perturbation s'étendant sur des échelles comparables à la taille de l'échantillon. De récentes études expérimentales sur les perturbations dans des films de Nb avec micro-indentations ont montré un décalage entre les prédictions et les paysages magnétiques réels. Afin de poursuivre les investigations concernant les origines de ce décalage, nous étudions des films de YBCO possédant des micro-indentations de géométries variées et montrons que contrairement au cas du Nb, les modèles d'état critique sont capables de reproduire précisément l'influence de ces indentations. Nous associons cette différence marquée de comportement au rôle des barrières de surface, négligées tant par les modèles d'état critique que par la plupart simulations basées sur les équations de Maxwell.

Dans un second temps, nous étudions les propriétés statistiques de la pénétration de flux magnétique dans des films de Nb. Nous montrons la possibilité de discriminer les réorganisations de flux dynamiques de celles thermiques malgré l'insensibilité de la magnéto-optique aux différences thermiques et sans avoir accès à l'évolution en temps réel des réorganisations. Après séparation des deux types de phénomènes, nous montrons l'existence de lieux préférentiels de nucléations pour les évènements thermiques et mettons en avant l'anti-correlation inattendue des lieux de nucléations thermiques et dynamiques. Nous montrons la différence fondamentale entre les deux types de réorganisation en observant leur distribution en taille. Bien que, pour la réorganisation dynamique, nous retrouvions la loi de puissance attendue entre la taille et la probabilité d'occurrence, caractéristique des phénomènes de criticalité auto-organisée, la réorganisation thermique crée une claire déviation de cette tendance en ajoutant un second mode à la distribution. La ressemblance visuelle du déplacement thermique de vortex avec les figures de Lichtenberg obtenues lors de claquages diélectriques nous invite à considérer le problème du point de vue des phénomènes de rupture. En fait, la nature réitérable de l'expérience nous fournit la possibilité d'une infinité de répétitions d'une rupture sur un échantillon unique, évitant ainsi la dispersion naturelle de ce genre de mesures due aux différences inter-échantillons. Nous concluons que la dispersion observée est associée aux différents sites de nucléations, chacun possédant un seuil de déclenchement propre. Enfin, en observant l'évolution de ce seuil de déclenchement lors d'une augmentation de température, nous corrélons le changement attendu de morphologie à la transition entre deux types distincts d'évènements ayant chacun son propre seuil magnétique. Nous sommes convaincu que les résultats exposés ici peuvent s'appliquer plus vastement qu'au seul domaine des systèmes supraconducteurs et sont d'intérêt pour d'autres domaines où les phénomènes de ruptures et les tests de résistance sont pertinents.

Acknowledgement

As a wise man once said, there is no such thing as a self-made man. In the same manner, this thesis could not have been here without the help of a lot of people that need acknowledgement.

First, I would like to thank the FNRS for financing the project my PhD thesis was part of, immersing me in four years of scientific discussions.

I would like to express my gratitude to the jury for taking the time to review my thesis and assisting to my defense in this troubled year.

I would like to thank Roman Kramer (Université Grenoble Alpes) for the Nb samples needed during my thesis, be it the sample presented here or the others, necessary for the peregrinations along the way. Thanks also to Anna Palau (ICMAB-CSIC) for the YBCO films used in this manuscript.

Some of the measurements presented here were made in São Carlos in the group of Wilson Ortiz. I am grateful for his invitation that turned into a fantastic experience thanks to his hospitality and to the help of Maycon Motta, Lincoln Pinheiro, and Otávio Pedroso both inside and outside the lab. All of them left me no choice but to conclude that Brazilian people are amongst the nicest colleagues one could hope for.

In less exotic setting, I would like to thank my Belgian colleagues, Jonathan, Gorky, Žjelko, Xavier, Joseph, Jérémy, Simon, Émile, Thomas, Sunil, François, Naama and Stefan. Thanks for what you taught me in the lab and outside, the insightful discussions, the proofreading, the discrete repair of VIVALDI on the day prior to its presentation, and of course, the coffee and ice cream. Thank you to Loïc Burger and Benoit Vanderheyden for their discussions, their expertise, and the insights provided by their simulations.

My deepest thanks to my supervisor and co-supervisor, Alejandro Silhanek and Sorin Melinte. They both took the time to provide feedback and constructive criticism of my work during this PhD. It is easy to get lost in the stormy sea of scientific papers and the daily advice from Alejandro Silhanek and our discussions showed me what science should strive for.

Completing this thesis was as much thanks to support from colleagues than from family and friends. Despite the clear overlap of both sets, I would like to thanks specifically Antoine, Ludivine, Marie-Julie, Élodie and Jérémy for the adventures they bring into my life.

Thank you to my family for their continuous support, my brothers for our

dinner discussions and my parents for enduring them. Thank you also to my in-laws for their support.

Finally, for supporting me, bringing me motivation, for making me dream but also for now knowing entirely too much about superconductivity, I can only attempt to thank you enough Clémentine.

Contents

List of Figures

Chapter 1

Introduction

Observed for the first time in 1911 by H. K. Onnes [1] in a feat of experimental physics, superconductivity grew from the unexplained zero electrical resistivity in mercury at low temperature to a coherent quantum theory in just 46 years. Following these first electrical measurements, W. Meissner and R. Ochsenfeld [2] realized that upon transitioning into a superconductive state, materials would also acquire a perfect diamagnetic behaviour. Opting for a pratical approach, H. and F. London described the electromagnetic response of a superconductor by complementing Maxwell's laws with a constitutive relation able to fit both the perfect conductivity and the expulsion of magnetic field inside the superconductor [3]. Although entirely phenomenological, this simple model is still relevant for the modelisation of magnetic and electric fields as a first approximation of superconductor/magnetic field interaction. Realizing that the expulsion of magnetic field was the sign of a phase transition, V. L. Ginzburg and L. Landau used a thermodynamical approach to formulate their theory in terms of an order parameter representing the density of superconducting electrons near the transition temperature [4]. The last stroke came in 1957 from J. Bardeen, L. Cooper and J. R. Schrieffer [5] with a many-body quantum mechanic microscopic description known as the BCS theory generalizing both London theory and Ginzburg-Landau theory. Understanding that contrary to the conventional independent electrons model, electrons inside a material superconducting material can undergo an attractive force between them is the key insight from this theory. At low enough temperature, this attractive force allows two electrons to pair up into a bosonic Cooper pair, which condensate into their lower energy state, similar to Bose-Einstein condensation in cold atoms physics. BCS theory proved to be rather successful in explaining most of metallic superconductors until 1987 when A. Müller and G. Bednorz [6] discovered the first high temperature superconductors. From then on, with the dream of room temperature superconductors, fundamental research flourished and the observation of unconventional superconducting condensates such as iron based superconductors [7], heavy fermions [8] or metastable superconductivity [9] continue to reveal new secrets of these strongly correlated electronic systems.

In parallel to these new discoveries, the already well established low temperature superconductors where progressively mastered and incorporated in technologically relevant applications, from NMR scanners in hospitals to particle accelerators. With the advent of nanotechnology, applications of superconductors saw their size shrink so as to confine the condensate to lower dimensionalities. The reduced dimensions of superconducting systems allows researchers to probe new phenomena including the predicted increase in critical temperature in Al thin films surface superconductivity [10,11] or electric field effects in 2D superconductors [12,13]. In addition to pure research, these thin films configurations are of great industrial interest. From YBCO-coated conductors [14] to MgB_2 coated Nb microwave cavity sustaining up to 2700 Oe [15], superconductors are regularly used in low loss, low noise applications. In quantum technologies, superconducting nanowire single-photon detectors with high detection efficiency and extremely high (<3 ps) temporal resolution are an emerging technology in quantum optical communication [16, 17] while Josephson junctions are used as scalable physical realisations of quantum bits [18].

In superconducting applications, the interaction between superconductors and magnetic field past the perfect diamagnetic phase is central to the physics of the device. The vast majority of technologically relevant superconducting materials belong to the so called type-II superconductors, a family in which minimizing the free energy of the system in the presence of a high enough magnetic field requires the penetrating field to be split down to single quanta of magnetic flux called vortices. It is this granular way of entering the superconductor that gives the material its peculiar properties, allowing the previously mentioned technological applications. Hence, studying the mechanism delaying or guiding their motion is of primary importance for continuous improvement of superconducting technologies.

Vortex penetration can be coarsely divided into dynamically driven and thermally driven flux penetration. In the former case, the heat generated by the motion of a vortex is dissipated quickly enough so that the system can be considered in a nearly isothermal state even during flux motion. By contrast, for thermally driven flux penetration, heat removal is too slow to ensure the full recovery of the superconducting condensate between two consecutive vortex reorganization. This create a positive gain feedback loop where magnetic flux penetration is increased locally due to the heated wake of preceding vortices.

As mentioned in the first paragraph, two macroscopical approaches are used to describe the interaction of superconductors with magnetic fields and therefore describe vortex motion. The thermodynamical approach, or generalized time-dependent Ginzburg Landau (gTDGL) model, is able to reproduce features of the condensate to sizes comparable to the coherence length $\xi(T)$ of the material (for the superconductors studied in this thesis, $\xi(0) = 1.4$ nm in YBCO, $\xi(0) = 38$ nm in Nb), modelling vortex by vortex, the effect of magnetic field on the superconducting condensate. The computational downside of this technique lies in the required minimum meshing to compute a valid solution. Since points must be spaced by $\Delta x \leq \xi/3$ [19], it is confined to local computation of the supercon-

ducting condensate over micrometric regions. Moreover, representing a realistic pinning landscape in the superconductor at this scale is not trivial as it depends on uncontrollable defects occurring during the deposition process. The electrodynamical approach consisting in solving London's equations is far more scalable. As these equations are of macroscopical nature, the solutions provided reflect an average of the magnetic field, reminiscent of a mean field approach. This allows for bigger spatial steps in simulations (typically Δx >100 nm) to the detriment of the local behaviour of individual vortices. Lacking the runaway feedback loop that intensify local differences, dynamically driven magnetic field penetration is easier to model using the electrodynamical approach. However, even for relatively simple geometries such as indented samples, theoretical predictions and experimental data do not match [20]. For thermally driven flux penetrations, the exact parameters influencing their nucleation are still unclear [21]. Moreover, the interaction between both types of flux penetrations as well as the cross-over from one regime to the other is still debated [20, 21].

Consequently, the goal of this thesis is to experimentally study dynamical vortex rearrangement for straight edge and indented samples, investigate the interplay between dynamically and thermally driven flux penetrations and study the magnetic and thermal conditions leading to the latter.

In order to do so, **Chapter 2** establishes the required concepts for uninitiated readers. Starting with the physical variable used to describe the superconducting state, we explain the mechanism responsible for the appearance of quantized flux in superconductors. Next, we distinguish between dynamically and thermally driven flux flow and in both cases, describe the driving forces for the rearrangement of the magnetic field. Dynamical flux penetration is described through critical state models while the existence of thermal flux penetration is treated in the thermomagnetic model. Finally, the characteristics of thin film geometries are described.

To compare experimental results with theoretical predictions, magnetic field imaging techniques are necessary. **Chapter 3** exposes the reader to magneto-optical imaging (MOI) based on the Faraday effect. After a brief introduction to polarized light microscopy, we describe the origin of the Faraday effect, at the center of MOI. Next, the noise sources of the set-up are described and a procedure for noise reduction in the experimental images is exposed. We then describe the problem of magnetic artefacts in MOI indicators and present a way to correct them. The set-up used for the measurements is described before providing an explanation of a calibration procedure allowing a quantitative mapping of the magnetic field in the sample. Finally, some chosen examples of MOI on various samples close this chapter.

In **Chapter 4**, micro-indented YBCO thin films are used for the study of dynamical magnetic flux penetration, occuring when ramping up the applied magnetic field changes the state of vortex pinning from metastable to instable. Previ-

ous experiments [20] showed a mismatch with the predicted theoretical penetration patterns [22]. The thin YBCO film studied combines several parameters ideal to study the discrepancy between experimental and theoretical flux penetration. By choosing a high-T_c (93 K) superconductor with small coherence length, we minimize the effect of surface barriers on vortex penetration. The large range of temperature available (up to 80 K) allows us to test the temperature invariance of the flux penetration profile. Finally, looking at indentations of various shapes, we analyse the spatial extension and asymmetry of the virgin sample profile and compare the experimental results with numerical predictions using finite element methods simulations of flux penetration.

Chapter 5 tackles the study of magnetic flux penetration in a thin Nb film. In this sample, dynamical reorganisation of vortices shares the stage with thermally driven processes. Magneto-optical imaging allows for a complete spatial mapping of magnetic penetration, in turn allowing us to study correlations of the two flux penetrations. Contrary to other techniques, MOI is insensitive to local temperature increase, the hallmark of thermally driven flux penetration. We recover the ability to discriminate between dynamically driven and thermally driven flux penetration using statistical analysis of the flux penetration patterns. The size distribution allows us to define an unambiguous discriminating criteria between both types of flux penetration. We first look at the statistical occurrence of magnetic flux penetration of both dynamical and thermal nature. From this, we show the power law associated with dynamical magnetic flux penetration. Thanks to the spatially resolved MOI, we then study nucleation spots of thermally driven flux penetration. We correlate it to the spread of the threshold field H_{th} and find an anti correlation with the preferential spots for dynamically driven magnetic flux penetration. Finally, we discuss the existence of two distinct thresholds for triggering of thermally driven magnetic flux penetration and their evolution with temperature.

Finally, in **Chapter 6** we summarize the main points of this thesis, their significance for the comprehension of vortex dynamics in superconductors, and discuss the experimental and theoretical perspectives that could result from this thesis.

Chapter 2

Magnetic landscape in superconductors

2.1 Introduction

The interesting physical properties of a superconducting sample, both from a technological and academic standpoint, occur when it is subjected to an external magnetic field. The goal of this chapter is therefore to describe how the magnetic field and superconductors are affected by one another. To do so, we start by describing the two types of superconductors and the behaviour of the magnetic field at the interface between the superconductor and another phase, be it another material, air, or the normal phase of the superconducting material. We discuss the nucleation of magnetic flux quanta in type-II superconductors and their redistribution as the external magnetic field is ramped up. This brings us to look at the forces responsible for vortex motion and vortex pinning as well as the dissipation associated to magnetic flux quanta displacement. We then analyse two extreme cases, one corresponding to isothermal flux quanta displacement and the other where the magnetic flux diffusivity largely exceeds the thermal diffusivity, leading to vortex displacement in a heated medium. In each category, we describe the physics at play and the models used to represent it. Finally, we examine thin film configurations and their unique characteristics as it is relevant to all samples studied in this thesis.

2.2 Characteristic parameters of the superconducting state

The superconducting state is limited to a region of physical parameters represented in Figure 2.1 (a). The first of these parameters is the critical temperature T_c. In conventional superconductos, at a temperature $T < T_c$, electrons of opposed spin and wave vector start to form Cooper pairs and condensate into a state of energy $\epsilon = \epsilon_F - \Delta$, where ϵ_F is the Fermi level of the material, Δ the en-

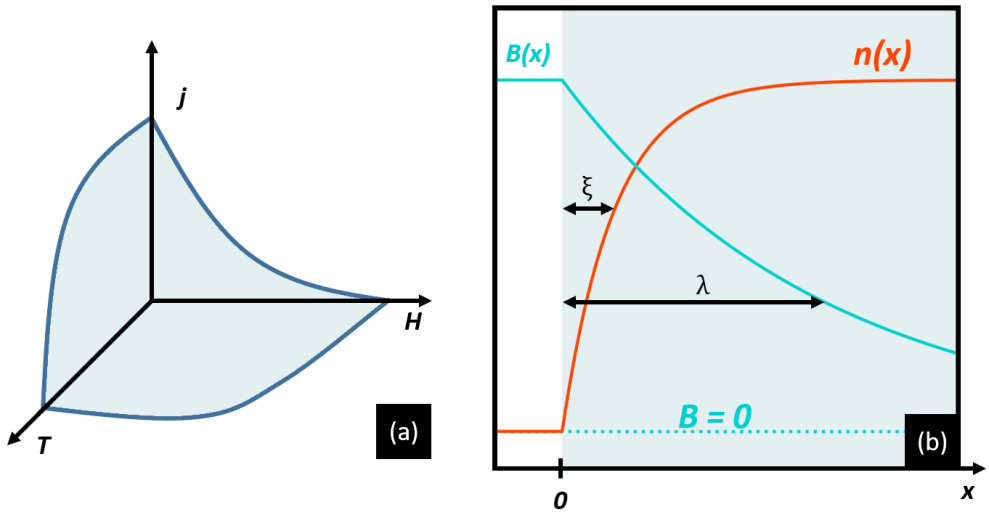

Figure 2.1: **(a)** Sketch representing the region of existence of a superconducting phase in the $H - T - j$ diagram. **(b)** Condensate near a normal (white) to superconducting (light blue) interface at $x = 0$. The blue line represents the spatial profile of the magnetic flux density B screened by the superconductor over a distance λ. In orange, recovery of the Cooper pairs density n over a distance $x \sim \xi$ from the interface.

ergy gap of the superconductor and ϵ its condensation energy. When approaching T_c, thermal perturbations of the order of $kT \sim \Delta$, where k is Boltzmann's constant, inhibit the pairing mechanism and superconductivity is destroyed. Another parameter limiting the superconducting phase is the magnetic field H. Because of the superconductor's perfect diamagnetism, there exists a field H_c, called the thermodynamical critical field, at which the energy gained by the system transitioning to the superconducting phase is counterbalanced by the magnetization energy required by the sample to maintain its inner region free of any magnetic flux. Finally, the lossless conduction of current is also limited to current densities below the critical current density j_c. While T_c and H_c are intrinsic factors of a superconductor, the maximal current density j_c is not. The intrinsic current density associated with a superconductor is the depairing current j_{dep}, over which it is energetically favourable for the electrons in a Cooper pair to split back into non correlated electrons. However, as will be explained in section (2.3), $j_c < j_{\text{dep}}$ and the exact form of $j_c(H)$ can be tuned with little effects on the other parameters. One can therefore realize the importance of optimizing $j_c(H)$ for applications and therefore the importance to study the magnetic response of superconductors.

To describe the behaviour of a superconductor in a magnetic field, two phenomenological parameters are used:

- λ, the London penetration depth, corresponding to the typical distance

needed for a superconducting sample to screen out an external magnetic field. It delimits the region where supercurrents circulate to create an opposite magnetic field. This parameter was introduced by H. and F. London in their equations [3]

$$\frac{\partial \boldsymbol{j}}{\partial t} = \frac{1}{\mu_0 \lambda^2} \boldsymbol{E}, \tag{2.1}$$

$$\mu_0 \nabla \times \boldsymbol{j} = -\frac{1}{\lambda^2} \boldsymbol{B}, \tag{2.2}$$

where $\boldsymbol{E}$ is the electric field, $\boldsymbol{B}$ is the magnetic flux density, $\boldsymbol{j}$ is the local supercurrent density, and $\mu_0 = 4\pi \times 10^{-7}$ H/m is the vacuum permeability. λ is related to the physical properties of the material via the relation $\lambda = \sqrt{\frac{m}{\mu_0 n_s e^2}}$ with m the mass of an electron, n_s the local density of superconducting electrons and e the elementary electrical charge.

- ξ, the coherence length of the superconductor, as described by Ginzburg and Landau [4]. This parameter gives an indication of the minimal distance over which a change in superconducting electron density can occur. In particular, when an interface between normal and superconducting material occurs, it takes a distance of $\sim \xi$ for the density of Cooper pairs to approach their asymptotic density far from the interface.

The screening of an external magnetic field and the recovery of the superconducting condensate is illustrated in Figure 2.1 (b). The ratio of these two parameters $\kappa_{\mathrm{GL}} = \lambda/\xi$, called the Ginzburg-Landau parameter, determines the behaviour of a superconductor under a magnetic field [23].

Samples with $\kappa_{\mathrm{GL}} < 1/\sqrt{2}$ are known as type-I superconductors. Because almost all elemental superconductors are of this type, they were the first to be discovered. A type-I sample cooled below T_c and subjected to a magnetic field $H < H_c$ will see its magnetization oppose the field so that in the volume of the sample $B = 0$, a phase called the Meissner phase. This behaviour will continue until the kinetic energy of the electron pairs forming the screening currents equals the condensation energy, at which point the sample will switch to its normal state.

Samples with $\kappa_{\mathrm{GL}} > 1/\sqrt{2}$ are known as type-II superconductors. Superconducting alloys, compounds, and dirty superconductors[1] are of type-II and they constitute the most relevant type for applications. In addition to their reaction under a magnetic field, this technological dominance can be related to alloys being easier to integrate in applications due to their strength and malleability. They possess two magnetic thresholds, $H_{c1} = \frac{\Phi_0}{4\pi\mu_0\lambda^2} \ln(\kappa_{\mathrm{GL}})$ and $H_{c2} = \frac{\Phi_0}{2\pi\mu_0\xi^2}$, where $\Phi_0 = \frac{h}{2e} = 2.07 \times 10^{-15}$ Wb is the quantum of magnetic flux, with h being Planck's constant. For $H < H_{c1}$, their behaviour correspond to type-I superconductors in

[1] Superconductors are referred to as dirty when the mean free path of normal electrons is smaller than the coherence length ξ if the material.

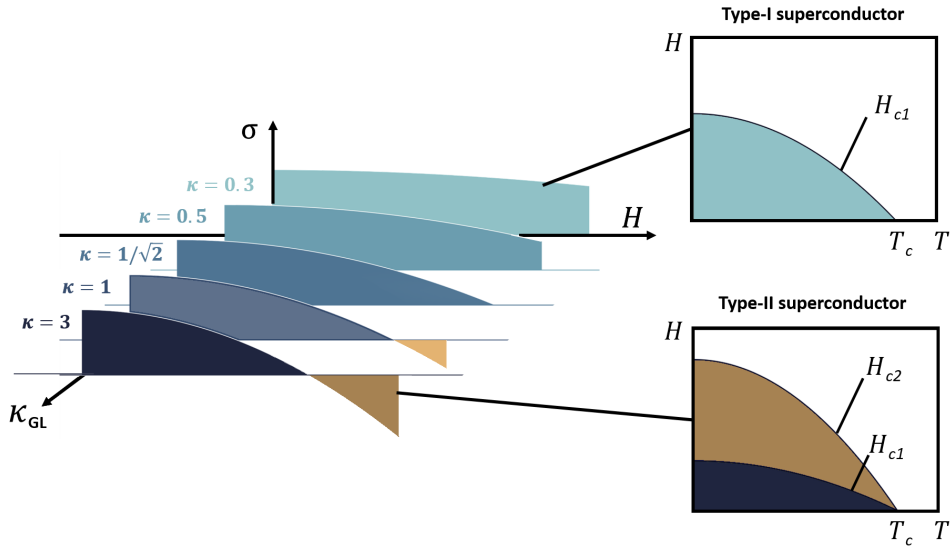

Figure 2.2: Energetic cost σ of a normal-to-superconducting interface as a function of the applied magnetic field H for different parameters κ. The value $\kappa = 1/\sqrt{2}$ corresponds to the transition between type-I and type-II superconductors whose phase diagram are shown in the upper right and lower right corners respectively.

Meissner phase, i.e. they expell the magnetic field such that $B = 0$ and the magnetization $M = -H$. For higher fields, this magnetization decrease in amplitude until reaching zero at the second critical field H_{c2}. This higher threshold before the complete loss of superconducting properties allows their use in applications until a much higher magnetic fields than type-I superconductors.

To understand why different values of κ_{GL} lead to different magnetic responses, we need to take a look at the role of λ and ξ in the energy cost associated with the creation of an interface between the superconducting phase and the normal metallic phase. The superconducting screening currents circulating in a region of thickness $\sim \lambda$ at the interface exponentially reduce the local magnetic flux density from its applied value B_{app} to $B(x) = B_{\mathrm{app}}\, e^{-x/\lambda}$, where x denotes the distance from the interface as depicted by the blue line of Figure 2.1 (b). At a distance from the interface $x < \lambda$, the magnetic field is only partially screened by the superconducting currents, reducing locally the energy spent by the system in opposing magnetization. In addition, the local density of Cooper pairs in the superconductor is also affected by this interface through the ξ factor. The Cooper pairs density as a function of the distance from the interface is given by $n(x) = n_\infty \left(1 - e^{-x/\xi}\right)$, where n_∞ is the density of Cooper pairs infinitely far from the interface, represented in orange in 2.1 (b). Contrary to the first term, this reduction in Cooper pairs density when approaching the interface means an increase in energy, as a lesser portion of the sample is in the lower energy superconducting state.

Within the Ginzburg-Landau formalism, a computation of the energy cost of an interface considering both effects gives $\kappa_{\mathrm{GL}} = 1/\sqrt{2}$ as the frontier for two types of behaviours for superconductors under an external magnetic field. Figure 2.2 shows the evolution of the surface energy associated to an normal-to-superconductor interface with increase applied magnetic field for different values of κ_{GL}. For type-I superconductors, the energy cost of a normal-to-superconductor interface is positive for every value of the applied field up to the critical field H_c. This results in the phase diagram, showed in the upper right region of Figure 2.2, with a single critical magnetic field H_c, boundary between the Meissner phase and the normal phase, respectively represented in blue and white.

In type-II superconductors, once the applied field exceeds the threshold field H_{c1}, the energy cost of a normal-to-superconducting interface becomes negative. As a result, the sample will have microscopic regions of normal material where magnetic field penetrates. Since the surface energy is negative, the system will tend to maximize the total area of the interfaces between the normal and superconductive states. It is favourable for the system to divide the magnetic flux in smaller and smaller bundles of flux lines. However, to preserve the coherence of the superconducting wavefunction, magnetic flux inside the superconductor must be a multiple of Φ_0. For $H > H_{c1}$, the system will therefore minimize its energy by creating bundles of magnetic flux lines Φ_0 inside the superconductor called vortices. The resulting phase diagram is showed in the lower right inset of Figure 2.2. The apparition of this phase coincides with the change of sign of the surface energy σ associated with a magnetic flux bundle.

Figure 2.3(a) shows the magnetic flux profile of such a vortex in a bulk isotropic superconductor, called an Abrikosov vortex. The central region of weakly varying magnetic field corresponds to the normal core of radius $\sim \xi$. Further from the center, the screening currents represented in dark blue produce a exponential decay of the magnetic field (in light blue). The radial profiles of magnetic flux, screening current density and Cooper pairs density are plotted in panels (b)-(d). While the precise profile of the vortex necesitate the numerical resolution of Ginzburg Landau equations, an analytical approximation can be found by modifying London's equation to take into account the non-constant $n(x)$. In this framework, the magnetic flux density represented by the light blue curve is given by [24]

$$B(x) = \frac{\Phi_0}{2\pi\mu_0\lambda^2} \frac{K_0\left(\frac{R}{\lambda}\right)}{K_1\left(\frac{\xi'}{\lambda}\right)}, \tag{2.3}$$

where K_0 is the zeroth order modified Bessel function of the second kind. The distance x from the center of the vortex is replaced by $R = \sqrt{x^2 + \xi'^2}$ where ξ' is an effective coherence length that minimize the Ginzburg Landau free energy. For $\kappa_{\mathrm{GL}} \to \infty$, $\xi' \to \sqrt{2}$ .Applying Maxwell equation $\mu_0 \boldsymbol{j} = \boldsymbol{\nabla} \times \boldsymbol{B}$ on eq. (2.3), we

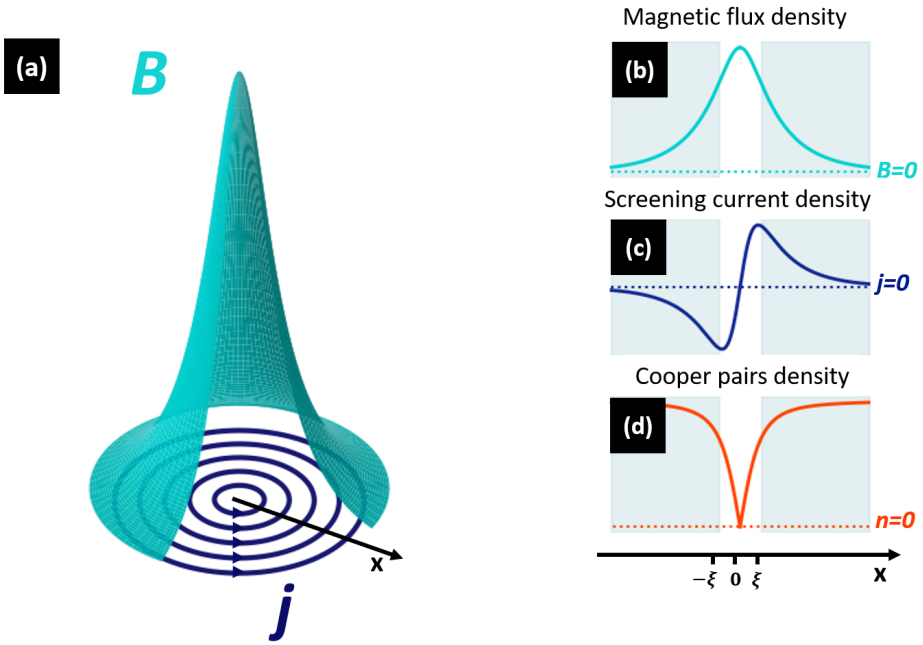

Figure 2.3: **(a)** Magnetic flux density profile and its associated screening currents in an Abrikosov vortex. **(b)-(d)** Radial profile of the magnetic flux density, corresponding screening current density and Cooper pairs density respectively. The normal core of radius ξ corresponds to the plateau in **(a)** and to the white region in **(b)-(d)**.

obtain the corresponding screening current density,

$$j(x) = \frac{\Phi_0}{2\pi\mu_0\lambda^3}\frac{x}{R}\frac{K_1\left(\frac{R}{\lambda}\right)}{K_1\left(\frac{\xi'}{\lambda}\right)} \tag{2.4}$$

where K_1 is the first order modified Bessel function of the second kind. The screening current density, plotted in dark blue in Figure 2.3(c), extends to $\sim \lambda$.

The entering of vortices in a type-II superconductor allows for some relief in the magnetic flux lines concentrated at the edges of the sample. Because of this, superconductivity can be maintained up to a much higher magnetic fields than in type-I superconductors but to the cost of the loss of perfect diamagnetism and zero resistivity encountered at lower fields [25]. By increasing the magnetic field, the density of vortices increases too. When H reaches H_{c2}, the vortex density reaches the point where the normal cores of the vortices start to overlap, *i.e.* their interdistance is of the order of ξ, and bulk superconductivity is completely suppressed. In the region between the two critical fields H_{c1} and H_{c2}, the behaviour of the superconductor is primarily influenced by the configuration and motion of

vortices inside the superconductor.

2.3 Vortex dynamics

When a vortex is set in motion, an electrical field is generated across its normal core. The unpaired electrons in the core start moving and dissipate energy via Joule heating. As a consequence, under a magnetic field, the critical current density j_c at which dissipation sets in is not the depairing current density j_{dep} but the current density necessary to induce vortex motion. The following section tackles the problem of vortex motion by describing the forces present in this problem.

2.3.1 Forces acting on vortices

To study the problem of vortex motion, let us first consider a defect-free sample under a magnetic field $H_{c1} < H < H_{c2}$ with a superconducting current density $\boldsymbol{j}$ passing through it resulting either from the screening currents or from a combination of screening current and transport current. Under theses circumstances, vortices in the sample are subjected to a Lorentz-like force whose density takes the form

$$\boldsymbol{f}_{\text{L}} = \boldsymbol{j} \times \boldsymbol{B}. \tag{2.5}$$

The total force exerted on the vortex $\boldsymbol{F}_{\text{L}}$ is obtained by integrating eq. 2.5 on the entire superconductor's volume. Because of the exponentially decreasing magnetic field of the vortex (cfr. eq. 2.3) the main contribution to this force will come from the region of radius λ around the center of the vortex. Because of the dissipation in the moving normal core, an opposite force taking the form of a viscous drag appears

$$\boldsymbol{F}_d = -\eta\, \boldsymbol{v}, \tag{2.6}$$

where η is the drag coefficient and $\boldsymbol{v}$ is the velocity of the vortex core.

This low disorder situation corresponds experimentally to a low ratio j_c/j_{dep} [26]. In these conditions, the sample is in a dissipative state called the flux flow regime. One can then define the resistivity of a sample in this flux flow state as

$$\rho_{ff} = \frac{n_v \Phi_0^2}{\eta}, \tag{2.7}$$

where n_v is the area density of vortices in the sample. In the simple model of Bardeen and Stephen [27], the flux flow resistivity can be linked to the normal state resistivity, ρ_n, via the expression [25]

$$\rho_{ff} = \rho_n \frac{\overline{H}}{H_{c2}}, \tag{2.8}$$

where $\overline{H}$ denotes the sample average magnetic field. Although the relation 2.8 guaranties a superconducting resistivity smaller than in the normal state, it is an important fraction of the normal state resistivity for a defect-free sample.

Real samples are often far from perfect crystallographic structures. They contain grain boundaries, second phases precipitates, dislocation, vacancies, etc., which all affect the superconducting condensate. Point defects tend to change the mean free path ℓ of the electrons which in turn reduces the value of ξ and increases the value of λ. On the other hand, when defects extend over a region of dimension $\sim \xi$, they create inhomogeneities affecting measurably the superconducting condensate and it becomes energetically favourable for vortices to have their normal core precisely at the weakened superconductivity region. The defect is called a pinning site as it prevents vortex motion via a pinning force density

$$\boldsymbol{F}_{\text{pin}} \approx -\boldsymbol{\nabla}\epsilon, \tag{2.9}$$

where ϵ is the local condensation energy of the superconductor. As ϵ depends on T, the importance of $\boldsymbol{F}_{\text{pin}}$ varies with temperature. When the temperature of the sample is lowered, the pinning force increase and may overcome the Lorentz-like force, thereby stopping vortex motion. For a certain temperature T and an applied field H, we can therefore define the critical current density $j_c(T, H)$ as the current density necessary to overcome the pinning forces of vortices in the sample, leading to dissipation through their core. When $\boldsymbol{F}_{\text{L}} \gg \boldsymbol{F}_{\text{pin}}$, the motion of vortices is predominantly set by currents. At the other extreme, for low current densities and low temperatures, vortex configuration is dictated by the pinning landscape. Due to thermal fluctuations and quantum tunnelling, vortices can still creep from one site to another [28]. The importance of thermal fluctuations can be assessed through Ginzburg number, G, while the importance of quantum fluctuations are contained in the quantum sheet resistance Q. Low-T_c superconductors are characterised by low G and Q numbers, of the order of 10^{-8} and 10^{-3} respectively, while both of these numbers are high, 10^{-2} and 10^{-1} respectively, for high-T_c superconductors [26].

Lastly, the vortices interact with each other and, similarly to how a transport current gives rise to a Lorentz-like force, screening currents from one vortex influence the others. When two vortices come within a distance $\sim \lambda$ of each other, the first vortex exerts a force on the second vortex whose density is given by

$$\boldsymbol{f}_{12} = \boldsymbol{j}_{v1} \times \boldsymbol{B}_{v2}, \tag{2.10}$$

where $\boldsymbol{j}_{v1}$ is the screening supercurrent density of the first vortex at the position of the core of the second vortex and $\boldsymbol{B}_{v2}$ is the magnetic flux density at the center of the second vortex. As a result, vortices of opposing chirality will attract each other, merge and annihilate. On the other hand, same chirality vortices will repel each other, giving rise, in the case of pin-free materials to a triangular lattice, so-called Abrikosov vortex lattice. When pinning sites are present, the lattice may be distorted, but the vortex interactions still play a major role as one vortex cannot move without changing the forces felt by the surrounding vortices. The total force necessary to induce the motion of a vortex is therefore often much greater than the pinning force exerted on a single vortex and one needs to compare the average pinning force of a group of vortices to the average driving force acting on it.

To predict the motion of a vortex, one could attempt to write Newton's equation of motion since flux quantization provides a certain rigidity (i.e. the vortex is topologically protected), taking m to be the inertial mass of the vortex. Theoretical and experimental evidences show this mass to be negligeable [29,30]. To obtain an equation of motion, we equal the drag force, only force containing a derivative of the position, to the sum of the other forces, $\sum_{i\neq d} \boldsymbol{F}_i = -\boldsymbol{F}_d \propto \boldsymbol{v}$. This equation is typical of overdamped medium and it follows that vortices set in motion will stop as soon as the total applied force $\sum_{i\neq d} \boldsymbol{F}_i$ vanishes.

Up to this point, the discussion about forces took place in the case of a vortex far from the border of the sample. To describe the problem of vortex nucleation at the edge of a sample, we must consider additional forces grouped under the denomination of surface barriers. These barriers are divided based on the scale of the phenomenon responsible for their existence.

Macroscopic surface barriers stem from the geometrical properties of the sample and are most present in films thicker than λ. Their result from the interaction of the entire sample with the surrounding magnetic field [31]. In the stage before the complete entering of the field in the sample in the form of a vortex, magnetic flux line are bent, rising the energetical cost associated with them. For films thinner than λ or samples with ellipsoidal shape, no bending of the magnetic field is observed and therefore these barriers do not come into play.

Microscopic surface barriers, referred to as Bean-Livingston barriers [32], stem from the interaction of a single vortex with the edge of the superconductor. They can be decomposed into two parts: a repulsive force stemming from the interaction of the vortex with the external magnetic field and an image force, attracting the vortex toward the edge. This image force is a result from the boundary condition $\boldsymbol{j}\cdot\boldsymbol{n} = 0$. The name image force comes from the fact that for an semi-infinite plane of superconducting material whose edge at $x = 0$, this boundary condition is mathematically equivalent to considering a vortex of opposite chirality symmetrically place with respect to the edge, outside the superconductor. The combination of both components of Bean-Livingston barriers allows for metastable configuration where even though it might be energetically favourable for the superconductor to have a vortex inside far from the edge, achieving this configuration necessitates to go through the intermediate state of higher energy with compressed screening currents.

The effect of both surface barriers is responsible for the existence of another critical field, the field of first vortex penetration H_p in the SC. While this value is hard to estimate for a given sample, it is bounded by H_{c1} at the lower end and by $H_{\mathrm{sh}} \approx H_c/\sqrt{2}$ at the upper end. In ultra pure samples, it is a contributing factor to their performance under high magnetic field [15].

2.3.2 Vortex dynamics regimes

The physical parameters quantifying the superconductivity of a sample (ξ, λ, j_c,...) all depend on temperature. Adding the fact that vortex motion generates local

heat and vortices interact with one another, it is not surprising that a plethora of vortex dynamics regimes can emerge. This thesis focus on dynamical and thermally driven magnetic flux penetrations in which the magnetic configuration of the studied samples are in a metastable state dependent of their magnetic history. Vortices are strongly pinned to defects and distributed inhomogeneously with a much higher density of vortex at the edges of the samples than in their center. One simple criterion to distinguish the two magnetic flux penetrations apart is to introduce a dimensionless parameter determined by the ratio between the thermal diffusivity D_t and the magnetic diffusivity D_m

$$\tau = \frac{D_t}{D_m} = \frac{\kappa/\rho c_p}{1/\mu_0\sigma_0}, \tag{2.11}$$

where κ is the thermal conductivity in W m^{-1} K^{-1}, c_p the specific heat capacity in J kg^{-1} K^{-1}, ρ the density in kg m^{-3} and σ_0 the normal state electrical conductivity in S m^{-1}.

The characteristics of dynamically driven ($\tau \gg 1$) and thermally driven ($\tau \ll 1$) flux penetrations are described in the next sections.

Dynamically driven flux penetration

When $D_t \gg D_m$, the heat produced by the vortex core is quickly assimilated by the surrounding. The motion of subsequent vortices can be considered as taking place in a quasi isothermal environment. The group behaviour of vortices is driven by the sole magnetic gradient of the out-of-equilibrium state. As such, one can estimate the speed of propagation of the flux front by looking at the flux flow regime [33]. Bhenia et al. [34] measured the temporal delay in flux increases between two points of a 20 μm wide Nb sample and found an experimental value of $\sim 5 \times 10^{-2}$ m s^{-1} for the propagation of dynamically driven flux penetration while theoretical predictions lead to $v \sim 0.25 - 80$ m s^{-1} [33]. Given the rather low speed of vortex displacement, it is reasonable to assume that dynamical flux penetration represents a simple reorganization of the flux front due to magnetic pressure with no need to invoke thermal effects.

One powerful tool to model the above described scenario is a set of models grouped under the name of critical state models. They all share the goal of describing the flux profile inside the superconductor based on a simple hypothesis [25]: the current density inside the superconductor is either equal to the critical current density j_c or equal to 0. The reasoning behind this assumption is that, being an overdamped system, vortex motion will stop as soon as the current density fall below the critical current density. This way, when an increase of magnetic field creates a spot where $j > j_c$, vortices are set in motion until the rearrangement of vortices lowers j below j_c where they stop abruptly. Conversely, in the vortex-free regions, $\boldsymbol{B} = 0$ and therefore[2] $\boldsymbol{j} = \frac{\nabla \times \boldsymbol{B}}{\mu_0} = 0$.

[2]This reasoning here is valid for bulk films in longitudinal configuration with no demagnetization effect. The thin film case is treated later in this chapter.

While after a reorganization of the flux front vortex motion stops, it is wrong to conclude that the sample is in equilibrium. Vortices are stuck to their pinning sites but given enough time the system will relax, due to thermal excitation or quantum fluctuations, to the real equilibrium state, much closer to a uniform vortex landscape. However, the total vortex relaxation having taken place in the sample as a function of time evolves as $\sim \ln(t)$. Far from the melting line of the vortex lattice, beyond which thermal fluctuations become important, the vortices are effectively anchored in place. Another underlying assumption of this model is that vortices are set in motion in groups because of the repulsive force they exert on one another. As a result, critical state models consider the mean pinning force in a given volume and disregard both the precise pinning landscape and the individual nature of the quantized flux lines.

The different models of critical states differ by the relation linking the critical current density to the magnetic field. The simplest and most common model was developed by C.P. Bean [35] and assumes a critical current density independent of the magnetic field and a first critical field $H_{c1} = 0$. To illustrate the magnetic profile expected from this model, Figure 2.4(a) represents a long superconducting sample of dimension $2w \times l \times L$, with $L \gg l$, w, in a magnetic field parallel to its longest axis (i.e. with a small demagnetization effect). The magnetic profile, given by Maxwell's equation $\partial B_z/\partial x = \mu_0 j_y(x)$ is illustrated for different values of the applied B_{app} in Figure 2.4(b). The field decreases linearly from $B = B_{\text{app}}$ at the interface to $B = 0$ at a distance $a = B_{\text{app}}/j_c$ from the interface, leaving a flux free central region of width $2(w - a)$. As the applied field is increased, the flux free region is reduced, vanishing for $B_{\text{app}} = B^* = wj_c$, with currents circulating in the entire sample, as shown in Figure 2.4(c). If the field is further increased by δB, the whole sample will see its magnetic flux density profile increase by the same amount δB at each point in the superconductor. For applied magnetic flux densities higher than B^*, the simple relation $j_c = \alpha(T)$, where α is only function of temperature, shows its limits. To better capture the real magnetic profile across the sample, we must change to a critical current density also dependent on the magnetic field, as proposed by Kim, Hempstead and Strnad [36]. The most versatile function $j_c(T, B)$ takes the form $j_c(B) = \alpha(T)/(1 + B/B_k)^\beta$, where B_k and $\beta > 1$ are fitting parameters. That being said, since most measurements realized in the framework of this thesis where carried out at $B < B^*$, Bean's model is still suited to describe the experimental results presented in the next chapters.

As we pointed out above, this class of models assumes a constant current density $j = j_c$. It therefore ignores the possible variations of the current density that can occur from the presence of a non superconducting macroscopic defect, resulting in current crowding [37]. A more realistic approach is to model the superconductor using Maxwell's laws and add a constitutive relation $\boldsymbol{E} = \rho(j)\boldsymbol{j}$, where $\rho(j)$ is a non linear function of j [38]. It is usual to take $\rho(j) = \rho_0(j/j_c)^{n-1}$, where $n \in [1; +\infty[$ is called the creep exponent. The case $n = 1$ corresponds to an ohmic behaviour while for $n \to \infty$ we recover Bean's model [39].

Let us conclude this section by noting that while Bean's model describes the

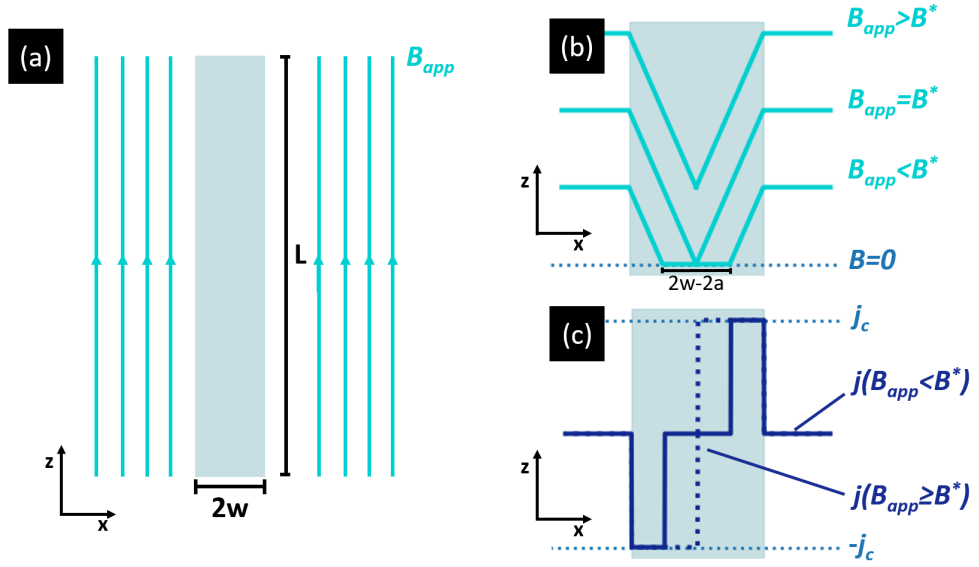

Figure 2.4: Bulk superconductor (in light blue) in longitudinal configuration in a magnetic field. **(a)** Sample in an applied magnetic flux density. **(b)** Magnetic field flux density B predicted by Bean's model for partial ($B_{\text{app}} < B^*$) and full magnetic flux penetration ($B_{\text{app}} \geq B^*$). **(c)** Corresponding screening current density.

metastable state of the system, it makes no prediction on how the vortices achieve this state. We stated that due to their repulsive interactions, vortices tend to move in bundles. The combination of vortex-vortex and vortex-pinning interactions makes reorganization of vortex landscape a possible candidate for observing self-organized criticality to occur [40]. The hallmark of self-organized criticality in a system is a scale invariant power law for the probability of an event. Experiments have shown that events of vortex bundle motion needed to adapt to Bean's magnetic profile are indeed distributed according to $\mathcal{P}(s) \sim s^{-\alpha}$, where $\mathcal{P}(s)$ is the probability of an event of size s to occur and $\alpha < 0$ is the critical exponent [33,40–43]. The question of the particular form of $\mathcal{P}(s)$ will be discussed in chapter 5.

Thermally driven flux penetration

When $D_t \ll D_m$, upon increasing the applied magnetic field H_{app}, the magnetic flux move much faster than the generated heat can propagate. As the condensation energy goes down when the temperature increases, the trail created by the displacement of the vortex acts as a attractor, like a pinning center would, for a vortex following in its wake. This following vortex then generates more heat in that region, thereby increasing further the attraction of vortices in their path. This

feedback loop leads to a trail of warmed material responsible for sudden burst of magnetic field inside the superconductor. These bursts are called thermally driven flux avalanches and are characterized by extreme propagation speed, exceeding the local speed of sound ($\approx$ 50 - 180 km/s [44–46]) and heat generation which can lead the local temperature to rise above T_c. In high-T_c superconductors, where critical current densities can exceed the electromigration[3] current density [49], this trail of non superconducting material could be responsible for the electromigration of the superconductor as the screening supercurrent is forced through normal material and in extreme cases, this phenomenon can lead to the melting of the material [50].

To date, the best suited model to study the appearance of these bursts is the thermomagnetic model [51–54]. It consists of adding to Maxwell's equations a heat transport equation. The total system to solve is therefore

$$\nabla \times \boldsymbol{H} = \boldsymbol{j}, \tag{2.12}$$

$$\nabla \cdot \boldsymbol{H} = 0, \tag{2.13}$$

$$\nabla \times \boldsymbol{E} = \frac{\partial \boldsymbol{H}}{\partial t}, \tag{2.14}$$

$$\nabla \cdot \boldsymbol{j} = 0, \tag{2.15}$$

$$c_{\mathrm{p}} \frac{dT}{dt} = \kappa \nabla^2 T - \frac{h_{\mathrm{t}}}{d}(T - T_0) + \frac{1}{d}\boldsymbol{j} \cdot \boldsymbol{E}, \tag{2.16}$$

where c_{p} is the specific heat of the superconductor, κ is its heat conductivity, h_{t} is the heat transfer through the substrate, T_0 is the substrate temperature, and d is the superconductor thickness. Moreover, the current density $\boldsymbol{j}$ is related to the electric field $\boldsymbol{E}$ through the current-voltage relation:

$$\boldsymbol{j} = j_c(T) g(E) \frac{\boldsymbol{E}}{E}, \tag{2.17}$$

where the exact form of $g(E)$ is unimportant but must respect the condition $\partial \ln E / \partial \ln j \gg 1$. The usual choice of $g(E) = \rho(j) = \rho_0 (j/j_c)^{n-1}$, presented previously, fits this constraint.

The study of this system and the stability of its solutions reveal the existence of a minimal field penetration length below which thermally driven flux penetration cannot occur [54, 55]. For a superconducting strip, this length is given by

$$l^* = \frac{\pi \sqrt{\kappa}}{2\left(\sqrt{|j_c'|E} - \sqrt{\frac{2h_t}{nd}}\right)}, \tag{2.18}$$

[3]For low dimension samples, the increased heat exchange between the environement and the sample delays the melting of the material due to Joule heating. It is then possible to reach current densities high enough so that the electron wind inside the material is strong enough to move atoms. Electromigration in Nb samples was explored in [47] while the YBCO case was treated in [48].

where $|j_c^{'}| = \frac{\partial j_c}{\partial T}$ and E is the magnitude of the electric field at the nucleation point of a thermally driven flux penetration at the begining of the perturbation. The term $\sqrt{|j_c^{'}|E}$ corresponds to the heat generation of vortices while $\sqrt{\frac{2h_t}{nd}}$ corresponds to the dissipation of heat through the substrate. To this l^* corresponds a lower magnetic field threshold

$$H_{th,1} = \frac{j_c d}{\pi} \operatorname{arcosh}\left(\frac{w}{w - l^*}\right), \tag{2.19}$$

delimiting the frontier below which no thermally driven flux penetration can occur. Note that the Equation 2.19 is taken from Bean's critical state model which suppose a lower critical field $H_{c1} = 0$, cuation must therefore be taken for the predictions at lower temperature and field. The region of instabilities is delimited in its upper part by a second threshold $H_{th,2}$. Its value corresponds to the magnetic field where the required instability length l^* becomes bigger than the half length of the film. Figure 2.5 show both of these thresholds obtained by using the following temperature dependency of each parameters: $\kappa = \kappa_0(T/T_c)^3$, $h_t = h_0(T/T_c)^3$, $j_c = j_0(1 - T/T_c)$ and $n = n_0(T_c/T - 1)$. The typical magnetic flux penetration for both sides of this boundary are represented in the right inset.

2.4 Thin film superconductors

Thin film technology is of particular interest for superconducting applications and justifies that all samples in this thesis are thinner than 150 nm. With reduced thickness and increased aspect ratio come a host of modifications in the physics of superconductors.

The most evident effect arises from the screening of magnetic flux density by the superconductor. The thin film samples placed in transverse configuration, with $\boldsymbol{B}$ perpendicular to the plane of sample, lead to an increased magnetic flux density around the edges, as illustrated in Figure 2.6(a). This geometrical effect on the magnetic flux lines is captured in the demagnetization factor N. Strictly speaking, this approach is valid for sample of ellipsoidal shape with linear magnetic response. The demagnetization effect of a straight edge thin film of thickness d and width $2w$ ($d \ll w$) can nevertheless be approximated by an ellipsoid with half major and minor axis $a = w, b = d/2$. The value the field at the edges can be written as

$$B_{\text{edge}} = \frac{B_{\text{app}}}{1 - N}, \tag{2.20}$$

with $N \approx 1 - d/w$ [38]. For typical values corresponding to the samples we will handle in this thesis, $d \approx 10^{-7}$ m and $w \approx 10^{-3}$ m , therefore $B_{\text{edge}} \gg B_{\text{app}}$. This magnification of the applied magnetic flux density at the edge is illustrated in Figure 2.6(b). A consequence of the sharp bending of magnetic flux lines is the generation of screening currents spanning the entire sample even in the region without magnetic flux density, as shown in Figure 2.6(c).

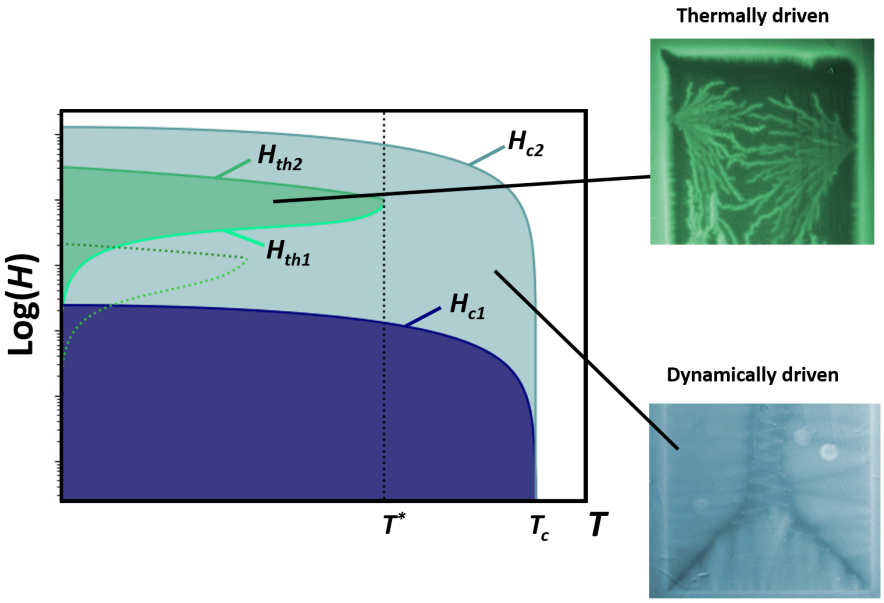

Figure 2.5: $\mathrm{Log}(H) - T$ diagram of a type-II superconductor. The white region above H_{c2} and T_c corresponds to the normal state of the sample. The darkest blue region at low magnetic field represents the Meissner phase. Above H_{c1}, the flux penetration in the light blue region is dictated by dynamical flux penetration. A typical example of magnetic flux penetration, as observed by magneto-optical imaging, is given in the lower right inset, with lighter regions associated with a high magnetic field and darker regions associated to low magnetic field. Crossing the $H_{\mathrm{th},1}$ curve, the green region corresponds to the vortex reorganization dominated by thermally driven flux penetration, shown in the upper right inset. With increasing magnetic field, the sample crosses the second threshold $H_{\mathrm{th},2}$, denoting the end of thermally driven instabilities. Both thresholds join at T^*, the maximum temperature at which one observe these abrupt magnetic flux penetrations. The dashed dark and light green lines correspond to the thresholds obtained for a reduction of the critical current density by an order of magnitude.

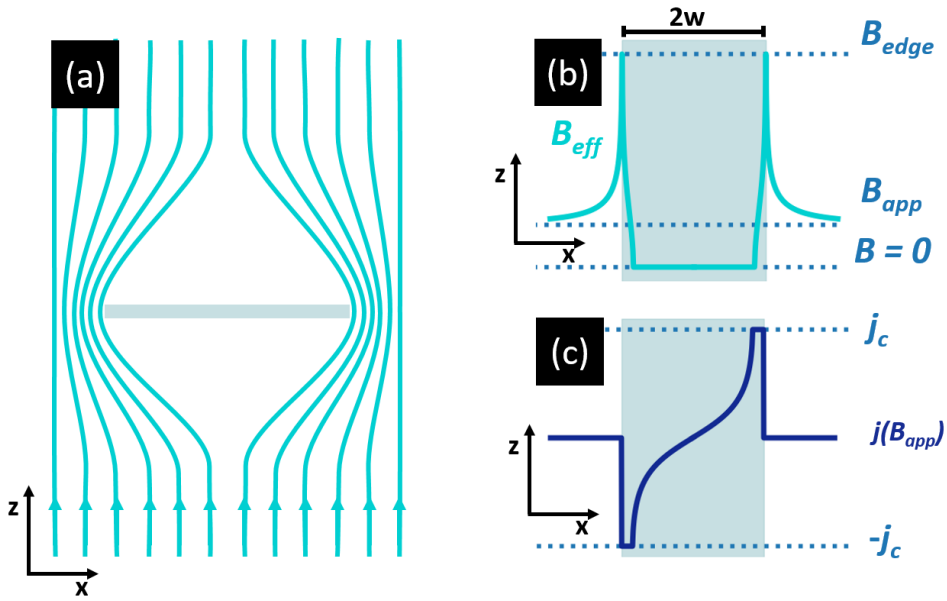

Figure 2.6: Demagnetization effect on a thin film superconductor (in light blue) with a magnetic field applied perpendicularly to the sample plane. **(a)** The blue lines represent the bending of the magnetic field lines due to the screening inside the sample. **(b)** Effective magnetic flux density inside and outside the sample due to the demagnetization effect. **(c)** Corresponding screening current density extending over the entire sample.

When the film thickness $d \approx \lambda$, the London penetration depth must be modified as the effective penetration depth $\Lambda = 2\lambda^2/d$. This film's thickness also coincides with the transition from Abrikosov vortices to Pearl vortices. Strictly speaking, Pearl vortices are solutions of 2D superconducting planes [56]. At a distance $r \gg \lambda$ from their core, they are characterized by a long range decay $\propto 1/r^2$ instead of the $\propto e^{-r}$ decay of Abrikosov vortices. While our films are not *per se* 2D superconducting plane, one can expect some modification of the screening currents with a behaviour half way between these two extremes. As films get thinner, the surface-to-volume ratio increases. This means that surface scattering of electrons is increased, resulting in a reduced mean free path ℓ. One must therefore change ξ to an effective $\xi' = \sqrt{\xi\ell}$. Finally, this also reduces the relative importance of the specific heat of the superconductor compared to the heat exchange with the substrate, lowering l^* and therefore the threshold $H_{\mathrm{th},1}$ for thermally driven penetration.

Chapter 3

Magneto-optical imaging

3.1 Introduction

This chapter discusses the processes of converting a magnetic landscape, be it in a superconductor or a magnetic material, into a 2 dimensional real-time light intensity mapping that can easily be picked up by a standard camera. While many techniques exist to image both in-plane and out-of-plane magnetic fields, magneto-optical imaging (MOI) is at the core of the measurements of this thesis and therefore is the focus of this chapter. The processes of imaging a magnetic landscape through MOI can be subdivided into two tasks: converting the magnetic field intensity into illumination intensity and analysing the illumination pattern. Both tasks have limiting factors that degrade the precision of the measurement. We discuss these limitations and the possible improvements to mitigate them. We finish by a summary of the expected imaging capabilities of magneto-optics and illustrative examples of the technique.

3.2 Magneto-optical imaging

MOI converts magnetic field information into light intensity that can easily be captured by a Charge-Coupled Device (CCD) sensor. This can be made possible via the action of a Faraday active indicator on polarized light in the presence of a magnetic field. This section starts by discussing the basis of light polarization. Next, the Faraday effect, which is at the heart of MOI, is explained. We look at the indicators used in this thesis and extract their sensitivity, saturation field and observational limits. We then turn our focus at the imaging of the resulting light pattern and the signal deterioration associated with it. Next, we show how a robust quantitative calibration can be achieved and deduce the magnetic field detection threshold of our MOI system. Finally, we conclude by showing the particularities of the MOI technique and its complementarity with other techniques.

3.2.1 Polarized light

In its classical electromagnetic description, monochromatic light consists of an electric field $\boldsymbol{E}$ oscillating in phase with a perpendicular magnetic field $\boldsymbol{B}$, both propagating along the direction $\hat{\boldsymbol{k}} = \boldsymbol{E} \times \boldsymbol{B}$, as shown in Figure 3.1 (a). While it is always possible to define the direction of the electric field for any given point in space at any given time, for most for the light sources, the direction of $\boldsymbol{E}$ at a particular point changes incoherently over time and the light is deemed unpolarized. When the evolution of the electric field direction over time is predictable, we speak of polarized light. Mathematically, for a beam of light propagating in the direction $\boldsymbol{k} = \boldsymbol{z}$ as in Figure 3.1 (a), we can describe the orientation of the electric field over time as

$$\boldsymbol{E}(z,t) = \begin{pmatrix} E_x \\ E_y \\ E_z \end{pmatrix} = \begin{pmatrix} E_{x_0}\cos(kz - \omega t) \\ E_{y_0}\cos(kz - \omega t + \delta) \\ 0 \end{pmatrix}, \tag{3.1}$$

where ω is the angular frequency of the electromagnetic wave. Light for which δ varies over time are said to be unpolarized. For a fixed value of δ, the polarization of the light is split into three cases:

- $\delta = 0$ corresponds to a linearly polarized light, represented in Figure 3.1 (b). The electric field oscillates in a plane at an angle α with respect to the XZ plane given by $\tan(\alpha) = E_{y_0}/E_{x_0}$.
- $\delta = \pm\pi/2$ corresponds to a circularly polarized light. The angle α between the electric field and the x axis rotates over time and is given by the relation $\tan(\alpha) = \tan(kz \pm \omega t)$. For $\delta = + \pi/2$, the electric field appears to rotate counter-clockwise for an observer that sees the light coming at them. This beam of light is said to be left-circularly polarized. For $\delta = - \pi/2$, the electric field rotates clockwise and the light is said to be right-circularly polarized. Both cases are represented in Figure 3.1 (c).
- $\delta \notin \{0, \pm\pi/2\}$ corresponds to an elliptically polarized light. In that case, in addition to the rotation of the electric field direction over time, the wave is characterized by a varying amplitude of the field, as represented in Figure 3.1 (d).

In the case of magneto-optical measurements, the imaging is done via a linearly polarized light obtained by inserting a linear polarizer in the trajectory of a unpolarized light beam. For a polarized light beam, its intensity after the polarizer can be calculated using Malus law

$$I_{\text{after}} = I_{\text{before}}\cos^2(\theta), \tag{3.2}$$

where I_{before} and I_{after} are the intensity of the light before and after the polarizer and θ is the angle between the polarization axis of the light and the polarization

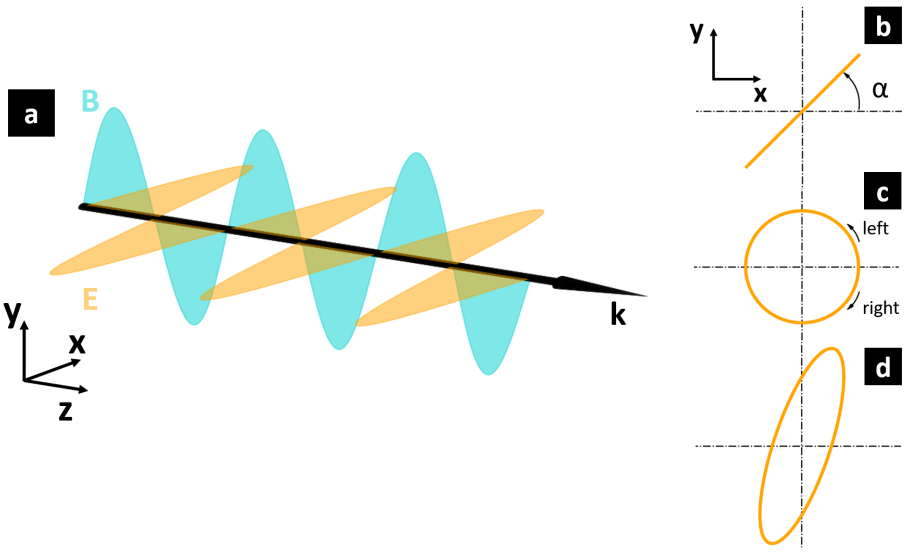

Figure 3.1: **(a)** Electromagnetic wave corresponding to a monochromatic polarized light. **(b-d)** Electric field for the three different types of polarized light as seen by an observer facing the electromagnetic wave. **(b)** Electric field for a linearly polarized electromagnetic wave at an angle α from the XZ plane, resulting from the superposition of left-circularly polarized light and right-circularly polarized light. **(c)** Electric field in left- and right-circularly polarized light. **(d)** Electric field in elliptically polarized light.

axis of the polarizer. Since unpolarised light can be viewed as a sum of linearly polarized light uniformly spread from $\theta = 0$ to $\theta = 2\pi$, the resulting intensity of the light after the polarizer is halved.

The modifications occurring on this polarized beam of light can be assessed by inserting an analyser further down the optical path. Although referred to by different names, analyzer and polarizer are both linear polarizers. By orienting them so that the relative angle between them is $\theta = \pi/2$, no light should be detected after the analyzer. A non-zero light intensity reflects a change of polarization of the incident light that, in our case, will be related to the local magnetic field.

Note that one important property of linearly polarized light is that it can be decomposed as an equal sum of left- and right-circularly polarized light of half the initial intensity. In the case of Faraday-effect-based magneto-optical imaging, it is this decomposition in opposite circularly polarized light that allows us to image the magnetic field as will be explained in the next section.

3.2.2 Faraday active medium

The Faraday effect allowing magnetic field visualization consists of the rotation of the polarization plane of a linearly polarized light beam when passing through an active medium in the presence of a magnetic field. This rotation is caused by a lack of mirror symmetry in the unit cell constituting the active medium. In turn, this lack of symmetry is responsible for different refraction indices, n_L and n_R, for left- and right-circularly polarized light.

The result on a linearly polarized light beam passing through an active medium is a mismatch between the speed of light for the right and the left component of the electromagnetic wave. This has the effect of changing the ratio E_{y_0}/E_{x_0} responsible for the angle of polarization of the light. The result is a rotation by an angle θ_A given by [57]

$$\theta_A = \frac{\pi d}{\lambda}\left(n_R - n_L\right), \tag{3.3}$$

where d is the material thickness and λ is the wavelength of the light.

Some materials are naturally devoid of mirror symmetry in their unit cell and are said to be circularly birefringent. In other materials, it is possible to break it via the application of a magnetic field. This forced symmetry breaking is at the origin of the Faraday effect. In that case, the rotation of the polarization plane is given by [58]

$$\theta_F = V(\omega)\int_{\text{o.p.}} \mu_0\, \boldsymbol{M}\cdot d\boldsymbol{l}, \tag{3.4}$$

where $V(\omega)$ is the frequency-dependent Verdet constant, $\boldsymbol{M}$ is the material magnetization and the integral is taken along the optical path in the medium. For a homogeneous material with constant magnetization and an optical path perpen-

dicular to the material's surface, Equation 3.4 takes the simplified form

$$\theta_F = V(\omega)\mu_0 M_z d, \tag{3.5}$$

where M_z is the magnetization component parallel to the optical path, along the $\boldsymbol{z}$ direction. Note that for a light beam passing through a Faraday active medium, being reflected and passing a second time in the opposite direction, as is the case in the experimental set-up of this thesis, the total rotation angle θ_F is not zero. This is due to the fact that the scalar product between the magnetization and the optical path changes sign for the return path, which compensates for the inversion of the integration bounds. The net effect is to double the rotation angle rather than to annihilate it.

Typical values of V in the visible spectrum are $\sim 10^{-5}$ deg mT^{-1} µm^{-1} [59]. As a result, to produce any noticeable change in the polarization of the light, one would either need extremely thick layers of material or high magnetic fields, both of which cannot be reconciled with the majority of experiments on thin film superconductors. For this reason, special materials with high Verdet constant need to be used.

3.2.3 Magneto-optical indicator

The ideal magneto-optical indicator for vortex observation must fulfil two antagonist properties. On the one hand, to obtain a good quality signal, the rotation angle must be big enough so that it can be clearly identified. On the other hand, the Faraday active layer must be as thin as possible to ensure proper spatial resolution. Indeed, as the final polarization rotation is the result of the average magnetization along the optical path, thicker indicators result in a blurring of the magnetic signal. In addition, while magnetic materials have high Verdet constant, we must limit ourselves to materials with low absorption coefficient as the light must travel trough the entire indicator and back before being picked up. The magnetic materials used as indicators must therefore be electrical insulators.

The material of choice for magneto-optical imaging of superconductors from the early 90's onward has been rare-earth substituted iron garnet with in-plane spontaneous polarization [60, 61]. The indicators used in this thesis are Bismuth doped Yttrium Iron Garnet (Bi:YIG - $Y_{3-x}Bi_xFe_5O_{12}$) of thickness $d = 3.5$ µm grown on a Gadolinium Gallium Garnet (GGG - $Gd_3Ga_5O_{12}$) substrate with (100) orientation. In addition to physical stiffness, this 450 µm-thick GGG substrate provides the ideal lattice parameter for epitaxial growth of the Bi:YIG. A 100 nm aluminium mirror is added to the opposite side of the GGG, ensuring a good reflectivity and images independent of the local topology of the superconducting sample. These indicators were characterized in detail in a previous work [62] and the reader is referred to it for further details. The Bi:YIG Verdet constant at $\lambda = 550$ nm, the wavelength used in our experimental set-up, is $V_{\text{Bi:YIG}} = 0.018 \pm 0.005$ deg mT^{-1} µm^{-1}.

Due to its magnetocrystalline anisotropy, the spontaneous magnetization of the indicator $\boldsymbol{M}_s$ rests in-plane. Upon the application of a magnetic field $\boldsymbol{H}_{\text{app}} = H_{\text{app}}\boldsymbol{z}$, the indicator changes the direction of its total magnetization $\boldsymbol{M}$, forming an angle ϕ with $\boldsymbol{M}_s$, as shown in the insets of Figure 3.2. From Equation 3.4, we deduce that for a light beam propagating perpendicular to the indicator, it is the change in the direction of this magnetization from fully in-plane to slightly out-of-plane that is responsible for the Faraday rotation of the polarized light.

To compute $\phi(B_z)$, we must write the angle dependency of the magnetic energy E_{mag} of the system and express the evolution of its minimum. In general, for a magnetic film in an external magnetic field, the leading terms of this energy take the form[1] [58]

$$E_{\text{mag}} = E_a \sin^2(\phi) - \boldsymbol{B}_{\text{app}} \cdot \boldsymbol{M}, \tag{3.6}$$

where E_a is called the anisotropy energy which can be assimilated to the energetic cost of moving the magnetization vector perpendicular to the preferred easy axis direction defined by $\boldsymbol{M}_s$. The second term is the Zeeman energy and corresponds to the magnetic energy cost of having a misalignment between the external applied field and the magnetization of the indicator. For an applied magnetic field in the z direction, perpendicular to the easy magnetization axis, the magnetic energy of the system is

$$E_{\text{mag}} = E_a \sin^2(\phi) - B_z M \sin(\phi), \tag{3.7}$$

which gives an equilibrium angle given by $\sin(\phi) = B_z M/2E_a$. The particular angle $\phi = \pi/2$ corresponds by definition to the anisotropy field $B_a = 2E_a/M$. Typical values of B_a for in-plane magnetized Bi:YIG are of the order of 100-300 mT [63, 64]. Note that this expression for B_a is only an approximation, as we limited ourselves to the first order development in the anisotropy energy in Equation 3.6.

It is possible to express the angle of rotation of the polarization plane of the light as a function of this anisotropy field and of the applied field as [64]

$$\theta_F = CM_z = CM_s \sin\left(\arctan\left(\frac{H_{\text{app}}}{\sqrt{2}H_a}\right)\right), \tag{3.8}$$

where C is a constant specific to each indicator and $H_a = \frac{B_a}{\mu_0}$.

In experiments, the situation is slightly different for two reasons. First, it is hard to ensure an applied magnetic field strictly in the $\boldsymbol{z}$ direction. If an in-plane field $\boldsymbol{H}_x$ is added, the Equation 3.8 must be modified to

$$\theta_F = CM_s \sin\left(\arctan\left(\frac{H_{\text{app}}}{\sqrt{2}H_a + H_x}\right)\right). \tag{3.9}$$

The consequence of this in-plane component is a reduced rotation angle for a given applied perpendicular magnetic field, as illustrated by the dashed line in Figure

[1] This form is similar to the Stoner-Wohlfarth model for single-domain magnetic particles.

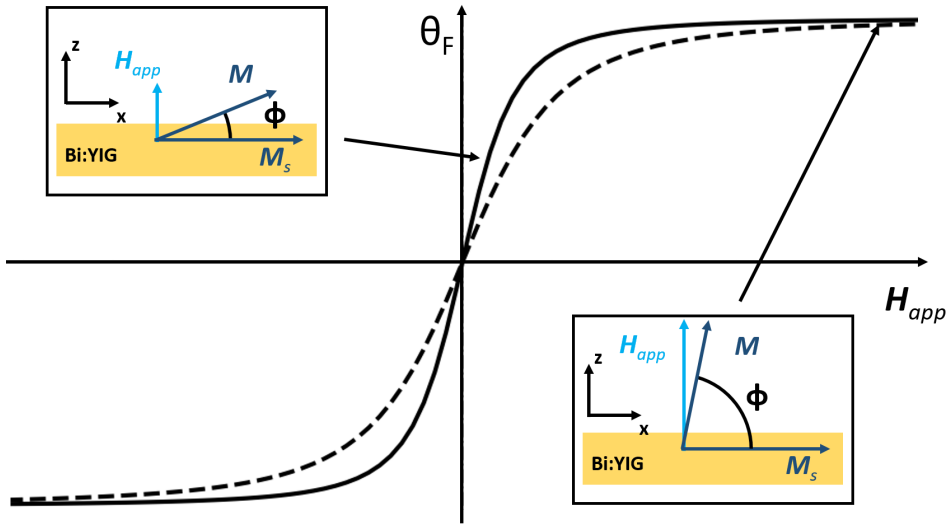

Figure 3.2: Faraday rotation as a function of the applied magnetic field. The continuous line corresponds to the rotation angle for an applied magnetic field strictly perpendicular to the film plane. The dashed line corresponds to the loss of sensitivity produced by an in-plane component of the magnetic field. The left inset shows that low applied magnetic fields are associated with small deviations ϕ from the spontaneous magnetization direction $\boldsymbol{M}_s$. In this situation, the indicator has a high sensitivity as a small variation in magnetic field corresponds to a substantial variation of the polarization direction θ_F. The situation for magnetic fields near the anisotropy field $\boldsymbol{H}_a$ is shown in the right inset. The magnetization direction of the indicator is then almost perpendicular to the plane and the sensitivity of the indicator is reduced since the indicator approaches magnetic saturation.

3.2. Second, it is even harder to ensure that the indicator lies in the XY plane due to an uneven mounting of the sample on the sample holder, an uneven contraction during cool down or any surface defect of the sample. While these two common imperfections of the experimental set-up result in a slight degradation of the signal from the MOI, the main resulting problem is the appearance of regions of different luminosities in the image. These artefacts and the algorithm developed to correct them are presented in the next section.

3.2.4 Magnetic artefacts in Bi:YIG

The unfortunate consequence of the inclination of the indicator with respect to the horizontal plane is the appearance of regions which react differently to an uniform applied magnetic field, thus creating undesired artefacts on the magneto-optical images as can be seen on the original image of Figure 3.4. This is due to the fact that multiple directions of in-plane magnetization are possible in the Bi:YIG

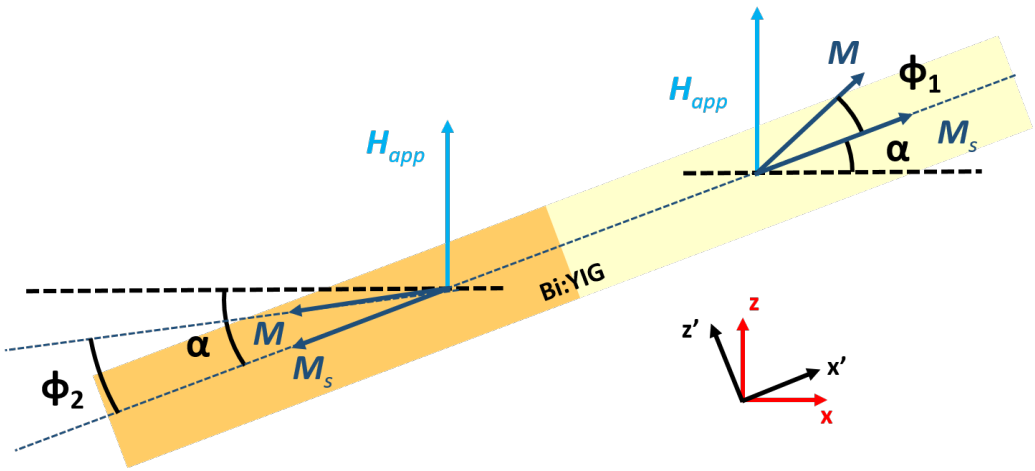

Figure 3.3: Magnetic domains of different in-plane orientations in a Bi:YIG indicator. Sketch of the combined effect of opposite spontaneous magnetization directions and inclination of the indicator with respect to the applied magnetic field direction.

indicator. For a perfectly horizontal sample and a perpendicular incident light, these domains are indistinguishable from one another as they react similarly to the applied field. This is no longer the case if the indicator is at an angle $\pi/2+\alpha$ with respect to the applied magnetic field, as the magnetization of each domain will be at a different angle from $\boldsymbol{H}_{\text{app}}$. To see this, consider two adjacent in-plane domains in the indicator having opposite spontaneous magnetization directions, as shown in Figure 3.3. Let us define two reference frames of axes $(\boldsymbol{x}, \boldsymbol{y}, \boldsymbol{z})$ and $(\boldsymbol{x'}, \boldsymbol{y'}, \boldsymbol{z'})$. The first reference frame is associated to the applied field and is such that $\boldsymbol{H}_{\text{app}} = H_{\text{app}}\boldsymbol{z}$. The second reference frame is associated to the indicator and is such that the in-plane magnetization lies perpendicular to $\boldsymbol{z'}$. For simplicity, we consider the spontaneous magnetization either parallel or anti-parallel to the $\boldsymbol{x'}$ but the following reasoning can easily be extended to any in-plane magnetization direction. In the second frame of reference, the applied field takes the form

$$\boldsymbol{H}_{\text{app}} = H_{\text{app}} \begin{pmatrix} \sin\alpha \\ 0 \\ \cos\alpha \end{pmatrix}. \tag{3.10}$$

From the sine's argument of Equation 3.9, we obtain the expected out-of-plane rotation of the magnetization angles

$$\phi_1 = \arctan\left(\frac{H_{app}\cos\alpha}{\sqrt{2}H_a + H_{app}\sin\alpha}\right) \tag{3.11}$$

and

$$\phi_2 = \arctan\left(\frac{H_{app}\cos\alpha}{\sqrt{2}H_a - H_{app}\sin\alpha}\right), \tag{3.12}$$

for $\boldsymbol{M}_s$ parallel and anti-parallel to $\boldsymbol{x}'$ respectively. This in turn will lead to a rotation of the polarization plane of the light of

$$\theta_{F1} \propto \sin(\alpha + \phi_1) \neq \theta_{F2} \propto \sin(\alpha - \phi_2). \tag{3.13}$$

This difference in polarization rotation leads to brighter and darker regions of characteristic triangular shape as illustrated in the original image of Figure 3.4.

Correction of magnetic artefacts in magneto-optical images

To prevent these magnetic artefacts, an usual trick is to force the direction of magnetization by applying a constant horizontal magnetic field, forcing the in-plane magnetization direction and favoring a single magnetic domain in the region of interest. To do so, our cryostat is equipped with a couple of coils able to generate a horizontal field of 2 mT in a fixed in-plane direction. This method however presents two disadvantages. First, as made evident by Equation 3.9 and Figure 3.2, this in-plane field decreases the sensitivity of the indicator to perpendicular magnetic fields. This is especially true in set-ups where the in-plane magnetic field is provided by strong permanent magnets. Second, any out-of-plane component of this permanent field will increase the perpendicular field by an unknown amount. This is particularly problematic for zero field cooling (ZFC) measurements where the sample is supposed to be cooled without an applied field below T_c before increasing the magnetic field to observe the sample behaviour under low magnetic fields.

Another approach to get rid of magnetic domains artefacts is to do numerical treatment once the image has been acquired. Since the spontaneous magnetization direction inside a magnetic domain is uniform, it is possible to correct magneto-optical images by scaling the detected light intensity up or down to match the illumination of a domain chosen as a reference.

The algorithm delimits portions of the image that the user will classify either as part of the dominant magnetic domain or as part of an artefact to be corrected. The different steps of this algorithm are illustrated in Figure 3.4.

We start by detecting the edges present in the image[2]. From the image I, two associated images I_x and I_y are created corresponding to the gradient in the image along the x and y direction. These images highlight the edges parallel to the y and x direction respectively, as illustrated in Figure 3.4 showing a MOI observation of a rectangular Nb thin film. I_x and I_y are created by the convolution of the image

[2]For noisy images, a preprocessing step consisting of convolving the image by a Gaussian kernel with a standard deviation $\sim$ 1-5 px to smooth out the picture might be necessary. This a due to the fact that differential operators in image processing exhibit high sensitivity to noise.

I with the kernels[3]

$$G_x = \begin{pmatrix} 0.125 & 0 & -0.125 \\ 0.250 & 0 & -0.250 \\ 0.125 & 0 & -0.125 \end{pmatrix} \tag{3.14}$$

and

$$G_y = \begin{pmatrix} 0.125 & 0.250 & 0.125 \\ 0 & 0 & 0 \\ -0.125 & -0.250 & -0.125 \end{pmatrix}. \tag{3.15}$$

We obtain the edges in any direction by taking the norm of the sum of the two images

$$I_{\text{Sobel}} = \sqrt{I_x^2 + I_y^2}, \tag{3.16}$$

where the operations are applied element-wise. This combination of I_x and I_y is refereed to as the application of the Sobel operator on the original image.

Due to noise in the image, the borders corresponding to the edges of the magnetic domains are often not continuous. This problem is solved by convolving the image with the stretch operator

$$S = \begin{pmatrix} 1 & 1 & 1 \\ 1 & 1 & 1 \\ 1 & 1 & 1 \end{pmatrix}, \tag{3.17}$$

which stretches each pixel of the I_{Sobel} image in both the x and y directions by 1 pixel. Next, to limit the number of edges associated with noise in the image, we apply a binary conversion filter whereby any pixel intensity below a manually defined threshold is set to zero and associated with a homogeneous region of space. Any pixel above this threshold is set to one and corresponds to a frontier between two homogeneous regions of space. Due to noise in the image, the number of domains delimited by the borders are usually unexpectedly high with regards to the actual number of artefacts in the image. Removing domains containing less than a set number of pixels discards these parasitic detections. In the example of Figure 3.4, a threshold set for a minimal area of 10 px reduces the number of domains from 125 to 68. While this number might look big for the given picture, this stems from the fact that each triangular spike on the edge of the Nb sample is detected as a single domain rather than as being part of a single domain with fixed magnetic in-plane orientation.

The user is then asked to provide two reference points for each domain to correct, one point inside the domain and the other outside, on a region of same magnetic landscape. The difference between these two values gives the correction to be applied to the domain. This is done via a flood fill algorithm[4] applied to the

[3] A brief illustration of this convolution process is shown in Appendix A as well as an explanation for the form of the kernels.

[4] The flood fill algorithm is the typical algorithm used for "bucket fill" options in digital image editor programs. While the method to determine pixels belonging to the same domain is the same, here the pixel value is shifted by a fixed amount while the bucket fill replace the value of each pixel by a pre-set value.

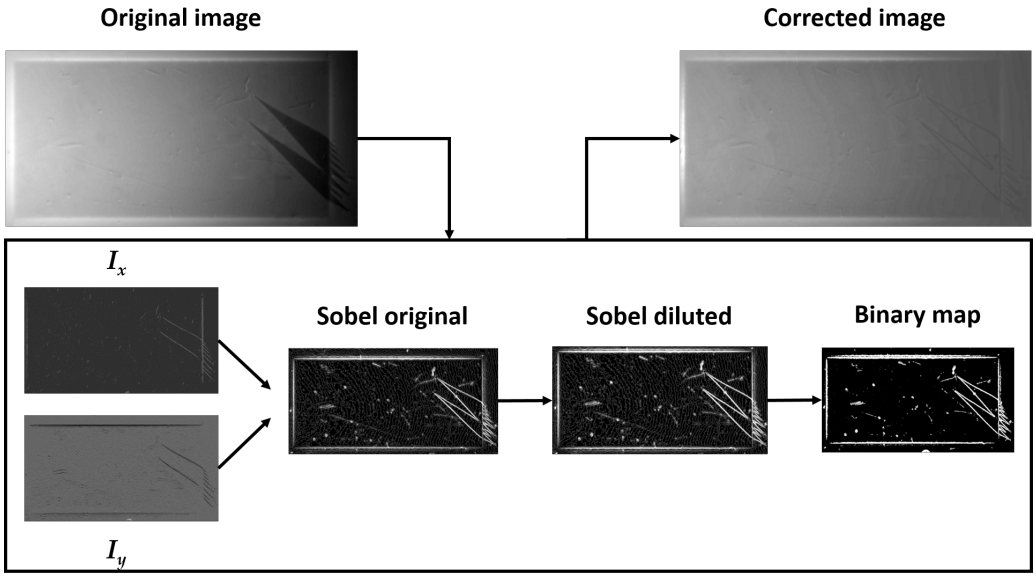

Figure 3.4: Illustration of the magnetic domains correction algorithm on a rectangular Nb thin film observed through MOI. Starting with the original picture of the top left, the algorithm creates the convolved images I_x and I_y then combine then to form the Sobel filtered image enhancing the edges. To ensure continuity of the edges delimiting the magnetic domains, a dilution filter is applied. Next, the image is converted to a binary map using a user-defined intensity threshold and a discarding of territories smaller than 10 pixels. The user manually select the regions to correct by shifting the intensity value of the whole domain. The final result, smoothed with a median filter on the edges is shown in the top right corner.

inside of the region where the difference in grey scale value is subtracted from the pixels initial grey scale values.

The procedure leaves a trail of uncorrected pixels corresponding to the borders of the domains. This trail can be smoothed out by changing its pixels' values to the mean luminosity of the closest pixels in a square of 5×5 px^2. The resulting corrected image can then be adjusted in contrast to enhance details otherwise invisible due to inter-domain contrast differences.

While this procedure leaves the magnetic landscape of the sample relatively unchanged, the numerical changes in luminosity render the light-to-magnetic field calibration described in section 3.2.6 impossible. In addition, since each domain correction requires manual inputs, this procedure is time consuming and should be reserved to a few selected images rather than be used in a systematic way.

3.2.5 Optical set-up

Once the out-of-plane magnetic information has been converted into a rotation of the polarization plane of the light, an analyzer translates it into light intensity information. The signal is then recorded throught a RETIGA-4000R 12-bit CCD camera. This section goes over the technical details of the imaging and capturing of magneto-optical images.

A schematic of the optical set-up is shown in Figure 3.5. The core of the system consists of an Olympus BX-RLA2 commercial microscope into which the different parts are mounted. The illumination is provided by a short arc mercury bulb (USH-103D) as a polychromatic light source which is rendered monochromatic by a 550-nm green filter (Olympus U-25IF550). The monochromatic constraint limits the aberrations in the system due both to the optical components and the wavelength dependency of the Verdet constant. The wavelength is chosen to be in the region where Verdet constant is the highest for Bi:YIG indicators around $\lambda \sim 500$ nm [65] and near the emission peak of the Hg bulb at $\lambda = 546$ nm, ensuring a bright monochromatic light.

Next, the monochromatic light passes through a fixed linear polarizer (UP-O3) and reaches a beam splitter which redirects it in the direction of the magneto-optical indicator mounted on top of the sample to be observed. Before reaching the indicator, the light passes through a $\times 5$ objective (LMPLFLN 5 BD)[5]. It then passes through the Bi:YIG magneto-optically active layer and the optically transparent GGG substrate. The light is reflected by the Al mirror separated by the sample by an air gap created by the sample's surface roughness, due to

[5] $\times 20$ and $\times 50$ objectives are also available. However no increased resolution has been noticed mainly due to a deterioration of the polarization by the longer path through the cryostat window associated with the bigger numerical apertures of the $\times 20$ and $\times 50$ objectives. To remedy this problem, some systems include the objective lens inside the cryostat, ensuring that the observed rays are perpendicular to the cryostat window when crossing it [66]. In our system, using those objectives only decreases the field of view, providing little additional details. In addition, the increase in numerical aperture allows for light rays to arrive at an angle with respect to the indicator, increasing the problem of magnetic artefacts.

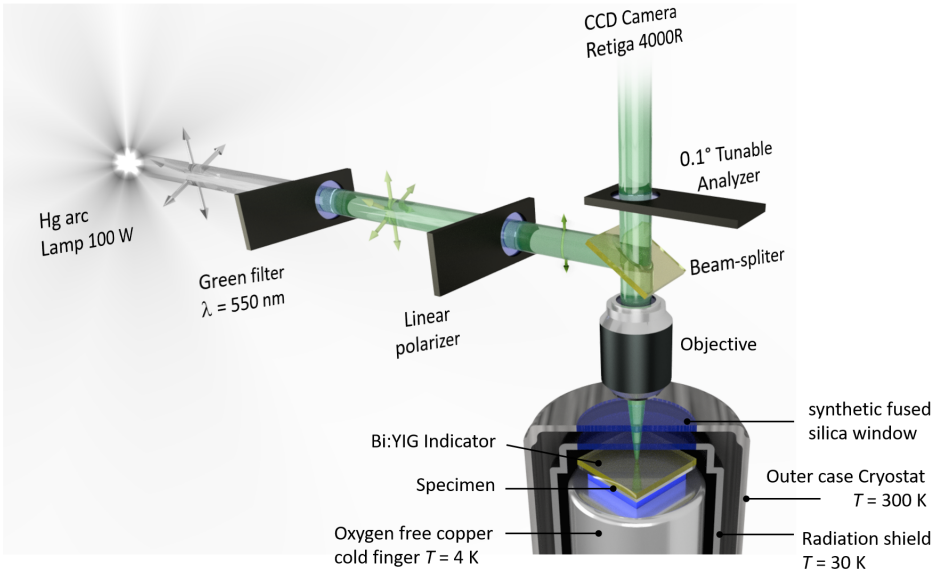

Figure 3.5: Schematic of a typical magneto-optical set-up. A Hg lamp produces a polychromatic light that is filtered down to a $\lambda = 550$ nm monochromatic green light. The light passes through a linear polarizer, is reflected by the indicator's mirror placed on top of the sample and sent through an analyzer before reaching the CCD camera. The small angle of the incident light with respect to the indicator's surface, limited by the numerical aperture of the microscope's objective is the main source of apparition of magnetic artefacts. Reproduced with the courtesy of Pinheiro, L. B. G.

scratches and dust particles. Light rays at a small enough angle for the objective numerical aperture then cross the beam splitter again to reach a rotatable analyser (U-AN360-3) whose angle with respect to the polarizer can be tuned from 0 to 180 degrees with a precision of 0.1 degree. The resulting signal is finally captured by the CCD sensor of the RETIGA-4000R camera. The 2048 $\times$ 2048 CCD sensor covers a field of view of $\sim 3 \times 3$ mm^2 where each pixel on the final image corresponds to a 1.48 $\times$ 1.48 µm^2 region.

The imaging possibilities of the system are determined by the signal-to-noise ratio for a given configuration. To obtain a decent quality image of superconductors, our system requires an exposure time of ∼0.5 s for an analyzer angle at ∼3 degrees from the cross-configuration[6], where the sensitivity is at its highest. The practical temporal resolution of MOI is dictated by the light intensity of the source, the sensitivity of the indicator and the observed magnetic field. The maximum observable magnetic field and sensitivity are intrinsic properties of the indicator used and cannot be easily changed. Changing the light source however is an easy way to increase the signal collected by the CCD. Using laser sources, several groups have managed to record reorganization of the magnetic field at microsecond [67], nanosecond [68] and even picosecond scale [46,69], approaching the intrinsic temporal resolution of Bi:YIG indicators of $\sim$ 1 ps [70].

In addition to increasing the signal, one can minimize the noise present in the image. In astronomy, a standard procedure to correct for the sensor's electronic noise is to transform the raw image I into a reduced image I' via the formula [71,72]:

$$I' = \frac{I - B - D}{F}, \tag{3.18}$$

where B is the bias frame, corresponding to an image taken with a zero second integration time, D is the dark frame, corresponding to a image taken with no light reaching the CCD but with the same integration time as the image, and F is the flat field, corresponding to an image taken with an uniform luminosity. The process is illustrated in Figure 3.6. The bias frame corresponds to the electrical background noise of the CCD sensor and is independent of the exposition time. The dark frame corresponds to the thermal noise in the sensor and increases linearly with exposition time. Finally, the flat field highlights the differences in pixel sensitivity in the CCD.

The flat field image differs in a microscopy setting as it is often hard to ensure uniform illumination. In that case, a flat field constituted of an unfocused image of an uniformly reflective substrate serves both to correct the uneven illumination, the defects in the analyzer, and the differences in pixel sensitivities. While this correction increases the quality of the magneto-optical images, it does not take into account all the of parameters influencing the image. First, the spatial variation of sensitivity in the indicator is neglected as the correction only adjust

[6] The cross-configuration, also referred to as the crossed Nicols, consists of the analyzer and polarizer being at a 90-degree angle from one another.

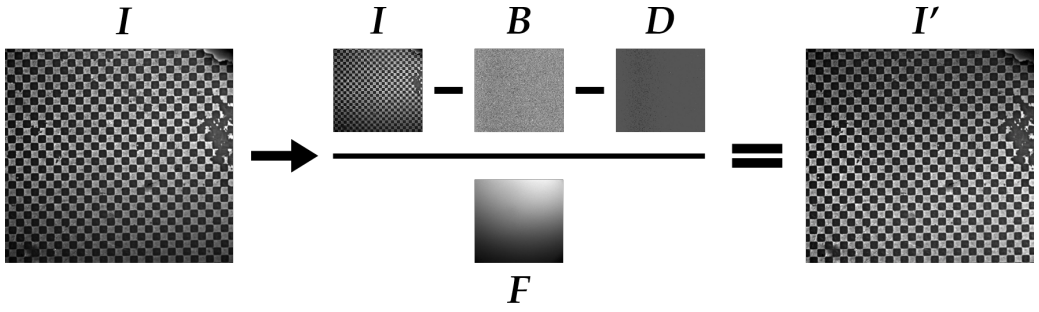

Figure 3.6: Image processing to eliminate the sources of noise of the CCD sensor on a magneto-optical image of a magnetic chessboard with alternating up and down magnetization. From the original image I are subtracted the bias frame B and dark field frame D before dividing the result by the flat field frame F.

the illumination and electronic noise. The next chapter describes a calibration procedure allowing us to compensate for this non-uniform sensitivity as well as from the temporal fluctuations of the light source intensity. Second, only the bias and dark noises were corrected in this procedure. This leaves the fluctuating shot noise obeying a Poisson distribution. As such, for a static magnetic landscape, this noise is reduced by a factor $\sqrt{N}$ by averaging N images.

3.2.6 Calibration procedure

Up to this point, discussions about features of a magneto-optical image in this chapter were qualitative. A number of schemes have been developed in order to turn MOI into a quantitative technique and transform the differences in luminosity into differences in magnetic flux density. [66, 73–80].

The method presented here is based on Reference [78]. It presents the advantage to compute a calibration procedure for every pixel of the image, thus taking care of the possible non-uniform sensitivity of the indicator and allowing to recover the magnetic response of samples with strong magnetic background signals such as in ferromagnet-superconductors structures. The idea behind the algorithm is to consider a simplified version of Malus law for the expected light intensity resulting from its second order Taylor expansion. This truncated expression of the light intensity I as a function of the applied perpendicular magnetic flux density B_z takes the form

$$I(B_z, x, y) = I_{\min}(x, y) + A(x, y)\left[B_z(x, y) - B_{\min}(x, y)\right]^2, \qquad (3.19)$$

where $I_{\min}$ is the estimated minimum light intensity recorded by the sensor, $B_{\min}$ is the value of the magnetic flux density needed to reach $I_{\min}$ and A is related to the local sensitivity of the indicator, all parameters being evaluated at the pixel's position (x, y). To estimate these parameters, a sweep in magnetic field must be

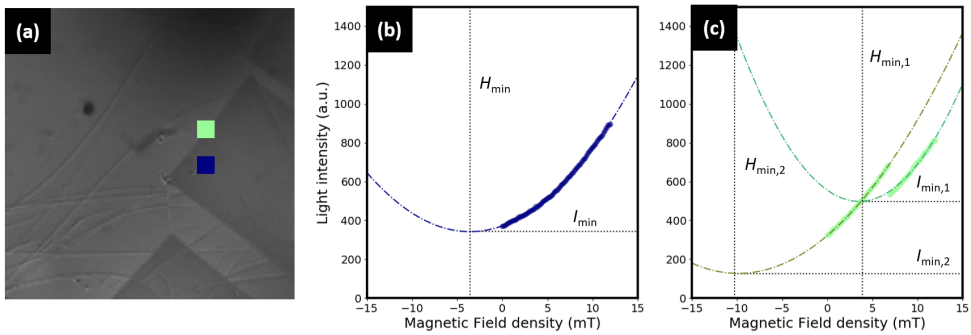

Figure 3.7: Calibration curves for a typical Bi:YIG indicator. **(a)** Indicator with visible magnetic domains during a calibration sweep. The coloured squares are centered on the pixels whose light intensity are plotted in (b) and (c). **(b)** Calibration curve of a pixel in a darker region of the indicator. The dots represent the experimental data while the curves are fitted from Eq 3.19. **(c)** Calibration curve of a pixel switching its magnetic domain during the magnetic sweep.

realized for each sample, indicator, and analyzer position. For superconducting samples, this sweep is done above T_c as to avoid any disturbance from the superconducting screening of the magnetic field. Bi:YIG's Verdet constant being almost independent of temperature far from its Curie temperature of ~ 545 K [81], the calibration parameters stay valid even for magnetic field conversions below T_c. A typical calibration curve is shown in blue in Figure 3.7 (b) for the pixel at the center of the blue square in Figure 3.7 (a).

Except for defects such as scratches on the indicator or dead pixels, neighbouring pixels tend to have similar values for $I_{\min}(x, y)$, $A(x, y)$, and $B_z(x, y)$. This, however, can change if an underlying out-of-plane magnetic landscape is present in the sample. The change in parameters is primarily noticeable in $H_{\min}$ as the applied field must counteract the local field to reach the minimum intensity value. Another reason for the spatial inhomogeneity in the calibration parameters is the existence of the magnetic artefacts discussed before. The green parabola of Figure 3.7 (c) corresponds to the calibration curve of the pixel at the center of the green square of Figure 3.7 (a). This image, taken in the middle of the calibration sweep, illustrates the jump from one domain to the other as the indicator magnetization suddenly changes its response to an increase of the magnetic field.

Using this conversion technique on permanent magnets as well as electromagnets, our system resolution was estimated to be 0.1 mT for punctual sources while extended sources (~ 20 µm) were detectable down to 0.01 mT. The smallest magnetic features resolved by our set-up was estimated at ~ 5 µm. The biggest obstacle to a higher resolution is the gap between the indicator and the magnetic sample, estimated at ~ 5 µm. For that reason, it is possible to increase the resolution of the MOI technique by pressing the indicator thanks to a spring loaded clip.

This pressing of the indicator has the detrimental effects of reducing the indicator lifetime and increasing the number of magnetic artefacts due to the mechanical stress induced to the indicator as well as scratching either the sample of the soft Al mirror of the indicator.

3.2.7 Selected examples of MOI

As we have seen in this chapter, MOI possesses attractive features for the study of superconductors. On the one hand, it allows for imaging of fast magnetic reorganization ($\sim$ ps). On the other hand, the technique combines a wide field of view ($\sim$ mm^2) with a high spatial resolution ($\sim$ µm). This spatial resolution makes it the ideal technique to study features of superconducting samples not observable via bulk measurements such as electrical transport, pick-up coil or magnetic susceptibility measurements that average the superconducting properties of the entire sample.

To illustrate this point, Figure 3.8 (a) shows a welded YBCO sample observed through a polarization microscope with clearly visible grains and Figure 3.8 (b) shows the associated magneto-optical image. A clear correlation can be drawn between the preferential regions for magnetic flux penetration appearing brighter on the magneto-optical image and the boundaries between grains visible under polarized light microscopy. This can be attributed to the local disorder associated with grain boundaries; locally weakening the superconducting condensate and acting as privileged channel for magnetic field penetration.

In other cases, the magneto-optical image provides information hidden to conventional optical imaging. Figure 3.8 (c) shows the optical image of a microstructured YBCO thin film of uniform appearance. Upon the application of a magnetic field, the magneto-optical investigation of Figure 3.8 (d) reveals a whole portion of the sample to be non superconducting despite no apparent difference in the optical image.

Let us show as a final example, a layered magnetic landscape observed by MOI. While the change in magnetization direction induced by the magnetic flux trapped in the superconducting layer is temporary for the magneto-optical indicator, for other magnetic layers, one can hope for a permanent change of magnetization [82]. Figure 3.9 shows such a realization, composed of a Nb thin film deposited on top of a hard disk drive (HDD) using perpendicular magnetic recording technology and observed via MOI. The sample is cooled below $T_c = 9$ K in a zero field cooling (ZFC) procedure. The applied field density is then increased up to $B = 4.8$ mT. The MOI of the sample confirms the presence of characteristic marks of magnetic flux penetrations (Figure 3.9 (c)). Upon turning off the applied field and warming of the sample at $T > T_c$, the remanent imprinting of the magnetic flux penetration on the HDD remains visible by MOI despite the disappearance of the trapped vortices. After cleaning of the HDD state by the application of a strong uniform magnetic field above T_c, the sample is cooled under an applied field of $B = 4.8$ mT, a procedure called field cooling (FC). Upon switching off the magnetic field,

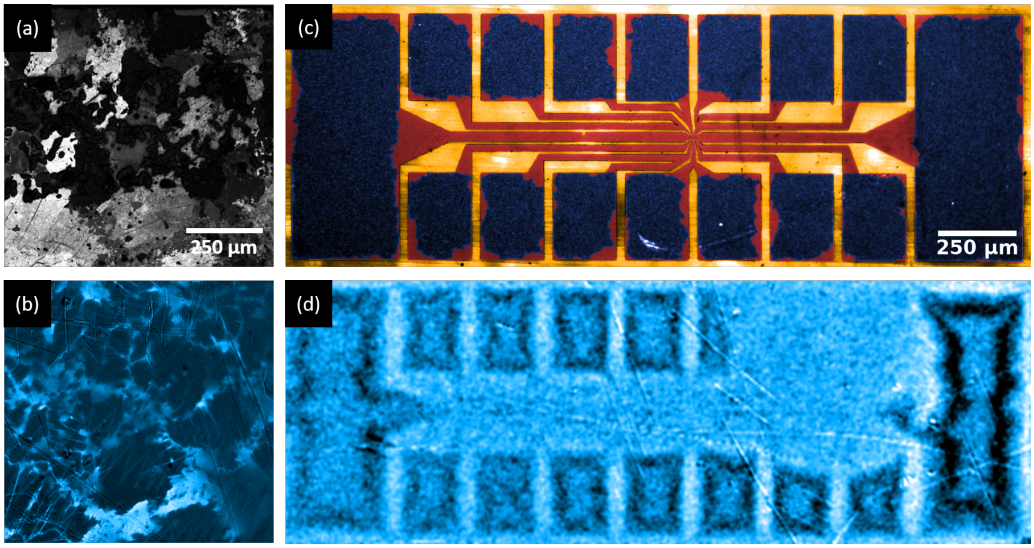

Figure 3.8: **(a)** Optical image of a welded YBCO sample under a polarization microscope. The regions of different brightnesses correspond to grains of different orientations. **(b)** MOI of the sample (a) taken below its critical temperature under magnetic field. The lighter part of the image corresponds to a higher local magnetic field and follow preferentially the grain boundaries observed in (a), indicating a decrease in local screening currents associated with the local crystalline disorder. **(c)** Optical image of a YBCO transport bridge (in red) on a $LaAlO_3$ substrate (in yellow). The blue regions on the red rectangular pads are composed of an added Ag layer to facilitate contacts made by wirebonding. The optical information shows textural uniformity amongst the connecting pads of the sample, leading to believe in an homogeneous sample. **(d)** Differential MOI of the sample (c) showing a region of depleted superconductivity in the upper right corner invisible through optical means. The signal represented here is the difference between the remanent magnetic field after exposing the sample to 5 mT and the signal obtained above T_c. Note that as mentioned earlier the distance from the YBCO film to the indicator is the main reason for the lack of resolution when compared to an optical image. This makes it impossible to see the leads to the central device and only the signal from the bonding pads are visible.

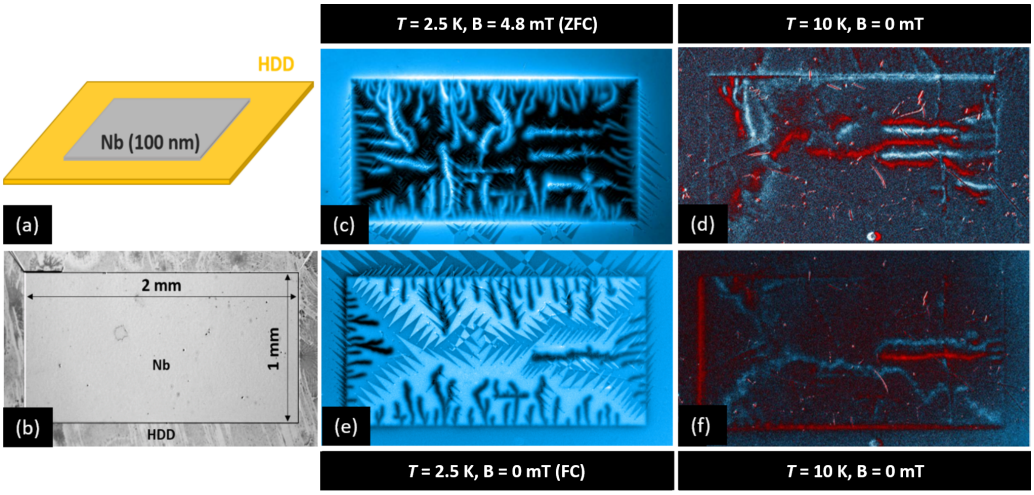

Figure 3.9: **(a)** Layout of the Nb-HDD sample, constituting of a Seagate Barracuda ST500LM030 hard drive, relying on the perpendicular magnetic recording technology, and a 100 nm-thick Nb superconducting film. **(b)** Optical image of the sample layout. **(c)** Magneto-optical image at $T = 2.5$ K and $B = 4.8$ mT, showing flux penetration in the form of thermomagnetic avalanches in Nb after cooling the sample in zero field (ZFC). **(e)** Magneto-optical image at $T = 2.5$ K and $B = 0$ mT, showing the remnant flux in Nb after withdrawing the applied magnetic flux density $B = 4.8$ mT (FC). **(d,f)** Magneto-optical images at $T = 10$ K and $B = 0$ mT, showing imprints of the flux avalanches in Nb visible in the HDD layer, after the ZFC and FC procedures, respectively.

vortices of opposite chirality penetrate the Nb film and anihilate with part of the trapped magnetic fux, leaving marks similar to the ZFC procedure (Figure 3.9 (e)). Again, the imprintings of vortices on the HDD are still present when the sample is warmed up above T_c. While this use of magnetic layers as a recording support still needs to be optimized, the high information density achievable by magnetic supports ($\sim$ 1 Tb/inch^2 [83]) promises the possibility of recording magnetic details of the magnetic landscape at the nanoscale. Coupling live MOI with post warm-up magnetic measurements via methods such as magnetic force microscopy would allow for both high temporal resolution during the evolution of the magnetic landscape with MOI and high spatial resolutions of the final vortex penetration pattern in superconductors.

Chapter 4

Flux penetration in YBCO thin films with a border indentation

4.1 Introduction

Vortex reorganization upon external field changes has been classified in Chapter 2 as either being dynamically driven or thermally driven. While the latter is characterized by a non repeatable magnetic flux pattern, the dynamically driven flux reorganization shows magnetic patterns that can be theoretically predicted very accurately. The exact form of the magnetic landscape in a superconducting sample depends on parameters such as the creep exponent n, the magnetic field dependence of the critical current $j_c(H)$, the sample geometry and the defect landscape of the sample. As such, the magnetic pattern observed by MOI acts as a fingerprint revealing the above described parameters unique to the investigated sample. The direct visualization of the magnetic landscape of entire samples gives us the possibility to quantitatively study the dependence of many of these parameters on the magnetic flux penetration pattern.

The highly non-linear $\boldsymbol{E}(\boldsymbol{j})$ relationship in superconductor exacerbates the importance of defects on current flow when compared to ohmic conductors. In particular, a micrometric edge indentation in a superconductor can influence the flux penetration from the very first vortex entering the sample up to complete magnetic flux penetration of the sample. The precise dependence on shape of the magnetic flux perturbation associated with an edge indentation is therefore central to the comprehension of real superconducting samples under magnetic field. In this chapter, we study square-shaped $YBa_2Cu_3O_{7-x}$ (YBCO) thin films with micrometric design features along their borders. We start by theoretically discussing the most noticeable patterns of dynamical magnetic flux penetration: the discontinuity lines (or d-lines) emerging from sharp turns taken by the screening currents. Next, we give a description of the samples observed. We then show the computer treatment applied to the experimental data and compare it with numerical simulations. Finally, once the detection algorithm is validated we study the

effect of both the geometry and the temperature on these d-lines.

4.2 Magnetic flux penetration in YBCO

YBCO is well known for its predominantly dynamical magnetic flux reorganization. Although thermomagnetic flux penetration has been observed, it requires either a strong perturbation of the local electric field via a laser pulse [44–46, 84] or an extremely fast ramping of the applied magnetic field (>250 T/s)[1], requiring specific set-ups [50,85–87]. Even with substrates having low thermal conductivity κ, thermomagnetic flux penetrations require high magnetic field sweeping rates at low temperature (<40 K) and are absent at high temperature up to YBCO's critical temperature ($\sim$ 90 K) [85]. This makes it the ideal material for characterising the magnetic patterns resulting from athermal flux reorganization in the whole temperature range.

Before describing the studied samples itself, we introduce the hallmarks of dynamical flux penetration which are the discontinuity lines (d-lines). We then present the numerical analysis done on magneto-optical images and compare it to predictions obtained by numerical simulations. Once the analysis validated, we compare the experimental data points to the Bean model's predictions and to similar work using Nb. Finally, the differences are explained and perspectives on the next step to predict d-lines exact shape are presented.

4.2.1 d-lines in superconductors

Consider a superconducting sample with geometrical shape of a cuboid with edges' length $w = l \ll h$ immersed in an applied magnetic field $\boldsymbol{H}_{\text{app}} = H_{\text{app}}\boldsymbol{z}$, as shown in Figure 4.1 (a). In this longitudinal geometry, the magnetic field and superconducting currents are independent from $\boldsymbol{z}$ as long as we are relatively far (compared to the London pentration depth λ) from the upper or lower faces (i.e. region where the demagnetization effect is low). The magnetic profile of a slice of the sample according to Bean's model is shown in Figure 4.1 (b) for an applied field generating screening currents in the entire slice, as shown in Figure 4.1 (c). Despite the presence of magnetic flux up to the center of the sample, we can observe a region devoid of magnetic field linking the corners of the square in a cross-like pattern. Looking at the screening current density, we can associate this region of lower magnetic field with the bending of the current lines to accommodate the sample's shape. Since these lines of lower field correspond to a discontinuity in the current direction, they are called discontinuity lines or d-lines. For another equivalent explanation of the lower magnetic field at the d-lines, it is possible to look at the forces acting on the vortices. As described in Chapter 2, vortices move in an overdamped medium, they velocity being proportional to the resulting

[1] For comparaison, the standard Cooper coil used in our set-up has a time constant of $\tau = L/R \approx 0.03$ s, limiting us to a rate of ~ 0.1 T/s.

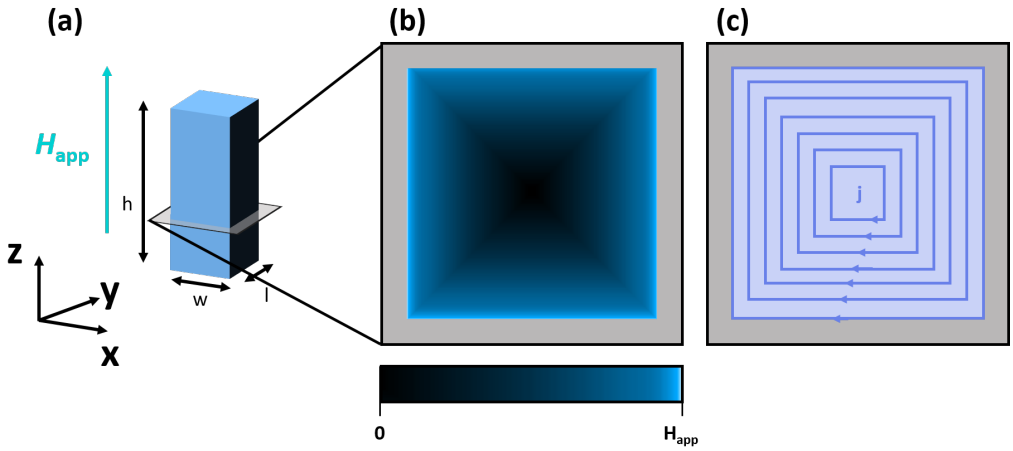

Figure 4.1: Magnetic flux penetration for a square-based superconductor in longitudinal configuration according to Bean's model. The geometrical arrangement is shown in **(a)**. Panel **(b)** shows the magnetic flux profile in a 2D slice away from the horizontal surfaces. Panel **(c)** shows the corresponding current density.

applied force on them. The main driving force of these vortices is the Lorentz-like force exerted by the screening currents and therefore their motion is perpendicular to the current streamlines. Upon arriving at the d-line, the change in current direction will forbid vortices from crossing from one magnetic flux front to the other, thereby acting as barriers for them.

Edges of the sample, geometrical defects on these edges, holes inside the superconductor, and local defects all contribute to change the direction of the screening currents and therefore create d-lines. As will be explained in more details in the next section, we focus our work here on edge indentations of micrometric size with predefined shapes, ensuring good control on the geometry of the defect. While the indentations in themselves can hardly be observed using MOI, the predicted disruption of the superconducting currents according to Bean's model span a much larger region, of the order of magnitude of the whole sample.

The effect of an edge indentation on the magnetic flux and screening current distributions has been addressed in the past from the theoretical side by Gurevich and Friesen studying the effect of a rectangular thin slit on these distributions [88, 89] whereas Vestgården *et al.* investigated the case of a semi-circular indentation [22]. Recently, Brisbois *et al.* studied lithographically defined micro-indentations of various shapes both experimentally and numerically [20], casting doubt on the role of triggering site for thermally driven flux reorganization. Numerical simulations by Jiang *et al.* [90] showed that the indentation's role as inhibitor or activator of thermally driven flux reorganization was explained by a difference of sweeping rate $\dot{H}$.

In order to compute the shape of the d-lines generated by an indentation, we must first note that in Bean's model, the only physical parameter used to

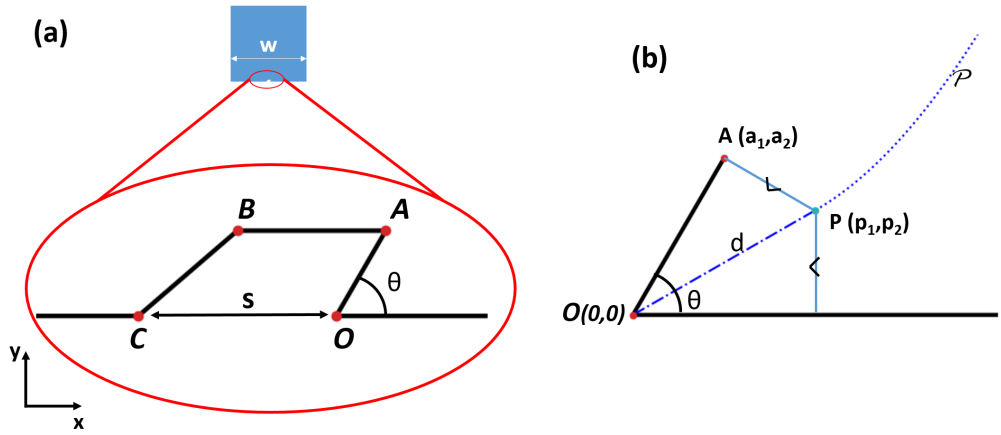

Figure 4.2: d-line (in blue) produced by a tetrahedral indentation along a superconducting edge (in black) based on the equidistance of the d-line from both superconducting edges. **(a)** Zoom on the central indentation of the lower edge of a square sample. The indentation is described by the coordinates of the vertices $O - A - B - C$. **(b)** Zoom on the right portion of the indentation. The d-line is composed of a linear portion d, bisecting the angle θ (dash-doted line), and a parabolic portion,$\mathcal{P}$ (dashed curve).

describe the superconductor is the critical current density j_c. From this j_c and the assumption of a critical state in the sample, we obtain the magnetic flux density $\boldsymbol{B}$ from the equation $\boldsymbol{j} = \frac{\nabla \times \boldsymbol{B}}{\mu_0}$. Since the d-lines appear at the meeting of two flux fronts and the gradient of magnetic flux is constant in the whole sample (*i.e.* the current stream lines must be equidistants), the problem of finding the shapes of the d-lines emerging from two edges is reduced to a geometric one. Thus, within Bean's model, the d-line produced by two adjacent edges coincides with the curve starting at their meeting point and equidistant from both edges. For films thinner than the London penetration length λ as is the case for our samples, the current distribution inside the superconductor can be modelled using a 2D current sheet. The result is an identical magnetic landscape for both situations if we correct the applied field to take into account the demagnetization factor of the thin film.

Let us now derive the explicit form of the d-lines produced by a quadrilateral indentation of length s at the center of an otherwise straight edge of length w, with $s \ll w$, as shown in Figure 4.2(a).

Since the d-lines emerge from the meeting of two adjacent edges, we treat the d-lines emerging from O and C separately. The role of the indentation's upper edge $\overline{AB}$ will be discussed later. Starting with the geometry of Figure 4.2(b), the d-line can be decomposed into two regions. In the region closest to O, it takes the form of a straight line bisecting the angle θ. Further inside the sample, it follows a parabolic curve with both curves meeting in a single point P. Let us compute the exact shape of the d-line produced by the corner of Figure 4.2 (b). The straight

line portion is described by the equation

$$\begin{aligned} d \equiv y &= \tan(\frac{\theta}{2})x \\ &= \tan(\frac{1}{2}\arctan(\frac{a_2}{a_1}))x \\ &= \frac{-x}{a_2}\left(a_1 - \sqrt{a_1^2 + a_2^2}\right), \end{aligned} \tag{4.1}$$

where a_1 and a_2 are the coordinates of the point A. This equation describes the d-line up to the point $P = (p_1, p_2)$ where the distance between A and d equals the distance between the x axis and d. That is,

$$p_1 = \sqrt{a_1^2 + a_2^2} \tag{4.2}$$

and

$$p_2 = a_2 - \frac{a_1}{a_2}\left(-a_1 + \sqrt{a_1^2 + a_2^2}\right). \tag{4.3}$$

Further inside the sample, in the parabolic region, the distance between the d-line and the x axis is equal to the distance between the d-line and A. That gives us the parabolic equation

$$\begin{aligned} y^2 &= (x - a_1)^2 + (y - a_2)^2 \\ \Rightarrow \mathcal{P} \equiv y &= \frac{(x - a_1)^2}{2a_2} + \frac{a_2}{2}. \end{aligned} \tag{4.4}$$

A similar reasoning can be made for the other section of the indentation. The final set of equations for the left and right d-lines takes the form [91]

$$d_l \equiv y = -\frac{x}{a_2}\left(a_1^2 + a_2^2\right) \qquad d_r \equiv y = \frac{x - s}{b_2}\left(s - b_1 + \sqrt{b_2^2 + (s - b_1)^2)}\right)$$

$$\mathcal{P}_l \equiv y = \frac{(x - a_1)^2}{2a_2} + \frac{a_2}{2} \qquad \mathcal{P}_r \equiv y = \frac{(x - s)^2}{2b_2} + \frac{b_2}{2}$$

meeting at the point P_l and P_r of coordinates

$$x_{P_l} = -\sqrt{a_1^2 + a_2^2} \qquad x_{P_r} = w + \sqrt{(w - b_1)^2 + b_2^2}$$

$$y_{P_l} = a_2 + \frac{a_1}{a_2}\left(a_1 + \sqrt{a_1^2 + a_2^2}\right) \quad y_{P_r} = b_2 + \frac{w - b_1}{b_2}\left(w - b_1 + \sqrt{(w - b_1)^2 + b_2^2}\right).$$

Let us finish the discussion of d-lines in the Bean model by talking about the effect of the corners OAB and ABC. Here too, the current must change direction in order to follow the edge. However, due to its counter-clockwise rotation, this change in current direction increases the magnetic field penetration. While these two lobes of increased magnetic flux are theoretically present, they are significantly harder to detect experimentally.

The predictions made here are subject to a number of assumptions. The most radical approximation is the first critical magnetic field value fixed at $H_{c1} = 0$. This assumption removes any surface barrier potentially present in the superconductor, thereby setting the field of first vortex penetration H_p to zero too. It has been speculated that this neglect of surface barriers is at the orgin of substantial discrepancy between the d-lines predicted by Bean's model and the ones observed experimentally [20]. In addition, this model corresponds to the extreme case of a creep exponent $n \to \infty$ in the constitutive relation $E = E_c(j/j_c)^n$ and a simple magnetic field independant critical current relationship. More realistic models including finite n and field dependent critical currents seem to suggest that little additional differences should be expected when these ingredients are incorporated [20].

4.2.2 Experimental observations

To confront these predictions of Bean's model and the associated shape of the d-lines, we studied 100 nm-thick square YBCO thin films of dimensions 800 µm × 800 µm. The epitaxial YBCO was grown on a $LaAlO_3$ substrate by chemical solution deposition [92,93]. Photolithography masks where made by direct-writing on a photoresist of the squares with indentations at the center of each side with a micro-writer system with laser-assisted technology (ML3 from Durhan Magneto Optics Ltd). The pattern was dry etched in the YBCO film via ion milling. The fabrication procedure was done in the group of Anna Palau at the Institute of Material Science of Barcelona. The critical temperatures of the films were estimated using MOI[2] at $T_c \sim 87$ K.

Part of the experimental measurements were realized in the group of superconductivity and magnetism lead by Prof. Wilson A. Ortiz at the University of São Carlos. The Oxford Instruments continuous flow MicrostatHe cryostat used for these measurements allows to reach temperatures from 2 K to room temperature. The optical apparatus used for MOI is similar to the one described in Chapter 3. The applied magnetic field perpendicular to the film is generated by a Cooper coil placed outside of the cryostat allowing for a maximum field of 15 mT. To ensure a minimal number of magnetic artefacts in the Bi:YIG indicator, a fixed in-plane magnetic field is applied by using a permanent magnet.

The samples were zero field cooled down to the desired temperature (40 K, 60 K or 70 K) for each of which a stepwise magnetic field increase was applied. Since the magnetic field corresponding to a complete magnetic flux penetration depends on the temperature, the sweep was adjusted accordingly for each temperature although keeping the same magnetic field step at 0.1 mT. At regular intervals during the sweep, the magnetic field was held constant to acquire multiple images,

[2]This has been estimated via a FC procedure down to the base temperature, turning the applied field off and taking pictures while warming the sample. By subtracting consecutive images taken at slightly different temperatures, we deduce the T_c when the differential picture cannot be distinguished from noise.

increasing the signal-to-noise ratio for a given field.

4.2.3 d-lines detection method

The numerical processing of the images starts with an alignment of all the pictures taken during a magnetic flux sweep in order to correct for drifting of the sample due to thermal contractions inside the cryostat. This is done using the ImageJ software [94] with the TubroReg [95] plug-in performing a rigid body rotation on the image to be corrected to match the first image of each series, and the StackReg [95] plug-in automating the process for all the images in the series. Next, a home-made python script averages all the aligned pictures taken at a given magnetic field. To minimize the influence of uneven lighting, a 2D parabolic background is then fitted on the image taken at $\mu_0 H = 0$ mT and images from this set are divided by this background, as discussed in Chapter 3. The corrected images are rotated to ensure that the edges of the samples are aligned with the x and y axis. Finally, a Gaussian blur of radius 1 px is applied, smoothing the noise in the image.

Next, to find the pixels belonging to a d-line, we delimit a rectangular region of interest around the indentation. Although these lines are more prominent in thin films than in bulk superconductors, it represents a challenge to identify an unambiguous criterion to experimentally track them. The loci of the d-lines is determined by subtracting a smooth polynomial background to each individual pixel line parallel to the sample's edge and then introducing two thresholds for the onset of the central peak. These two thresholds naturally define the extremes of an error bar within which the d-line is expected to lie.

To ensure proper detection on the d-lines, we first run the algorithm on a numerical simulation of the magnetic flux encountered at 5 µm above a superconducting thin film, mimicking the vertical gap between the magneto-optical indicator and the superconducting sample. The finite element method simulation, generated by Loïc Burger at the Electronics Research Group of University of Liège, represents a 200 µm-long and 100 nm-thick film with a rectangular indentation of 8.5 µm × 10 µm at the center of the sample's lower edge. To test the robustness of the algorithm, a Gaussian noise typical for the experimental images is added to this simulation. The similar noise level of the experimental and simulation images is confirmed in the maroon curves of Figure 4.3 (a), representing the light intensity along a pixel line parallel to the sample's edge. Figure 4.3 (b) shows the resulting d-line containing regions, giving reasonable results both in the simulation and the experimental case.

4.2.4 Experimental d-lines in YBCO

We now compare the experimental d-lines obtained with the predictions from Bean's model. First, different indentations are compared under a single magnetic field and at a fixed temperature of 60 K. Next, we show the effect of varying the

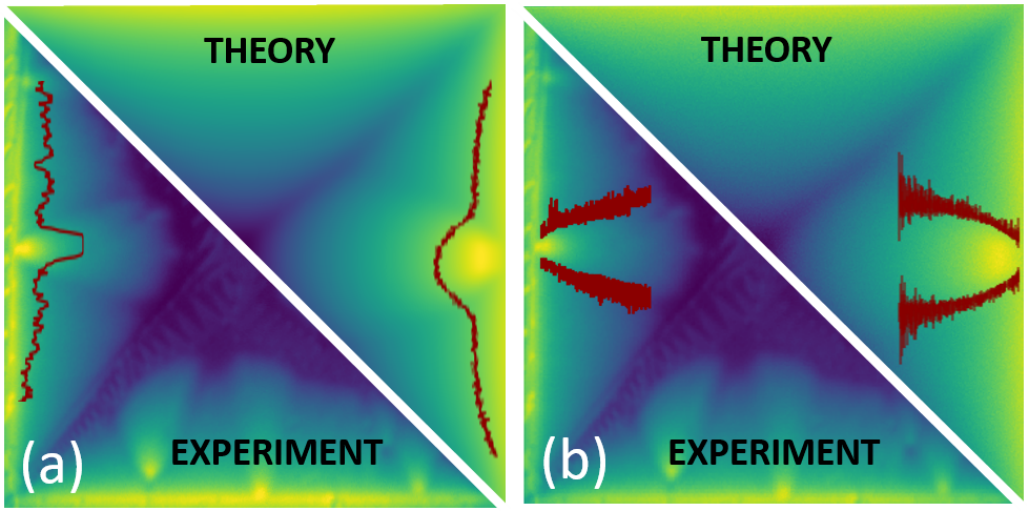

Figure 4.3: Comparaison of experimental MOI data with numerical simulations with added Gaussian noise for YBCO thin films. **(a)** Intensity profiles of a pixel line parallel to the sample's edge. **(b)** Regions containing the d-line as given by the two thresholds detection method.

temperature (thereby affecting n, j_c, and H_{c1}) on the shape of the d-lines.

Effect of geometry

Figure 4.4 shows the d-lines of six indentations having different geometries for an applied magnetic field of $\mu_0 H = 10$ mT at a temperature of $T = 60$ K, corresponding to a reduced temperature $T/T_c = 0.69$. The red regions correspond to the experimental detection while the underlying salmon curves correspond to the predictions of Bean's model. The overall good agreement with the theoretical predictions can be contrasted with previous experiments on micro-indented Nb thin film performed at similar T/T_c [20], where the observed increase in the curvature of the parabola compared to the predictions of Bean's model was established to be several times bigger than the error bar.

Effect of temperature

Brisbois *et al.* [20] noticed in Nb a widening of the d-line parabolic part as the temperature increased. The curvature was halved when passing from $T/T_c = 0.45$ to $T/T_c = 0.9$. In contrast, Figure 4.5 shows no temperature dependence of the d-lines for the YBCO samples.

4.2.5 Discussion

A number of factors can explain the difference of behaviour between the Nb and the YBCO thin films. Since the relevant physical parameters are linked, it is hard

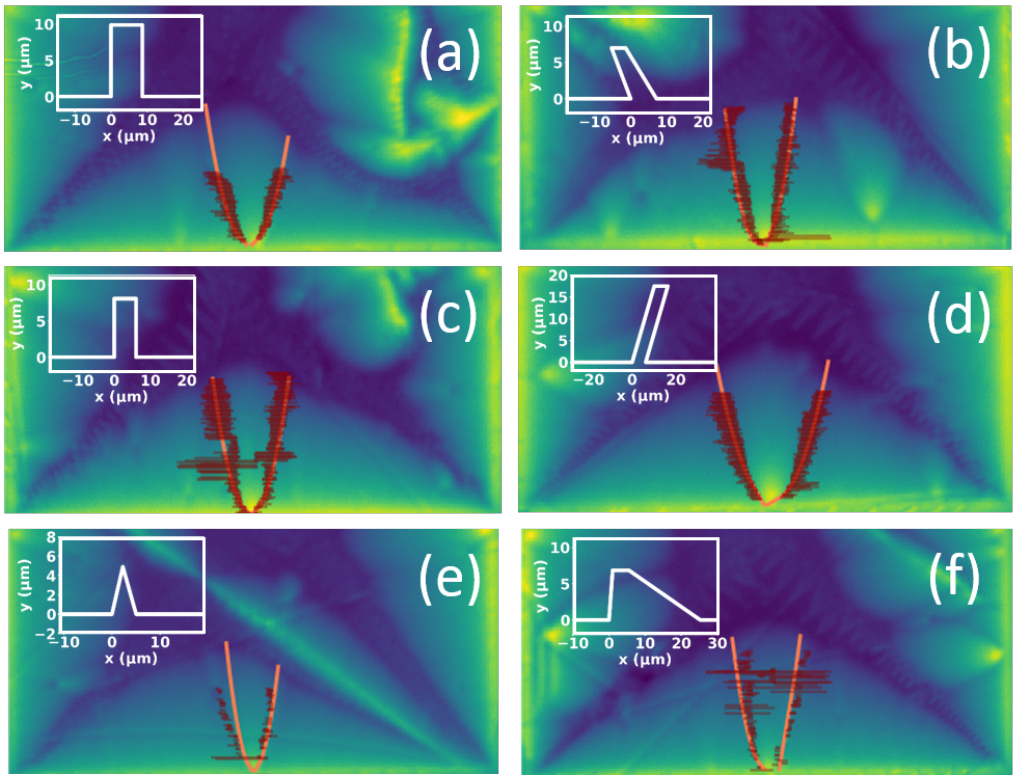

Figure 4.4: Influence of indentation shape on d-lines for various indentations. The shape of each indentation is represented in white. The picture represents magneto-optical images of the magnetic landscape under $\mu_0 H = 10$ mT at $T/T_c = 0.69$. The blue regions correspond to low magnetic field regions while the green-yellow regions are those with the highest magnetic field values. The salmon curves show the predictions of Bean's model for the different indentations while the maroon marks show the detected d-lines.

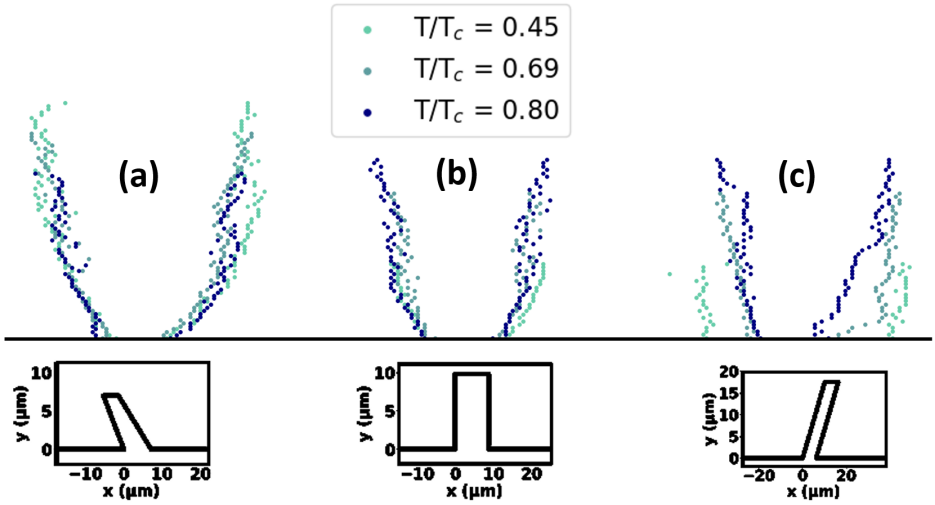

Figure 4.5: Influence of temperature on d-lines for various indentations. No noticeable change in the d-line profile can be noticed as the temperature increases. For clarity, the plotted points correspond to the center of the d-line regions.

to know for sure what parameter leads to a Bean-like flux penetration.

One of the assumptions of Bean's model is that the magnetic flux starts to enter the sample as soon as an external field is applied. The existence of surface barriers and a lower critical field $H_{c1} \neq 0$ makes this assumption unrealistic. While the precise value of the magnetic field at which the first vortex nucleates, H_p, is hard to predict, it is bounded in its lower value by H_{c1} ($\mu_0 H_{c1,\mathrm{YBCO}} = 5$ mT, $\mu_0 H_{c1,\mathrm{Nb}} = 180$ mT [25]), leading in the lower bound estimation to $H_{p,\mathrm{YBCO}} \ll H_{p,\mathrm{Nb}}$. The close agreement of YBCO's d-lines to theory combined with the poor agreement of Nb's d-lines points toward the reasonability of this assumption and would indicate the importance of the surface barriers in the final shape of the d-line. This is a notable exception, as surface barriers are notably hard to highlight with magnetic measurements in dirty superconductors due to bulk pinning in the sample [96].

In addition, as demonstrated by the d-lines, indentations, even of small size, play a role in the flux penetration. The natural roughness and defects at the edge act as facilitators for magnetic flux penetration, thereby reducing H_p. It has been observed that YBCO films with twinning defects shows no surface barriers, contrary to untwinned YBCO samples [97]. The presence of these twinning planes combined with the smaller coherence length of YBCO (1.4nm) could lower its average surface barrier. Nb having a bigger coherence length (38nm) and no twinning planes, this mechanism prevents the existence of large surface barriers for Nb films.

Finally, the comparison between the currents of a thin film and a 2D slice of the Bean model is only approximative. It is acceptable for a thickness d smaller

than λ and the samples in the Nb study [20] had a ratio $d/\lambda = 2$ while in the present case, $d/\lambda = 0.76$. It is therefore expected that thinner Nb films or thicker YBCO films might have behaviours closer from one another.

4.3 Future work

This study of edge indentations showed that d-lines can be properly and quantitatively accounted for in thin YBCO films by Bean's model of critical state, contrary to previous observations in Nb films. YBCO and Nb consist of extreme cases regarding their H_p values and it would be interesting to look at superconductors with intermediate H_p with lithographically controlled roughness, or investigate the influence of tilting the applied magnetic field. One of these alternative superconductor would be NbN which has a $H_{c1} = 9$ mT close to YBCO but whose vortex core are five times larger, of the order of $\xi_{\mathrm{NbN}} = 6.5$ nm. Another would be MgB_2 which has a $H_{c1} = 110$ mT, close to the value of Nb and a $\xi_{\mathrm{MgB_2}} \approx 12$ nm, while having a London penetration length of $\lambda = 1$ µm, ensuring the validity of the 2D approach for films of similar geometry. A cleaner comparison however could come from the difference of d-line patterns between untwinned and twinned YBCO film as this would have a minimal influence over all parameters except the surface barriers.

The question of the d-lines emerging from a defect inside the sample is still unanswered. In light of our results, it can be reasonably assumed to follow Bean's model for YBCO but should be verified experimentally for other materials. Numerical studies of the flux penetration for holes inside YBCO wires have shown that in order to maximize the trapped flux, the successive holes must be placed on the d-lines generated by the previous ones [98]. A YBCO sample with an array of holes would provide experimental confirmation of this prevision. In the context of holes, the differences between Nb and YBCO is expected to diminish due to the lesser role of H_p in the flux penetration further away from the sample's edges. While studies of dense anti-dots array have been realized on Nb [99], the comparison of sparser arrays of anti-dots for both materials could shed light on the reasons for the discrepancy in d-line shapes between them.

Finally, the better comprehension of the interplay between the shape of d-lines inside a superconductor and its surface barriers could provide a new tool for a spatially resolved study of the different surface barriers in a superconductor.

Chapter 5

Statistics of thermomagnetic breakdown in Nb superconducting films

This chapter is largely based on the following work:

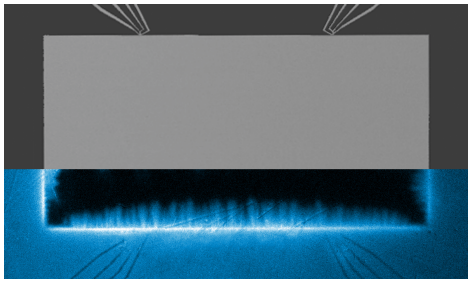

"Statistics of thermomagnetic breakdown in Nb superconducting films."
S. Blanco Alvarez, J. Brisbois, S. Melinte, R. G. B. Kramer & A. V. Silhanek, Scientific Reports, **9** 3659 (2019).

5.1 Introduction

In the previous chapter, we have shown the predictability of dynamically driven magnetic flux penetration. The magnetic landscape, described by Bean's critical state model, can be viewed as the magnetic parallel of a sandpile where vortices take the role of individual grains. The addition of new grains of sand to the pile creates local stackings where the slope exceed the angle of repose of the sand. This unstable configuration leads to grains moving down the sand pile, increasing the slope further down the pile and possibly triggering other rearrangement of sand. In this analogy where vortices act as grains of sand, the angle of respose correspond to the variation $\partial B_z/\partial x$ of the magnetic field in the film's direction perpendicular to the closest edge and holds at temperatures close to T_c. In this regime, the heat produced by the vortex motion is easily dissipated and the rearrangement of the landscape can be considered isothermal.

When the bath temperature T_0 is decreased or the magnetic field ramping rate $\dot{H}$ is increased, the heat evacuation is insufficient to maintain an isothermal rearrangement. Vortex motion being promoted by temperature increases, this added effect breaks the analoy with sandpile and the resulting positive thermal feedback loop creates patterns, refered here as magnetic flux avalanches and reminiscent of Lichtenberg figures. These non-repeatable magnetic flux patterns [54] disrupt the magnetic landscape and, contrary to magnetically driven flux penetration, destroy the critical state of the sample [100].

The sudden disruption of a metastable critical state is characteristic of breakdown phenomena, present in a variety of systems. In breakdown experiments, a sample is placed under an monotonically increasing stress σ_i until it hits the stress threshold σ_{th} necessary for the sample to fail. Breakdown phenomena are numerous and include events such as the dielectric breakdown of a capacitor under an increasing tension, electromigration of integrated circuit lines due to current or even the explosion of a corn kernel under its increasing internal pressure when heated up.

In these ramp-to-failure tests, one observe that rather than associating a single σ_{th} value to a breakdown phenomenon, the physics is better described by a probability density function (PDF) giving the probability that failure occurs at a given stress σ_i. Due to the destructive nature of ramp-to-failure tests, probing for this PDF necessitates a large number of replicas. This creates two unfortunate consequences. First, these experiments are costly and time consuming due to the multiplication of samples. Second and more importantly, each replica possess small intrinsic particularities giving rise to a spread in σ_{th} extrinsic to the physical phenomenon but inseparable from the intrinsic spread associated to the physics at play. By contrast, while increasing the applied magnetic field up to its threshold value H_{th} creates thermally driven flux penetration, the phenomenon leaves the sample intact and warming up the sample above T_c allows to reset the experiment with the exact same sample. Type-II superconductors are therefore ideal playgrounds for studying breakdown phenomena.

Knowing that, it might come as a surprise to learn that as of today, there are neither theoretical predictions nor experimental investigations of the statistical distribution of H_{th}. On the one hand, while theoretical simulations have been successfully used to emulate flux avalanches and deduce some of their properties [21,101], they still fail to capture the stochasticity of the process. On the other hand, the lack of experimental information can be tracked back to the techniques used to estimate H_{th}. Magnetization measurements offer the possibility to identify H_{th} as the magnetic field at which the first magnetization jump is detected. Unfortunately, these studies based on Hall probe arrays and global magnetization measurements conceal information about the different nucleation spots in the sample, the size of individual avalanches and their morphology. Alternatively, a more reliable and direct approach consists in visualizing the magnetic field profile through the magneto-optical imaging (MOI) technique.

In all cases, the resetting of the sample to the initial condition requires to warm it up above the superconducting transition temperature T_c and to cool it down in zero field back to the working temperature T_0. Since flux avalanches only develop at $T_0/T_c < 0.5$, the typical resetting takes several minutes, thus severely undermining the possibility to collect enough data to reliably determine the PDF. In this chapter, we shorten the time necessary for a thermal cycle by introducing planar nanoheaters alongside the Nb rectangular thin film studied.

With the possibility to collect a large number of events via MOI, we study the PDF associated with thermally driven magnetic flux penetration. Studying the size distribution of the different vortex reorganization occurring as the field is increased illustrate clearly the contribution of both the magnetically driven and the thermally driven magnetic flux penetration. This in turn allows us to define a criterion to separate both events and with that, determine precisely the threshold magnetic field H_{th} and its distribution probability with unprecedented resolution. Taking advantage of the spatial resolution of MOI, we study the correlation between dynamically driven and thermally driven magnetic flux penetration. Finally, repeating the statistical analysis at several temperatures, we highlight the presence of two distinct H_{th} distributions corresponding to small and large avalanches, peaking respectively at low and high magnetic fields and coexisting at intermediate temperatures.

5.2 Experimental details

5.2.1 Sample configuration

The experiments were conducted on a 100 nm-thick Nb film prepared in a home-built electron beam UHV evaporator. To ensure electrical insulation, a 100 nm-thick SiO_2 layer was evaporated on top of the monocrystalline (100) Si substrate. Details concerning the evaporation parameters can be found in Ref. [20]. The choice of material has been largely motivated by the extensive investigations already reported in the literature of magnetic flux avalanches in Nb [34, 102–106].

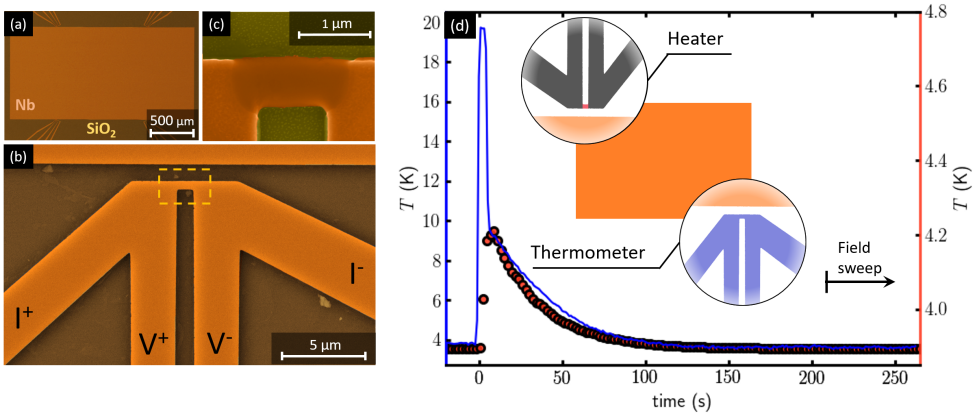

Figure 5.1: Sample layout and local thermometry configuration. Scanning electron microscopy details of the investigated sample. **(a)** Layout of the rectangular Nb film with four thermal elements symmetrically placed along the long sides. **(b)** Zoom-in on one of the as-fabricated Nb thermal elements, highlighting the central bridge. **(c)** Most of the voltage drop takes place in the short Nb bridge made non-superconducting via electroannealing, corresponding to the dashed yellow rectangle in panel (b). The inset in panel **(d)** shows the configuration used for tracking the temperature of the substrate with one thermal element used as a nanothermometer, while exciting the diagonally opposed nanoheater with a 7 mA current during 5 s. The blue continuous line in panel (d) shows the time evolution of the sample temperature detected by the nanothermometer (left axis) and the red dots correspond to the temperature change detected in the cold finger thermometer (right axis). MO measurements start with a magnetic field sweep one the temperature of the substrate has been stabilized, as indicated by the black arrow.

The thin film was patterned using electron beam lithography followed by a reactive ion etching process. The layout of the sample investigated in this work is summarized in Figure 5.1 (a). It consists of a rectangular Nb film of 2 mm $\times$1 mm and four thermal elements made of the same material symmetrically placed along the long side of the rectangular sample.

In their as-fabricated state, the thermal elements can only be employed as nanoheaters when fed with currents above the superconducting critical current of Nb. However, by performing a controlled electroannealing process [47], we are able to locally change the material properties and render them non-superconducting. Figure 5.1(c) shows a scanning electron microscopy image, corresponding to the yellow dashed rectangle of panel (b), after the central part of the nanoheater has been modified by electroannealing. During this process the normal state resistance changes from 5 Ω in the as-fabricated state to 50 Ω after electroannealing. Although one single nanoheater should suffice, they are fragile against electrostatic discharges and chances of obtaining a successful operational device scale with their number. In addition, each nanoheater can also be used as a local thermometer allowing to monitor the temperature evolution of the sample during each cycle.

In panel (d) of Figure 5.1 (blue curve), we record the T modulations picked up in one nanothermometer caused by the heating produced by a 5 seconds current pulse in the diagonally opposed nanoheater (see inset). The sample temperature reaches a maximum value of 20 K, well above the superconducting critical temperature of Nb ($T_c = 9.0$ K). Once the excitation is switched off, the recovery to the initial temperature is characterized by two well distinguished relaxation times: a rapid exponential decay of the substrate temperature to the temperature of the cold finger ($\tau_1 = 0.7$ s) followed by a slower thermalization of the cold finger to the bath temperature ($\tau_2 = 32$ s). The slow relaxation of the latter is corroborated by the temporal evolution of the cold finger thermometer, as shown by the red dots in Figure 5.1 (d).

It is worth noting that both decay times are much larger than the intrinsic relaxation time of the Si substrate once the heater is switched off, estimated as [107, 108] $\tau = l^2\rho C/\kappa \approx 10^{-6}$ s, taking the density $\rho = 1$ g.cm^{-3}, $l = 1$ mm, the heat capacity $C = 1.6 \times 10^{-5}$ J.K^{-1} and the thermal conductivity $\kappa = 2.97$ W.cm^{-1}.K^{-1}. In other words, the high thermal conductivity of the substrate κ combined with a low heat transfer coefficient h between the substrate and the cold finger, leads to a large thermal healing length $\delta = \sqrt{\kappa t/h}$, with t the substrate thickness. This ensures a rather uniform heating of the entire sample when using a single nanoheater.

5.2.2 Visualization of the magnetic flux penetration

Direct visualization of the magnetic flux landscape was obtained by the MOI technique explained in chapter 3, using a Bi:YIG Faraday indicator with in-plane magnetization. Post-image processing was done to remove the inhomogeneous illumination and field-independent background, using the ImageJ software. Low

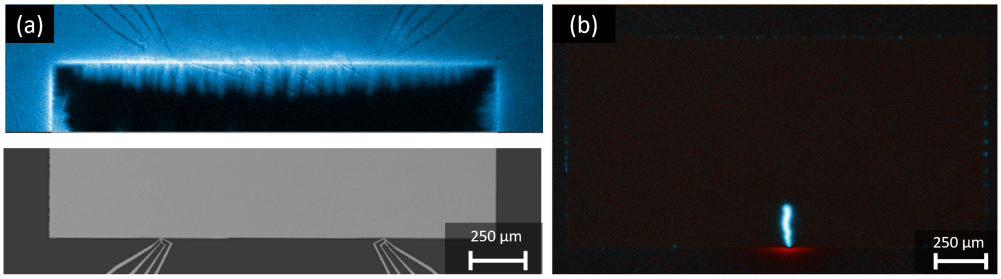

Figure 5.2: Magneto-optical images of the Nb rectangle. **(a)** MOI of the sample's magnetic flux penetration at 7 K for a magnetic field H applied perpendicularly to the sample, with $\mu_0 H = 1.85$ mT. The lower part of the picture shows the corresponding SEM image. While the broad leads far from the Nb sample are visible as darker path, no effect on the smooth magnetic flux penetration can be observed at the position of the heaters. **(b)** Differential MO image of the Nb film at $T = 3.83$ K. White-blue (red) regions correspond to positive (negative) field variations, while dark regions correspond to undetectable field variations.

temperature MO measurements are performed in a closed-cycle cryostat and the external magnetic field was applied through a copper coil with resistance R = 22.1 Ω and inductance $L = 26$ mH. The small magnetic field changes detected by MOI (~ 10 μT) are to be compared with the smallest magnetization change 50 μT picked up by a superconducting quantum interference device (SQUID) with typical sensitivity of 10^{-8} emu, on the entire sample [109]. More importantly, unlike such specimen-average measurements, MO imaging allows to record spatial maps of the magnetic flux and thus obtain direct information on the location and size of each event.

Since the four thermal elements are made of the same superconducting material as the rectangular Nb film, it is pertinent to wonder about their influence on the local penetration of flux in the Nb film. Their small dimensions, shown in Figure 5.1 (b), are intended to minimize the perturbations on the magnetic field distribution and consequently, on the flux penetration into the rectangular Nb film despite their proximity with the film. If no current circulates in the circuit, the screening Meissner currents will expel the magnetic field from the device, giving rise to a concentration of magnetic flux lines in the 1 μm gap separating the device from the border of the Nb film. It is precisely the presence of this screening effect which permits to visualize the Nb wires of the inactive thermal elements in the magneto-optical image shown in the upper part of Figure 5.2.

Note first that if the central part of the nanoheater has been modified by electromigration, it becomes a normal metal and therefore interrupts the Meissner currents and their associated effects. If no electromigration process has been practiced on the heating element, the flux focusing effect [110] has to be taken into account. Simple arguments based on the field distribution around a supercon-

ducting film [111] indicate that such perturbations of the magnetic field can be ignored. Indeed, on the one hand the magnetic field at the border of a Nb strip $B_z \sim (w/d)^{1/2} B_{\rm app}$ of width w and thickness d, largely exceeds the applied field $B_{\rm app}$. On the other hand, the field perturbation with respect to $B_{\rm app}$ decreases rapidly within a distance $\sim w/4$ from the border of the sample. Based on the fact that the nanoheater width is about 1 μm and the distance from its border to the border of the film is on the same order, the nanoheater produces a negligible perturbation of the magnetic field at the border of the film.

We have verified experimentally that no influence of the heating elements is observed by inspecting the MOI obtained at 7 K, for perpendicular applied fields from 0 Oe to 50 Oe by steps of 0.25 Oe. At this temperature, no thermomagnetic instabilities take place and the flux penetration tends to follow the Bean profile, as shown in the magneto-optical image of Figure 5.2 (a) recorded at $H = 18.5$ Oe.

It is worth emphasizing that there are no effects associated to the field generated by the large currents applied to the heater since when the heating elements are active, no external field is applied and no measurements are acquired.

5.3 Results

5.3.1 Quantitative criterion for thermomagnetic breakdown

In the study of magnetic flux penetration in chapter 2, we distinguished the smooth magnetic flux penetration described by the critical state model [34,35] and studied in the previous chapter from the regime dominated by thermomagnetic instabilities [51], subject of the current chapter. In the former case, the thermal diffusion coefficient $D_{\rm t} = \kappa_{\rm Nb}/C_{\rm Nb}\rho_{\rm Nb}$, where $\kappa_{\rm Nb}$ is the thermal conductivity of the superconducting material, $C_{\rm Nb}$ its specific heat and $\rho_{\rm Nb}$ its density, exceeds the magnetic diffusion coefficient $D_{\rm m} = 1/\mu_0\sigma_0$, with σ_0 the normal state electrical conductivity and μ_0 the vacuum permeability. In other words, the heat generated by the magnetic flux motion is rapidly distributed in the entire sample before further flux motion develops. In the opposite situation where $D_{\rm m} \gg D_{\rm t}$, rapid magnetic flux diffusion takes place while leaving behind a trail of overheated material which slowly diffuses.

The two main distinctive features of thermally driven flux avalanches are (i) a supersonic flux propagation [34], and (ii) a high temperature wake left along their paths [112]. Most of magneto-optical studies reporting on avalanches produced by thermomagnetic instabilities are based on static pictures and hence they lack the time resolution needed to track the evolution of the flux propagation, neither are they sensitive to the local temperature distribution. Therefore, conclusions as to whether an magnetic flux reorganization belongs to one regime or the other are based on seemingly speculative arguments such as their size. This approximate conjecture is nevertheless valid for extreme cases of large flux burst, but certainly becomes unreliable for small avalanche sizes. The associated uncertainty is particularly prominent for the case of the first avalanche defining the transition point

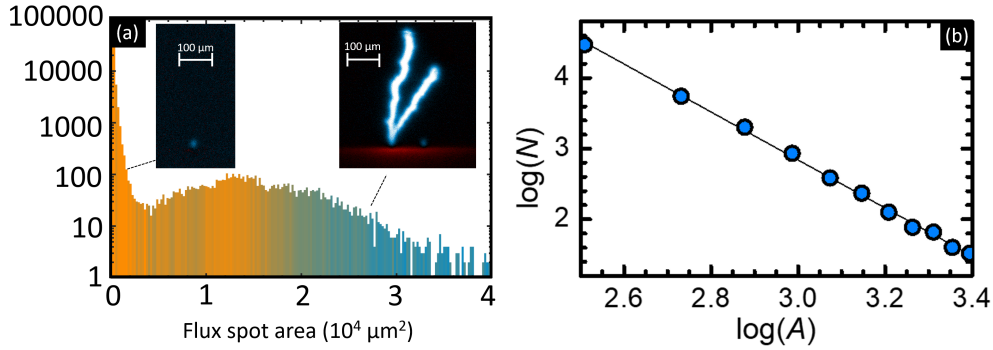

Figure 5.3: Statistical distribution of magnetic flux avalanches size. **(a)** Distribution of the avalanche sizes obtained from 79726 recorded events during 813 field sweeps from 1.4 mT to 2.5 mT. The graded color in the histogram indicates the mean field value at which the avalanches occur, from $\mu_0 H = 1.775$ mT (orange) to $\mu_0 H = 2.475$ mT (blue). The insets in panel (a) show that dynamically driven flux penetration (left) exhibit a more rounded shape, whereas thermally driven avalanches (right) are elongated. Panel **(b)** shows the distribution of the number N of avalanches as a function of their size A in μm^2. The black line corresponds to a linear adjustement and gives a critical exponent $\alpha = 3.4$.

$D_\mathrm{m} \sim D_\mathrm{t}$ at a threshold magnetic field H_th and therefore, early determinations of H_th are inaccurate.

We will now show that a rigorous statistical analysis of the avalanche distribution permits to overcome this deficiency of the MOI technique and to precisely distinguish a dynamically driven (nearly isothermal) from thermally driven (adiabatic) magnetic flux reorganization. The measurement protocol consists in a zero-field cooling to the working temperature T_0, followed by a step-wise $\delta H = 0.25$ Oe magnetic field sweep between $H_\mathrm{min} < H_\mathrm{th}$ and $H_\mathrm{max} > H_\mathrm{th}$. Subsequently, the magnetic field is turned off and a delay much larger than the time constant of the coil (~ 1 ms) is imposed before heating the whole substrate with one nanoheater. The nanoheater is active during 5 s, ensuring a complete removal of the magnetic history of the sample, as directly verified by MO images inspection. Once the heater is switched off, a delay of 210 seconds is respected in order to guarantee that the system has recovered the initial temperature T_0. This time has been experimentally determined by warming up with one heating elements and monitoring the temperature change in the diagonally opposed heating element, as shown in Figure 5.1 (d). This procedure has been repeated 2000 times thus collecting about 1.5×10^5 images for a given temperature.

Magnetic flux changes are identified by subtracting consecutive images as illustrated in Figure 5.2(b). The most salient feature of this differential image is the lightening-like magnetic flux burst at the lower center of the sample. The white-blue color indicates an increase of magnetic field intensity, whereas the red-white

color points to a local decrease of the field magnitude resulting from decompression of magnetic field lines, sign of the perturbation of the critical state [100]. A careful inspection of this image shows small flux changes all along the border of the sample. The digital images allow for a precise estimation of the area covered by each magnetic flux change and thus the size of the avalanches.

The flux reorganization's frequency of appearance as a function of size is presented in Figure 5.3(a) in semi-log scale and with a color grade indicating the mean value of the magnetic field at which the avalanche has been triggered. Interestingly, a bimodal distribution is observed. Indeed, although the frequency of appearance of flux reorganizations tends to monotonously increase as the size of the event decreases (a general trend also reported for earthquake and granular avalanches distributions), a clear broad peak at large reorganization sizes is observed. This second peak is a unique fingerprint associated to avalanches initiated by a thermomagnetic instability which has no counterpart in the earthquake and granular avalanches analogies [104]. According to this description, the minimum in the size distribution indicates the transition between these two regimes and it could be used as a criterion to determine the first flux avalanche triggered by a thermomagnetic instability.

5.3.2 Dynamical flux reorganization

When a magnetic field is applied to the superconducting film, the system can relax the magnetic pressure built up at the sample border either through dynamically driven avalanches (i.e. non thermal) or via thermomagnetic avalanches. As shown in Figure 5.3(b), the dynamically driven avalanche regime typically correspond to small size events in the bimodal distribution. It has been long argued that within this regime signatures of self-organized criticality could be observed.

According to the theory of self-organized criticality, the probability P of an avalanche involving N vortices follows a power law $P(N) = N^{-\alpha}$, reflecting the scale invariant nature of the phenomenon. A critical exponent $\alpha = 3$ for Nb foils has been obtained by Altshuler and co-workers from combined MOI and Hall magnetometry [113]. In Figure 5.3 (b), we plot the distribution of the number of avalanches as a function of their size in the range corresponding to the first mode of the distribution in Figure 5.2 (a). A linear fitting, represented by the black line in the log-log graph, gives a critical exponent $\alpha = 3.4$, which is close to the value reported in previous studies [113].

5.3.3 Thermal flux reorganization

Unfortunately, the statistical criterion seems of little practical use since it requires as prerequisite to accomplish the whole statistical analysis. A more functional approach to discriminate between dynamically and thermally driven flux reorganization is to look at the ratio $\varepsilon = L/W$ characterizing the geometrical shape of the magnetic flux penetration, where L and W are its length and width. Indeed,

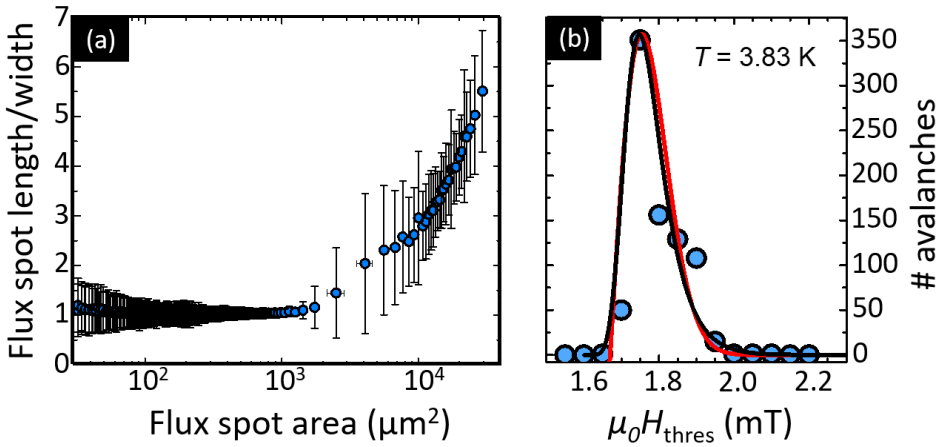

Figure 5.4: Panel **(a)**, mean value of the aspect ratio ε of the avalanches plotted as a function of the avalanche size. The dots correspond to an average over 100 avalanches and the error bars indicate the standard deviation. The panel **(b)** shows the probability density function of the threshold field $H_{\rm th}$ at which thermally driven avalanches develop. The red and black lines correspond to fittings obtained with Eqs. (5.1) and (5.2) respectively.

in the dynamically driven regime, the shape of the vortex influx is dominated by thermal diffusion ($D_{\rm t} \gg D_{\rm m}$) which is an isotropic process, thus giving rise to magnetic flux redistributions with $\varepsilon \gtrsim 1$. There is an inevitable asymmetry associated with the fact that vortex motion follows the direction of the magnetic flux gradient. In contrast to that, in the thermally driven regime where $D_{\rm m} \gg D_{\rm t}$, the shape of the avalanche is ruled by the magnetic diffusion which is highly directional (towards the center of the sample) and therefore elongated avalanches with $\varepsilon \gg 1$ are expected. These two extreme situations correspond well with the examples of flux reorganization shapes taken at either side of the minimum in the size distribution, as shown in the insets of Figure 5.3(a). At the transition point between the two regimes, $D_{\rm m} \sim D_{\rm t}$, which roughly corresponds to $\varepsilon = 2$ at low temperatures. In Figure 5.4(a), ε is plotted as a function of the size of the vortex reorganization. The dots correspond to an average over 100 avalanches and the error bars indicate the standard deviation. The dynamically driven regime is clearly identified by the region where $\varepsilon \sim 1$. It is important to point out that one must use caution when extrapolating the criteria used in this work to other superconductors. Disordered superconductors [100] and superconductors grown on inclined substrate [114] show clear asymetric penetration and $\varepsilon > 1$ can be associated with dynamical flux motion. The explanation provided here in terms of the diffusion constants D_m and D_t still stands. However in such samples, we must consider the existence of channels of increased vortex motion, breaking the isotropy of the superconducting material. It is the correlation of the $\varepsilon = 2$ criterion with the

beginning of the second peak in the size distribution that confirms the correctness of the criterion in this sample. Note that in highly disordered MgB_2 thin films, previous studies by Treiber *et al.* [100, 115] have proposed alternative criteria to distinguish dynamic flux reorganization from thermomagnetic avalanches based on the decompression of the magnetic flux lines.

Based on the $\varepsilon = 2$ criterion separating the two regimes, we can now rigorously estimate the threshold magnetic field $H_{\rm th}$ at which the first thermally driven avalanche is triggered. The result of this analysis for $T = 3.83$ K is shown in Figure 5.4(b). The alternative criterion corresponding to the local minimum of the size distribution provides very similar results. The obtained PDF shows a clear asymmetric shape.

To the best of our knowledge, there are no theoretical studies predicting the PDF of $H_{\rm th}$. Historically, the Weibull probability density function has been widely used to describe material or device failures [116]. This distribution is a weakest-link type distribution, meaning that the failure of the whole is dominated by the degradation rate of the weakest element (a nucleation point in our case). For instance, it properly describes dielectric breakdown, where the entire capacitor fails when a very localized region of the capacitor fails. The Weibull probability density function is defined by

$$P\left(H_{\rm th}\right) = \frac{\beta}{H_0}\left(\frac{H_{\rm th}-H_1}{H_0}\right)^{\beta-1} e^{-\left(\frac{H_{\rm th}-H_1}{H_0}\right)^{\beta}}, \tag{5.1}$$

where H_0 is referred to as the scale parameter, H_1 is the location parameter, and β is referred to as the shape parameter.

Alternatively, the Gumbel distribution, given by

$$P\left(H_{\rm th}\right) = \frac{1}{H_0}\exp\left[\frac{H_{\rm th}-H_1}{H_0} - e^{\frac{H_{\rm th}-H_1}{H_0}}\right], \tag{5.2}$$

has been shown to be useful in predicting the probability that an extreme earthquake, flood or other natural disaster will occur [117], as well as to describe the statistical distribution of phase slips in a long superconducting nanowire [118–120]. For the latter, the analogy is pertinent since the process of avalanche triggering starts from the contour of the sample, which can be regarded as a one dimensional nanowire.

An attempt to fit the experimentally determined probability density function with these two distributions is shown in Figure 5.4(b). The red (black) curve corresponds to Eq. (5.1) [Eq. (5.2)] with the following parameters: $\beta = 2$, $H_0 = 1.2$ Oe and $H_1 = 16.7$ Oe ($H_0 = 0.5$ Oe and $H_1 = 17.8$ Oe). Although both Gumbel and Weibull distributions seem to properly account for the PDF of the first magnetic flux avalanche at low temperatures, we will show in the next section that a more complex probability distribution emerges at higher temperatures.

Note that the criterion based on ε should be temperature dependent. Indeed, as mentioned above, a typical dynamically driven avalanche does not exceed the flux

front separating the critical state profile from the Meissner region. However, the distance between the sample border and the flux front increases with temperature. Therefore, it is expected that the value of ε separating dynamically from thermally driven avalanches also rises as temperature increases. It is important to point out that the observed dynamically and thermally driven avalanches may be influenced by the size of the sample, as reported in MgB_2 films [121]. In addition, it is also expected that the threshold field for triggering flux avalanches decreases with increasing the field ramp rate [122]. However, previous studies by Nowak *et al.* [104] showed that the avalanche activity in Nb rings remains unaffected for rates ranging over four decades from 0.2 µT/s to 2 mT/s. Recent numerical simulation predicts that the nature of the magnetic flux reorganization is only weakly dependent of the ramping rate [90]. In the present experiments, a maximum field ramp rate of about 20 mT/s has been used.

5.3.4 Spatial distribution of thermomagnetic flux avalanches

Previous investigation in MgB_2 films repeating three runs under the same external conditions, suggested that dendrites tend to nucleate from fixed locations along the edge [123]. By identifying the loci of the avalanches triggered at each point of the distribution, we conclude that the multiplicity of these nucleation spots are the main cause of the broadening of the distribution.

The finite width of the distribution of the threshold field H_{th} at which avalanches are triggered (Figure 5.4 (b)) originates from the distribution of nucleation points along the sample border. This is clearly illustrated in Figure 5.5 showing the number of avalanches detected along that border in 1 px = 1.48 μm wide intervals. Notice that the activity is higher at the center of the sample and diminishes towards the corners as a consequence of the fact that avalanches are only triggered if the Bean profile exceeds a characteristic length [54].

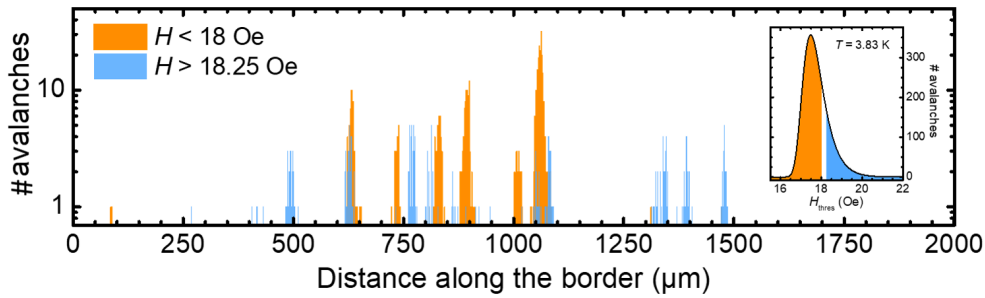

Figure 5.5: Spatial distribution of the first flux avalanches triggered along the bottom edge of the sample at $T = 3.83$ K. The data in orange corresponds to avalanches appearing at a field $H < 18$ Oe, while the blue bars correspond to those triggered at $H > 18.25$ Oe.

Interestingly, by plotting in orange the avalanches triggered at $H_{\mathrm{th}} < 18$ Oe

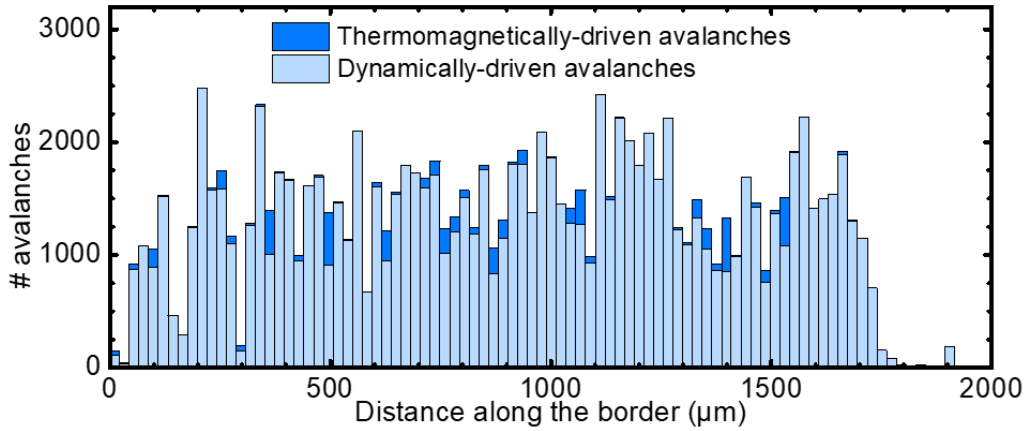

Figure 5.6: Spatial distribution of dynamically driven (in light blue) and thermomagnetically driven (in dark blue) flux avalanches along the bottom edge of the sample at $T = 3.83$ K.

and in blue those appearing for $H_{\text{th}} > 18.25$ Oe, we can see that nucleation points with low threshold fields do not overlap much with those having high threshold fields. It is tempting to associate these spatial distribution of avalanches to a spatial distribution of border defects. As we will demonstrate, this interpretation might be misleading since thermomagnetic avalanches tend to avoid border defects.

Prior to 2016, it was widely asummed that thermomagnetic flux avalanches should preferably nucleate at the location of defects, due to the large electric fields and the vortex traffic found at those points [22, 124, 125]. However, it has been recently experimentally shown that defects can actually have the opposite effect, i.e. thermomagnetic avalanches will be less likely to occur in their vicinity [20]. A possible argument is that defects act as flux faucets and favour dynamically driven flux penetration, thus releasing the magnetic flux pressure accumulated at the sample border. Recently, Jiang *et al.* [90] showed that the situation was a bit more complex and that the role of defects changes from nucleation points to inhibiting points for TMI according to the sweeping rate of the magnetic field $\dot{H}$.

In order to dig further on this issue, we have analyzed the spatial correlation between dynamically driven and thermomagnetically driven avalanches. Figure 5.6 shows the spatial distributions of dynamically driven (light blue) and thermomagnetically driven (dark blue) flux avalanches triggered at the bottom edge of the Nb superconducting film at $T = 3.83$ K. Note that unlike in Figure 5.5, here all thermomagnetically driven avalanches are included. A close inspection to Figure 5.6 indicates that thermomagnetic avalanches are mainly active where dynamically driven avalanches exhibit a minimum activity. This finding seems to corroborate previous reports [20] showing that dynamically driven and thermomagnetically driven avalanches are spatially anticorrelated.

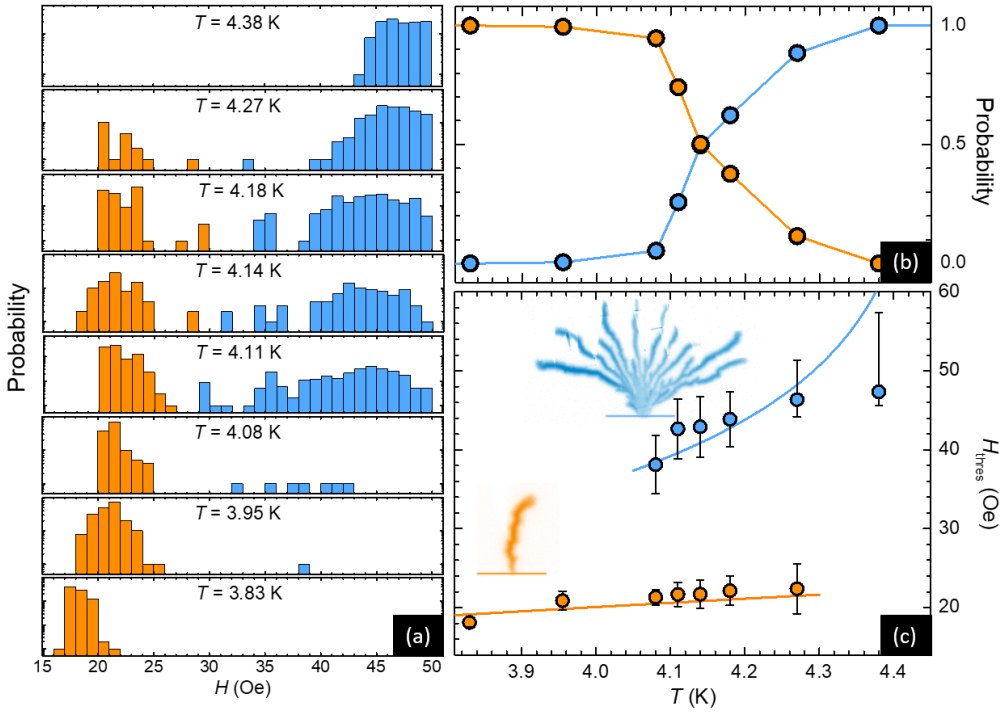

Figure 5.7: Threshold field for triggering thermally driven avalanches. **(a)** Probability density function of the threshold field H_{th} in semi-log scale for several temperatures T. The bimodal distribution exhibits a peak at low fields associated to the development of finger-like avalanches (in orange), and a broader peak at higher fields corresponding to dendritic avalanches (in blue). **(b)** Probability that the first avalanche is of filamentary type (orange dots) or branching type (blue dots) as a function of T. **(c)** $H-T$ diagram $H_{\mathrm{th}}(T)$ showing the measured and computed transition lines for the two different avalanche morphologies.

5.3.5 Threshold magnetic field of thermomagnetic breakdown

It has been reported that thermally driven avalanches can exhibit either a finger-like morphology at low temperatures or a branching structure at higher temperatures [126]. The question arises as to how this transition takes place and how sharp this crossover is. Figure 5.7(a) summarizes the resulting PDF of H_{th} for several temperatures in semi-log scale. The lowest temperature of 3.83 K is limited by the base temperature of our cryostat, whereas above 4.40 K, no avalanches were detected. The color code of the histogram indicates the morphology of the first thermally driven avalanche, with orange for the finger-like type and blue for the dendritic branching. At $T = 3.83$ K, 100% of the first avalanches detected are finger-like, whereas at $T = 4.38$ K, 100% of the first avalanches detected are of branching type. In between these two extrema, the PDF shows two well distinguished distributions. The amplitude of the peak corresponding to filamentary

avalanches progressively decreases whereas the peak associated to dendritic flux penetration becomes more dominant as temperature increases. This is more clearly seen in Figure 5.7(b) where the probability that the first avalanche is of one type or another is plotted as a function of temperature. A transition between these two regimes is observed close to $T = 4.15$ K. It has been argued, based on numerical simulations [127], that this transition may be associated to a change in the lateral heat diffusion. The sharpness of the observed transition is at odds with this interpretation since no abrupt change in the lateral heat diffusion is expected. The authors of Ref. [127] also showed that the morphology significantly depends on the initial background flux penetration depth prior to the triggering of the avalanche. This seems to be in agreement with our observation that dendritic avalanches take place at higher fields and correspondingly with a larger flux penetration depth than finger-like avalanches.

A $H-T$ diagram depicting the transition lines corresponding to the threshold magnetic field H_{th} at which the first thermally driven avalanches are triggered is shown in Figure 5.7(c). The lower (orange) dots indicate the transition to finger-like avalanches and the upper (blue) dots the transition to dendritic avalanches. The observed small variation of the threshold field at low temperatures is a general characteristic also reported in MgB_2 films [128] and tapes [129]. Closed-form expressions for the threshold magnetic field were recently derived for different regimes where the onset of avalanches is delayed either by heat diffusion through the superconducting sample, by the specific heat of superconductor or by heat evacuation through the substrate [21].

At low temperatures, the heat evacuation coefficients are sufficiently low and the system can be considered in an adiabatic regime where the instability is solely prevented by the specific heat of the superconductor. In this case the threshold field is given by [21]

$$H_{\mathrm{th},C} = \sqrt{\frac{2\,C_{\mathrm{Nb}}(T_{\mathrm{c}} - T)\,d}{\pi\,\mu_0\,w}}, \tag{5.3}$$

where d is the Nb film thickness, w the half width of the film and $C_{\mathrm{Nb}}(T) = C_{\mathrm{Nb},0}\,(T/T_{\mathrm{c}})^3$ the specific heat of the superconductor. Fitting the low field data points (in orange) with Eq. (5.3), we find $C_{\mathrm{Nb},0} = 5.5 \times 10^5$ J.K^{-1}.m^{-3}, which is comparable to typical values found in the literature [99], and observe a reasonable agreement between theoretical expression and experimental data.

At higher temperatures, the heat dissipation through the substrate becomes the delaying parameter and the transition line is given by

$$H_{\mathrm{th},h} = \frac{d\,j_{\mathrm{c}}}{\pi}\ \mathrm{atanh}\left(\frac{h\ (T_{\mathrm{c}} - T)}{n\,w\,d\,j_{\mathrm{c}}\,\mu_0\,\dot{H}_{\mathrm{a}}}\right), \tag{5.4}$$

where $\dot{H}_{\mathrm{a}}$ is the time derivative of the applied magnetic field during a step of the sweep, $j_{\mathrm{c}} = j_{\mathrm{c},0}(1 - T/T_{\mathrm{c}})$ is the critical current density, $h = h_0(T/T_{\mathrm{c}})^3$ is the coefficient of heat transfer between the superconductor and the substrate and n is the creep exponent. Using $\dot{H}_{\mathrm{a}} = 200$ Oe.s^{-1} and [99] $j_{\mathrm{c},0} = 1.5 \times 10^{11}$ A.m^2,

we find $h_0/n = 2.8 \times 10^{-1}$ W.K^{-1}.m^2 for the blue curve in Figure 5.7(c). Note that the last two experimental points underestimates the $H_{\rm th}$ value due to the set-up limitation to apply magnetic fields higher than 50 Oe. The clear mismatch between the experimental data and the theoretical expression can be explained by the large uncertainty in the parameters at play and by the fact that Eq.(5.4) assumes that the local temperature remains close to the bath temperature, which has been shown to be a strong hyphothesis [130]. In that sense, the solid line corresponding to $H_{{\rm th},h}$ should be taken with caution and interpreted as a general trend expected from the model. Both Eqs. (5.3) and (5.4), take into account the demagnetization factor. From the measured $H_{\rm th}$, it is possible to roughly estimate the local field as $H_{\rm local} \sim (w/t)^{1/2} H_{\rm th}$, where w is the half width of the sample and t its thickness. Since the geometrical prefactor is a large figure (~ 70), there is a substantial difference between $H_{\rm local}$ and $H_{\rm th}$. However, nearly the same geometrical factor applies for every datapoint, and therefore the trend observed in Figure 5.7 remains the same irrespective of plotting the data against $H_{\rm local}$ or $H_{\rm th}$.

We should emphasize that the two transition lines $H_{\rm th}$ seem to end at a precise point, a feature that has not been anticipated by the theoretical investigations. Nevertheless, their reasonable agreement with the measured $H_{{\rm th},C}$ and $H_{{\rm th},h}$ suggests that the observed abrupt transition between the two morphology regimes arises from a change in the mechanism of heat dissipation. Further systematic experimental investigation in other superconducting materials and substrates will certainly help to corroborate this finding.

5.4 Conclusion and further studies

To summarize, we provide a clear quantitative criterion based on magneto-optical imaging for distinguishing dynamically driven flux reorganization from those originating from thermomagnetic instabilities without the need of thermography or time resolved measurements. This technique permits to surpass previous studies based on Hall probe arrays and global magnetization measurements which conceal information about different nucleation spots in the sample, size and shape of individual avalanches. Based on the proposed quantitative criterion, we are able to determine the probability density function of the threshold field of thermomagnetic breakdown, track its temperature dependence with unprecedented resolution and unveil the details of the transition from filamentary to dendritic branching avalanches. The reasonable agreement of the two measured $H_{\rm th}(T)$ transition lines with the recently developed theoretical model suggests that a change of damping mechanism from in-plane heat diffusion to heat transfer to the substrate is at the origin of the observed two regimes. For low temperature TMI, geometric changes of w and d could corroborate this expression. Comparison with other superconductors in hope of changing the specific heat of the superconductor would be harder. While no new regime is expected for lower temperature, continous flow cryostats

can extend the range of temperature down to 2 K. The data points for $H_{\rm th}(T)$ at high temperature on the other hand could hardly be expanded further as the magnetic field needed diverges close to 4.4 K. However, the theoretical expression of this threshold is dependent on the magnetic field sweep rate. Further experiments varying this rate parameter could shed light on the robustness of this expression. Measurements at $T > T^*$ would also bring information on dynamical flux reorganization and the temperature dependence of the creep exponent. Finally, the studied system is non-destructive, which makes it to stand out from previous investigations of the triggering statistics of avalanche type events. This, in turn, allowed us to unequivocally assess the probability density function without being affected by the inevitable dispersion associated with an ensemble of replicas. Thanks to the spatial resolution of the MOI technique used, we were able to associate the natural spread of the magnetic threshold to different points of nucleation inside the sample.

Chapter 6

Conclusion and further prospects

Vortex physics plays a central role in the behaviour of type-II superconductors. Be it for applied purposes such as lossless current transport where vortex motion determines the critical current density of the superconductor or as a toy-model to study interacting multi-particle systems in a complex potential landscape, they remain fascinating physical entities. In the present manuscript, we focused on the dynamics of magnetic flux reorganization resulting from the continuous nucleation of new vortices at the sample's border as the external magnetic field is progressively increased.

As for any many-particle systems in physics, the task to describe the behaviour of each individual component quickly grows in complexity with the number of particles and degrees of freedom. Average macroscopic models called critical state models [35, 36] are used to describe the group behaviour of vortices in a strong pinning landscape at expenses of losing information of the composing single elements. A somewhat refined approach is the numerical resolution of Maxwell's equations to which a highly non-linear $\boldsymbol{E}(\boldsymbol{j})$ constitutive relation is added, bringing up further details to the average picture predicted by critical state models. Both models describe dynamically driven vortex reorganization characterized by a smooth evolution of the magnetic landscape with a negligible local temperature elevation. This description is however incomplete and unable to capture some of the experimental finding reported recently.

Notably, Brisbois *et al.* [20] showed significant discrepancy between the landscape obtained by simulation of thin superconducting Nb films with defined edge indentations and their experimental counterparts. A plausible cause of mismatch between simulations and experiments is the existence of important surface barriers in Nb. These surface barriers delay the vortex penetration up to a field H_p situated between the first critical field H_{c1} and the superheating field H_{sh}. Due to bulk pinning in hard superconductor, the fingerprints of surface barriers are often difficult to notice in magnetization measurements [96]. The change in the pattern formed by the discontinuity lines of thin films upon the presence of surface barriers constitute a unique tool to unveil their presence. This was further

confirmed in Chapter 4 where we studied thin indented YBCO films with lithographically defined edge indentations. YBCO is an ideal candidate because of its strong preference for dynamically driven magnetic flux penetration as well as for its high inclination to twinning defects, acting as suppressor of surface barriers [97]. The experimental magnetic landscape of the samples was observed via magneto-optical imaging, providing us with a 2D map of the magnetic field above the films. The comparison with theoretical predictions were done by looking at d-lines, regions of lower magnetic field in the sample caused by the sharp bending of the screening current lines. A numerical detection of the experimental d-lines lead us to conclude that contrary to the Nb case, the observed d-line network is in good agreement with Bean's critical state model predictions for a variety of edge indentation shapes in a wide range of temperatures.

Dynamically driven flux reorganization is part of the family of phenomena exhibiting self-organized criticality such as granular media avalanches or snow avalanches. The characteristic power-law distribution of event's sizes was made evident in Chapter 5 when looking at magnetic flux penetration in a rectangular Nb sample. Opposed to the predictable patterns of this phenomenon, thermally driven magnetic flux penetration occurs at low temperatures. The interplay of both reorganization mechanisms is rather complex. While it has been asserted that prior dynamical flux penetration was necessary to thermal flux penetration, questions concerning the nucleation of the latter remain open. An important one is the nature of the nucleation sites for thermal phenomenon. Theoretical arguments predicted a spatial correlation between dynamical and thermal reorganizations [21]. However, recent experiments found an inhibition of thermal events in sample with artificially introduced border defects which had the effect of locally increasing dynamical flux penetration. Using a large number of MOI data, we showed in Section 5.3.4 that regions of high dynamical vortex activity were actually anti-correlated with regions of high thermal vortex activity. This finding extends the experimental confirmation of their antagonistic character from the artificial indentations in [20] to the much smaller naturally occurring defects and nucleation points of a straight edge sample. These loci of high dynamical reorganizations tend to act as siphons of magnetic flux, relieving the local magnetic pressure necessary for the instabilities to occur thereby inhibiting them.

While an unpredictable pattern of the magnetic flux penetration result from thermally driven flux reorganization, they can be outlined by global properties such as its triggering magnetic field and its temperature dependency. However, the diversity of shapes observed makes it apparent that an interplay of many competing mechanisms are at stake. It is well know that thermally driven flux penetration changes its characteristic shape as the temperature of the sample is varied. At low temperature, they adopt filamentary forms without branching. At higher temperature, in addition to their increased size, their morphology evolves towards a more branched configuration reminiscent of fractal Lichtenberg figures [131]. Repeated observations of these two patterns at different temperatures revealed that they can be associated with two distinct populations of events coexisting at

intermediate temperature. An unexpected experimental finding we report in this thesis is that even in the coexisting region, two well-defined and distinct magnetic thresholds exist for them.

The existence of a gap between the thresholds of the two populations hints at a complex interaction of the different delaying mechanisms. An important ingredient is heat evacuation through the substrate. We limited our investigation to Nb on Si/SiO_2 substrates and it would be interesting to extend this research to study substrates with higher thermal conductivity such as sapphire. Still, it is necessary to ensure the good adhesion of the superconducting layer to other potential substrates in order to minimize the thermal contact resistance and thereby the influence of this interface. In addition, changing the substrate heat conductivity could allow the use of nanoheaters not only as resetting device but as local heat sources to investigate the stability of the magnetic landscape to heat perturbations. To distinguish further the influence of the specific heat of the superconductor and of the dissipation through the substrate, the experiment should be done with films of different thickness, as the respective thresholds have an inverse relationship regarding this parameter. Changing the sweeping rate of the magnetic field would also provide insight on vortex reorganization in two ways. First, of the three theoretical predictions proposed by [21], the threshold deduced when the heat transfer to the substrate is the dominating mechanism, which correspond the best to the branching avalanches observed at high temperature, is the only one dependent on this rate. This would allow for a clear confirmation or rejection of the pertinence of this expression. Second, increasing the sweeping rate should reduce the effectiveness of natural defects to act as siphons and therefore change the correlation relation between dynamical and thermal flux reorganization.

Finally, it is interesting to note the parallel between thermally driven flux penetration and general breakdown mechanism such as dielectric breakdown in a capacitor. Our superconducting sample provided the ideal experimental realisation to investigate the natural distribution of the breakdown threshold as a virtually infinite number of measurements can be taken on a single sample. We showed that the natural spread of the threshold is related to the multiple nucleation points present in each sample. Taking this parallel from a mere resemblance to a formal correspondence would bring in tools from the well studied problem in engineering of lifetime of a device. The typical goal of a ramp-to-failure test is the extrapolation of the device lifetime under normal load. The equivalent test of lifetime of a superconductor free of thermally driven penetration right under the triggering magnetic threshold would add to the traditional picture where only the dynamical rearrangement is considered between two increases of the magnetic field.

In short, the added scientific value of the presented work is twofold. In first place, we provide compelling evidence that surface barriers influence the network of discontinuity lines emerging from border defects. In second place, we provide the first clear-cut statistical criteria discriminating athermal and thermally driven magnetic flux avalanches. The latter proposes a whole new approach to experimentally determine the regions of the temperature-field phase diagram where

thermomagnetic instabilities develop, thus offering the possibility to test, validate and refine the available theoretical models. The highly time-consuming downside of the statistical analysis is somewhat compensated by the non-destructive nature of magnetic flux avalanches. Moreover, the methods and findings here advanced might transcend the domain of superconducting avalanches to foster application in apparently dissimilar systems such as dielectric breakdown and filamentary formation in metal-insulator transitions.

Appendices

Appendix A

Illustration of kernel convolution on images

We illustrate here the process of image convolution by kernels such as the one used for the domain correction algorithm presented in the section 3.2.4 as well as a brief explanation for the particular value of Sobel's filter.

A.1 Image convolution

The convolution of an image I by a kernel K to give an image I' is illustrated in Figure A.1. To compute $I'(x, y)$, one uses the elements of K as weights to be applied to the pixel at position (x, y) and its surroundings. Specifically, the intesity of the pixel $I'(x, y)$ is computed using the formula:

$$\begin{aligned} I'(4,3) = & a \cdot I(x-1, y-1) + b \cdot I(x-1, y) + c \cdot I(x-1, y+1) \\ & + d \cdot I(x, y-1) + e \cdot I(x, y) + f \cdot I(x, y+1) \\ & + g \cdot I(x+1, y-1) + h \cdot I(x+1, y) + i \cdot I(x+1, y+1), \end{aligned}$$

where the coefficients $a, ..., i$ are the 9 elements of the example kernel K. To compute pixel values for pixels at the border of the image using our kernel of size 3×3, we pad the image with pixels of zero intensity. The pixels of this region are often unreliable and discarded for future treatment.

A.2 Sobel filter

The simplest way to obtain the gradient of our picture along the x axis would be to replace each pixel's value by its central difference:

$$I(x, y) \to I'(x, y) = I(x-1, y) - I(x+1, y). \tag{A.1}$$

Since this numerical differentiation of the signal only probes two points, it is quite sensitive to noise. A solution to minimize the noise was proposed by I. Sobel in 1968 [132] by multiplying the derivative kernel by a 1-D Gaussian vector

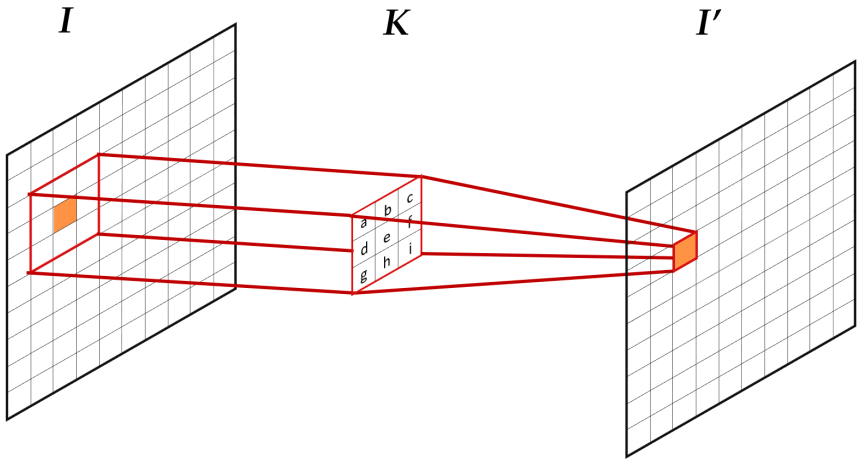

Figure A.1: Example of the creation of an image I' based on an original image I and a kernel K. The highlighted orange pixel shows the pixel computed in I' and its corresponding in I. The red square on I shows the pixels involved in this computation.

$$\begin{pmatrix} 0.125 \\ 0.250 \\ 0.125 \end{pmatrix} \begin{pmatrix} 1 & 0 & -1 \end{pmatrix} = \begin{pmatrix} 0.125 & 0 & -0.125 \\ 0.250 & 0 & -0.250 \\ 0.125 & 0 & -0.125 \end{pmatrix} \equiv G_x, \tag{A.2}$$

thereby probing six points to deduce the derivative along the x axis. The derivative with respect to the vertical direction follows the same process.

Publications

Direct Visualization of Current-Stimulated Oxygen Migration in $YBa_2Cu_3O_{7-\delta}$ Thin Films
S. Marinković, A. Fernandez-Rodriguez, S. Collienne, S. Blanco Alvarez, S. Melinte, B. Maiorov, G. Rius, X. Granados, N. Mestres, A. Palau, and A. V. Silhanek
ACS Nano **14**, 11765-11774 (2020).

In situ Magnetic Measurements of Ionic-Liquid-Gated Superconducting Films
Mingyang Qin, Ruozhou Zhang, Zefeng Lin, Zhongpei Feng, Xinjian Wei, Sylvain Blanco Alvarez, Chao Dong, Alejandro V. Silhanek, Beiyi Zhu, Jie Yuan, Qing Qin, Kui Jin.
Journal of Superconductivity and Novel Magnetism **33**, 159 (2020).

Magnetic Recording of Superconducting States
G. Shaw*, S. Blanco Alvarez*, J. Brisbois*, L. Burger, L. B. L. G. Pinheiro, R. B. G. Kramer, M. Motta, K. Fleury-Frenette, W. A. Ortiz, B. Vanderheyden and A. V. Silhanek.
Metals **9**, 1022 (2019).
* *These authors contributed equally to this work*

Statistics of thermomagnetic breakdown in Nb superconducting films
S. Blanco Alvarez, J. Brisbois, S. Melinte, R. B. G. Kramer and A.V. Silhanek.
Scientific Reports **9**, 3659 (2019).

Quantitative magneto-optical investigation of superconductor / ferromagnet hybrid structures
G. Shaw, J. Brisbois, L. B. G. L. Pinheiro, J. Müller, S. Blanco Alvarez, T. Devillers, N. M. Dempsey, J. E. Scheerder, J. Van de Vondel, S. Melinte, P. Vanderbemden, M. Motta, W. A. Ortiz, K. Hasselbach, R. B. G. Kramer, and A. V. Silhanek.
Review of Scientific Instruments **89**, 023705 (2018).

Statistics of localized phase slips in tunable width planar point contacts
X. D. A. Baumans, V. S. Zharinov, E. Raymenants, S. Blanco Alvarez, J. E. Scheerder, J. Brisbois, D. Massarotti, R. Caruso, F. Tafuri, E. Janssens, V. V. Moshchalkov, J. Van de Vondel and A. V. Silhanek.
Scientific Reports **7**, 44569 (2017).

Bibliography

[1] H. K. Onnes. Working notes. *Koninklijke Akademie van wetenschappen te Amsterdam*, 1911.

[2] W. Meissner and R. Ochsenfeld. Ien neuer effekt bei eintritt der supraleitfähigkeit. *Naturwissenschaften*, 21:787–788, 1933.

[3] F. London and H. London. The electromagnetic equations of the supraconductor. *Proceedings of the Royal Society A: Mathematical, Physical and Engineering Sciences*, 149, 1935.

[4] V. L. Ginzburg and L. D. Landau. On the theory of superconductivity. *J. Exp. Theor. Phys.*, 20:1064–1082, 1950.

[5] J. Bardeen, L. N. Cooper, and J. R. Schrieffer. Theory of superconductivity. *Phys. Rev.*, 108:1175–1204, 1957.

[6] J. G. Bednoz and K. A. Müller. Possible high T_c superconductivity in the Ba-La-Cu-O system. *Zeitschrift für Physik B Condensed Matter*, 64:189–193, 1986.

[7] Y. Kamihara, T. Watanabe, M. Hirano, and H. Hosono. Iron-based layered superconductor La[$O_{1-x}F_x$]FeAs (x=0.05-0.12) with T_c = 26 K. *Journal of American Chemical Society*, 130:3296–3297, 2008.

[8] K. Andres, J. E. Graebner, and H. R. Ott. $4f$-virtual-bound-state formation in $CeAl_3$ at low temperatures. *Phys. Rev. Lett.*, 35:1779–1782, 1975.

[9] H. Oike, M. Kamitani, Y. Tokura, and F. Kagawa. Kinetic approach to superconductivity hidden behind a competing order. *Sci. Adv.*, 4, 2018.

[10] A. A. Shanenko, M. D. Croitoru, M. Zgirski, F. M. Peeters, and K. Arutyunov. Size-dependent enhancement of superconductivity in Al and Sn nanowires: Shape-resonance effect. *Phys. Rev. B*, 74:052502, 2006.

[11] K. Y. Arutyunov, E. A. Sedov, I.A. Golokolenov, V. V. Zav'yalov, G. Konstantinidis, A. Stavrinidis, G. Stravinidis, I. Vasiliadis, T. Kekhagias, G. P. Diitrakopulos, F. Komninu, M. D. Kroitoru, and A. A. Shanenko. Quantum

size effect in superconducting aluminum films. *Physics of the Solid State*, 61:0559–1562, 2019.

[12] K. Ueno, S. Nakamura, H. Shimotani, A. Ohtomo, N. Kimura, T. Nokima, H. Aoki, Y. Iwasa, and M. Kawasaki. Electric-field-induced superconductivity in an insulator. *Nature Materials*, 7:855–858, 2008.

[13] M. Qin, R. Zhang, Z. Lin, Z. Feng, X. Wei, S. Blanco Alvarez, C. Dong, A. V. Silhanek, B. Zhu, J. Yuan, Q. Qin, and K. Jin. In situ magnetic measurements of ionic-liquid-gated superconducting films. *J. Supercond. Nov. Magn.*, 33:159–163, 2020.

[14] U. Schoop, M. W. Rupich, C. Thieme, D. T. Verebelyi, W. Zhang, X. Li, T. Kodenkandath, N. Nguyen, E. Siegal, L. Civale, T. Holesinger, B. Maiorov, A. Goyal, and M. Paranthaman. Second generation HTS wire based on RABiTS substrates and MOD YBCO. *IEEE Transactions on Applied Superconductivity*, 15:2611–2616, 2005.

[15] T. Tan, M. A. Wolak, X. X. Xi, T. Tajima, and L. Civale. Magnesium diboride coated bulk niobium: a new approach to higher acceleration gradient. *Sci. Rep.*, 6:35879, 2016.

[16] W. Zhang, L. You, H. Li, J. Huang, C. Lv, L. Zhang, X. Liu, J. Wu, Z. Wang, and X. Xie. NbN superconducting nanowire single photon detector with efficiency over 90% at 1550 nm wavelength operational at compact cryocooler temperature. *Science China Physics, Mechanics & Astronomy*, 60:120314, 2017.

[17] B. Korzh, Q-Y. Zhao, S. Frsca, J. P. Allmaras, T. M. Autry, E. A. Bersin, M. Colangelo, G. M. Crouch, A. E. Dane, T. Gerrits, F. Marsili, G. Moody, E. Ramirez, J. D. Rezac, M. J. Stevens, E. E. Wollman, D. Zhu, P. D. Hale, K. L. Silverman, R. P. Mirin, S. W. Nam, M. D. Shaw, and K. K. Berggren. Demonstration of sub-3 ps temporal resolution with a superconducting nanowire single-photon detector. *Nat. Photonics*, 2020.

[18] F. Arute, K. Arya, R. Babbush, D. Bacon, J.C. Bardin, R. Barends, R. Biswas, S. Boixo, F. G. S. L. Brandao, D. A. Buell, B. Burkett, Y. Chen, Z. Chen, B. Chiaro, R. Collins, W. Courtney, A. Dunsworth, E. Farhi, B. Foxen, A. Fowler, C. Gidney, M. Giustina, R. Graff, K. Guerin, S. Habegger, M. P. Harrigan, A. Hartmann, M. J. Ho, M. Hoffmann, T. Huang, T. S. Humble, S. V. Isakov, E. Jeffrey, Z. Jiang, D. Kafri, K. Kechedzhi, J. Kelly, P. V. Klimov, S. Knysh, A. Korotkov, F. Kostritsa, D. Landhuis, M. Lindmark, E. Lucero, D. Lyakh, S. Mandrà, J. R. McClean, M. McEwen, A. Megrant, X. Mi, K. Michielsen, M. Mohseni, J. Mutus, O. Naaman, M. Neeley, C. Neill, M. Y. Niu, E. Ostby, A. Petukhov, J. C. Platt, C. Quintana, E. G. Rieffel, P. Roushan, N. C. Rubin, D. Sank, K. J. Satzinger,

V. Smelyanskiy, K. J. Sung, M. D. Trevithick, A. Vainsencher, B. Villalonga, T. White, Z. J. Yao, P. Yeh, A. Zalcman, and H. Neven. Quantum supremacy using a programmable superconducting processor. *Nature*, 574:505–510, 2019.

[19] Z. L. Jelić. *Emergent vortex phenomena in spatially and temporally modulated superconducting condensates.* PhD thesis, University of Liège and University of Antwerp, 2018.

[20] J. Brisbois, O.-A. Adami, J. I. Avila, M. Motta, W. A. Ortiz, N. D. Nguyen, P. Vanderbemden, B. Vanderheyden, R. B. G. Kramer, and A. V. Silhanek. Magnetic flux penetration in Nb superconducting films with lithographically defined microindentations. *Phys. Rev. B*, 93:054521, 2016.

[21] J. I. Vestgården, Y. M. Galperin, and T. H. Johansen. Oscillatory regimes of the thermomagnetic instability in superconducting films. *Phys. Rev. B*, 93:174511, 2016.

[22] J. I. Vestgården, D. V. Shantsev, Y. M. Galperin, and T. H. Johansen. Flux penetration in a superconducting strip with an edge indentation. *Phys. Rev. B*, 76:174509, 2007.

[23] A. A. Abrikosov. *Dokl. Akad. Nauk SSSR*, 86:489, 1952.

[24] J. R. Clem. Simple model for the vortex core in a type II superconductor. *J. Low Temp. Phys.*, 18:427–434, 1975.

[25] P. Mangin and R. Kahn. *Supraconductivité.* EDP Sciences, 2013.

[26] K. H. Bennemann and J. B. Ketterson. *Superconductivity*, volume 1. Springer, 2008.

[27] J. Bardeen and M. J. Stephen. Theory of the motion of vortices in superconductors. *Physical Review*, 140:A1197, 1965.

[28] G. Blatter, M. V. Feigel'man, V. B. Geshkenbein, A. I. Larkin, and V. M. Vinokur. Vortices in high-temperature superconductors. *Reviews of Modern Physics*, 66:1125–1388, 1994.

[29] H. Suhl. Inertial mass of a moving fluxoid. *Phys. Rev. Lett.*, 14, 1965.

[30] D. Golubchik, E. Polturak, and G. Koren. Mass of a vortex in a superconducting film measured via magneto-optical imaging plus ultrafast heating and cooling. *Phys. Rev. B*, 85:060504, 2012.

[31] E. Zeldov, A. I. Larkin, V. B. Geshkenbein, M. Konczykowski, D. Majer, B. Khaykovich, V. M. Vinokur, and H. Shtrikman. Geometrical barriers in high-temperature superconductors. *Phys. Rev. Lett.*, 73:1428–1431, 1994.

[32] C. P. Bean and J. D. Livingston. Surface barrier in type-II superconductors. *Phys. Rev. Lett.*, 12:14–16, 1964.

[33] E. Altshuler and T. H. Johansen. Colloquium: Experiments in vortex avalanches. *Rev. Mod. Phys.*, 76:471–487, 2004.

[34] K. Behnia, C. Capan, D. Mailly, and B. Etienne. Internal avalanches in a pile of superconducting vortices. *Phys. Rev. B*, 61:3815, 2000.

[35] C. P. Bean. Magnetization of hard superconductors. *Phys. Rev. Lett.*, 8:250–253, 1962.

[36] Y. B. Kim, C. F. Hempstead, and A. R. Strnad. Critical persistent currents in hard superconductors. *Phys. Rev. Lett.*, 9:306, 1962.

[37] J.R. Clem and K.K. Berggren. Geometry-dependant critical currents in superconducting nanocircuits. *Phys. Rev. B*, 84:174510, 2011.

[38] E. H. Brandt and M. Indenbom. Type-II superconductor strip with current in a perpendicular magnetic field. *Phys. Rev. B*, 48, 1993.

[39] E. H. Brandt. Susceptibility of superconductor disks and rings with and without flux creep. *Phys. Rev. B*, 55:14513, 1997.

[40] C. M. Aegerter, M. S. Welling, and R. J. Wijngaarden. Self-organized criticality in the Bean state in $YBa_2Cu_3O_{7-x}$. *Europhys. Lett.*, 65:753–759, 2004.

[41] S. Field, J. Witt, and F. Nori. Superconducting vortex avalanches. *Phys. Rev. Lett.*, 74:1206–1209, 1995.

[42] C. M. Aegerter. Evidence for self-organized criticality in the Bean critical state in superconductors. *Phys. Rev. E*, 58:1438–1441, 1998.

[43] R. J. Wijngaarden, M. S. Welling, C. M. Aegerter, and M. Menghini. Avalanches and self-organized criticality in superconductors. *Eur. Phys. J. B*, 50:117–122, 2006.

[44] P. Leidered, J. Boneberg, P. Brüll, V. Bujok, and S. Herminghaus. Nucleation and growth of a flux instability in superconducting $YBa_2Cu_3O_{7-x}$ films. *Phys. Rev. Lett.*, 71:2646, 1993.

[45] U. Bolz, B. Biehler, D. Schmidt, B.-U. Runge, and P. Leidered. Dynamics of the dendritic flux instability in $YBa_2Cu_3O_{7-\delta}$ films. *Europhys. Lett.*, 64:517–523, 2003.

[46] Y.-H. Zhou, C. Wang, C. Liu, H. Yong, and X. Zhang. Optically triggered chaotic vortex avalanches in superconducting $YBa_2Cu_3O_{7-x}$ films. *Phys. Rev. Appl.*, 13:024036, 2020.

[47] J. Lombardo, Ž. L. Jelić, X. D. A. Baumans, J. E. Scheerder, J. P. Nacenta, V. V. Moshchalkov, J. Van de Vondel, R. B. G. Kramer, M. V. Milošević, and A. V. Silhanek. In situ tailoring of superconducting junctions via electro-annealing. *Nanoscale*, 10:1987–1996, 2018.

[48] S Marinković, A. Fernández-Rodríguez, S. Collienne, S. Blanco Alvarez, S. Melinte, B. Maiorov, G. Rius, X. Granados, N. Mestres, A. Palau, and A. V. Silhanek. Direct visualization of current-stimulated oxygen migration in $YBa_2Cu_3O_{7-\delta}$ thin films. *ACS Nano*, 14:11765–11774, 2020.

[49] X. D. A. Baumans, A. Fernández-Rodrígez, N. Mestres, S. Collienne, J. Van de Vondel, A. Palau, and A. V. Silhanek. Electromigration in the dissipative state of high temperature superconducting bridges. *Appl. Phys. Lett.*, 114:012601, 2019.

[50] M. Baziljevich, E. Baruch-El, T. H. Johansen, and Y. Yeshurun. Dendritic instability in $YBa_2Cu_3O_{7-\delta}$ films triggered by transient magnetic fields. *Appl. Phys. Lett.*, 105:012602, 2014.

[51] R. G. Mints and A. L. Rakhmano. Critical state stability in type-II superconductors and superconducting-normal-metal composites. *Rev. Mod. Phys*, 53:551–592, 1981.

[52] I. Aranson, A. Gurevich, and V. Vinokur. Vortex avalanches and magnetic flux fragmentation in superconductors. *Phys. Rev. Lett.*, 87:067003, 2001.

[53] A. L. Rakhmanov, Y. M. Shantsev, Y. M. Galperin, and T. H. Johansen. Finger patterns produced by thermomagnetic instability in superconductors. *Phys. Rev. B*, 70:224502, 2004.

[54] D. V. Denisov, A. L. Rakhmanov, D. V. Shantsev, Y. M. Galperin, and T. H. Johansen. Dendritic and uniform flux jumps in superconducting films. *Phys. Rev. B*, 73:014512, 2006.

[55] D. V. Denisov, D. V. Shantshev, Y. M. Galperin, E.-M. Choi, H.-S. Lee, S. I. Lee, A. V. Bobyl, P. E. Goa, A. A. G. Olsen, and T. H. Johansen. Onset of dendritic flux avalanches in superconducting films. *Phys. Rev. Lett.*, 97:077002, 2006.

[56] J. Pearl. Current distribution in superconducting films carrying quantized fluxoids. *Appl. Phys. Lett.*, 5:65–66, 1964.

[57] M. Fox. *Optical properties of solids.* Oxford University Press, 2^{nd} edition, 2012.

[58] J. M. D. Coey. *Magnetism and magnetic materials.* Cambridge University Press, 2012.

[59] ed. David R. Lide. *CRC Handbook of Chemistry and Physics.* CRC Press LLC, 2005.

[60] V.K. Vlasko-Vlasov, L.A. Dorosinskii, M.V. Indenbom, V. I. Nikitenko, Yu. A. Ossip'yan, and A.A. Polyanskii. Direct experimental study of magnetization processes in high-T_c superconducting materials. *Sov. J. Low. Temp. Phys.*, 17:762, 1991.

[61] L.A. Dorosinskii, M.V. Indenbom, V.I. Nikitenko, Yu. A. Ossip'yan, A.A. Polyanskii, and V.K. Vlasko-Vlasov. Studies of HTSC crystal magnetization features using indicator magneto-optic films with in-plane anisotropy. *Physica C*, 203:159–156, 1992.

[62] J. Brisbois. *Magneto-optical investigation of superconducting hybrid structures.* PhD thesis, University of Liège, 2017.

[63] M. R. Koblischka and R. J. Wijngaarden. Magneto-optical investigations of superconductors. *Supercond. Sci. Technol.*, 8:199, 1995.

[64] Ch. Jooss, J. Albrecht, H. Kuhn, S. Leonhard, and H. Kronmüller. Magneto-optical studies of current distributions in high-T_c superconductors. *Rep. Prog. Phys.*, 65:651–788, 2002.

[65] L. E. Helseth, R. W. Hansen, E.I. Il'yashenko, M. Baziljevich, and T.H. Johansen. Faraday rotation spectra of bismuth-substituted ferrite garnet films with in-plane magnetization. *Phys. Rev. B*, 64:174406, 2001.

[66] C. Liu, X. Zhang, and Y.-H. Zhou. A novel design for magneto-optical microscopy and its calibration. *Meas. Sci. Technol.*, 30:115904, 2019.

[67] M. Baziljevich, D. Barness, M. Sinvani, E. Perel, A. Shaulov, and Y. Yeshurun. Magneto-optical system for high speed real time imaging. *Rev. Sci. Instrum*, 83:083707, 2012.

[68] B.-U. Runge, U. Bolz, J. Eisenmenger, and P. Leiderer. Ultrafast magneto-optical study of flux avalanches in high-T_c superconductors. *Physica C*, 341-348:2029–2030, 2000.

[69] Y. Hashimoto, A. R. Khorsand, M. Savoini, B. Koene, D. Bossini, A. Tsukamoto, A. Itoh, Y. Ohtsuka, K. Aoshima, A.V. Kimel, A. Kirilyuj, and Th. Rasing. Ultrafast time-resolved magneto-optical imaging of all-optical switching in GdFeCo with femtosecond time-resolution and a µm spatial-resolution. *Rev. Sci. Instrum.*, 85:063702, 2014.

[70] A. Y. Elezzabi and M. R. Freeman. Ultrafast magneto-optic sampling of picosecond current pulses. *Appl. Phys. Lett.*, 68:3546, 1996.

[71] W. Romanishin. *An introduction to astronomical photometry using CCDs.* 2002.

[72] H. Karttunen, P. Kröger, H. Oja, M. Poutanen, and K.J. Donner. *Fundamental astronomy.* Springer International Publishing, 6^{th} edition, 2017.

[73] F. Laviano, D. Botta, A. Chiodoni, R. Gerbaldo, G. Ghigo, L. Gozzelino, S. Zannella, and E. Mezzeti. An improved method for quantitative magneto-optical analysis of superconductors. *Supercond. Sci. Technol.*, 16:71–79, 2002.

[74] M. Roussel. *Magneto-optical imaging in superconductors.* PhD thesis, University of Wollongong, 2007.

[75] W. C. Patterson, N. Garraud, E. E. Shorman, and D. P. Arnold. A magneto-optical microscope for quantitative measurement of magnetic microstructures. *Rev. Sci. Instrum.*, 86:094704, 2015.

[76] R. Grechishkin, M. Kustov, S. Ilyashenko, O. Gasanov, F. Dumas-Bouchiat, and N. M. Dempsey. Magneto-optical imaging and analysis of the magnetic field micro distributions with the aid of biased indicator films. *J. Appl. Phys*, 120:174502, 2016.

[77] F. S. Wells, A. V. Pan, S. Wilson, I. A. Golovchanskiy, S. A. Fedoseev, and A. Rozenfeld. Dynamic magneto-optical imaging of superconducting thin films. *Supercond. Sci. Technol.*, 29:035014, 2016.

[78] G. Shaw, J. Brisbois, L. B. G. L. Pinheiro, J. Müller, S. Blanco Alvarez, T. Devillers, N. M. Dempsey, J. E. Scheerder, J. Van de Vondel, S. Melinte, P. Vanderbemden, M. Motta, W. A. Ortiz, K. Hasselbach, R. B. G. Kramer, and A. V. Silhanek. Quantitative magneto-optical investigation of superconductor/ferromagnet hybrid structures. *Rev. Sci. Instrum.*, 89:023705, 2018.

[79] J. Yang, C. Liu, X. Zhang, and Y. Zhou. A novel method for quantitative magneto-optical measurement under non-uniform illumination. *Meas. Sci Technol.*, 31:085002, 2020.

[80] M. Gerken, S. Sievers, and H. W. Schumacher. Inhomogeneous field calibration of a magneto-optical indicator film device. *Meas. Sci. Technol.*, 31:075009, 2020.

[81] S. Geller and M. A. Gilleo. Structure and ferrimagnetism of yttrium and rare-earth-iron garnets. *Acta Cryst.*, 10:239, 1957.

[82] G. Shaw, S. Blanco Alvarez, J. Brisbois, L. Burger, L.B.L.G. Pinheiro, R.B.G. Kramer, M. Motta, K. Fleury-Frenette, W. A. Ortiz, B. Vanderheyden, and A. V. Silhanek. Magnetic recording of superconducting states. *Metals*, 9:1022, 2019.

[83] C. Tannous and R. L. Comstock. *Magnetic information-storage materials.* Springer International Publishing, 2017.

[84] V. Bujok, P. Brüll, J. Boneberg, S. Herminghaus, and P. Leidered. Nanosecond magneto-optic study of a new instability in thin $YBa_2Cu_3O_{7-x}$ films. *Appl. Phys. Lett.*, 63:412–414, 1993.

[85] E. Baruch-El, M. Baziljevich, T. H. Johansen, and Y. Yeshurun. Substrate influence on dendritic flux instability in YBCO thin films. *J. Supercond. Nov. Magn.*, 28:379–382, 2015.

[86] E. Baruch-El, M. Baziljevich, B. Ya. Shapiro, T. H. Johansen, A. Shaulov, and Y. Yeshurun. Dendritic flux instabilities in $YBa_2Cu_3O_{7-x}$ films : Effect of temperature and magnetic field ramp rate. *Phys. Rev. B*, 94:054509, 2016.

[87] E. Baruch-El, M. Baziljevich, T. H. Johansen, A. Shaulov, and Y. Yeshurun. Thickness dependence of dendritic flux avalanches in $YBa_2Cu_3O_{7-x}$ films. *J. Phys. : Conf. Ser.*, 969:012042, 2018.

[88] A. Gurevich and M. Friesen. Nonlinear transport current flow in superconductors with planar obstacles. *Phys. Rev. B*, 62:4004–4025, 2000.

[89] M. Friesen and A. Gurevich. Nonlinear current flow in superconductors with restricted geometries. *Phys. Rev. B*, 63:064521, 2001.

[90] L. Jiang, C. Xue, L. Burger, B. Vanderheyden, A. V. Silhanek, and Y.-H. Zhou. Selective triggering of magnetic flux avalanches by an edge indentation. *Phys. Rev. B*, 101:224505, 2020.

[91] L. Burger. Working notes. 2019.

[92] X. Obradors, T. Puig, A. Pomar, F. Sandiumenge, S. Piñol, N. Mestres, O. Castaño, M. Coll, A. Cavallaro, A. Palau, J. Gázquez, J. C. González, J. Gutiérrez, N. Romà, S. Ricart, J. M. Moretó, M. D. Rossell, and G. Van Tendeloo. Chemical solution deposition: A path towards low cost coated conductors. *Supercond. Sci. Technol.*, 17:1055–1064, 2004.

[93] X. Obradors, T. Puig, S. Ricart, M. Coll, J. Gazquez, A. Palau, and X. Granados. Growth, nanostructure and vortex pinning in superconducting $YBa_2Cu_3O_{7-\delta}$ thin films based on trifluoroacetate solutions. *Supercond. Sci. Technol.*, 25, 2012.

[94] C. A. Schneider, W. S. Rasband, and K. W. Eliceiri. *NIH Image to ImageJ: 25 years of image analysis*, 2012.

[95] P. Thévenaz, U. E. Ruttimann, and M. Unser. *A Pyramid Approach to Subpixel Registration Based on Intensity*, 1998.

[96] P. K. Mishra, G. Ravikumar, V. C. Sahni, M. R. Koblischka, and A. K. Grover. Surface pinning in niobium and a high-T_c superconductor. *Physica C*, 269:71–75, 1996.

[97] M. Konczykowski, L. I. Burlachkov, Y. Yeshurun, and F. Holtzberg. Evidence for surface barriers and their effect on irreversibility and lower-critical-field measurements in Y-Ba-Cu-O crystals. *Phys. Rev. B*, 43:13707–13710, 1991.

[98] G. P. Lousberg, M. Ausloos, Ph. Vanderbemden, and B. Vanderheyden. Bulk high-Tc superconductors with drilled holes: how to arrange the holes to maximize the trappedmagnetic flux ? *Supercond. Sci. Technol.*, 21:025010, 2008.

[99] M. Motta, F. Colauto, J. I. Vestgården, J. Fritzsche, M. Timmermans, J. Cuppens, C. Attanasio, C. Cirillo, V. V. Moshchalkov, J. Van de Vondel, T. H. Johansen, W. A. Ortiz, and A. V. Silhanek. Controllable morphology of flux avalanches in microstructured superconductors. *Phys. Rev. B*, 89:134508, 2014.

[100] S. Treiber, C. Stahl, G. Schütz, and J. Albrecht. Unusual flux jumps above 12 K in non-homogeneous MgB_2 thin films. *Supercond. Sci. Technol.*, 25:065010, 2012.

[101] Ze Jing, Huadong Yong, and Youhe Zhou. Influences of non-uniformities and anisotropies on the flux avalanche behaviors of type-II superconducting films. *Supercond. Sci. Technol.*, 29:105001, 2016.

[102] M.R. Wertheimer and J. le G. Gilchrist. Flux jumps in type II superconductors. *J. Phys. Chem. Solids*, 28:2509 – 2524, 1967.

[103] C. A. Durán, P. L. Gammel, R. E. Miller, and D. J. Bishop. Observation of magnetic-field penetration via dendritic growth in superconducting niobium films. *Phys. Rev. B*, 52, 1995.

[104] E. R. Nowak, O. W. Taylor, Li Liu, H. M. Jaeger, and T. I. Selinder. Magnetic flux instabilities in superconducting niobium rings: Tuning the avalanche behavior. *Phys. Rev. B*, 55:11702–11705, 1997.

[105] M. Motta, F. Colauto, W. A. Ortiz, J. Fritzsche, J. Cuppens, W. Gillijns, V. V. Moshchalkov, T. H. Johansen, A. Sanchez, and A. V. Silhanek. Enhanced pinning in superconducting thin films with graded pinning landscapes. *Appl. Phys. Lett.*, 102:212601, 2013.

[106] Jérémy Brisbois, Maycon Motta, Jonathan I. Avila, Gorky Shaw, Thibaut Devillers, Nora M. Dempsey, Savita K. P. Veerapandian, Pierre Colson, Benoît Vanderheyden, Philippe Vanderbemden, Wilson A. Ortiz, Ngoc Duy Nguyen, Roman B. G. Kramer, and Alejandro V. Silhanek. Imprinting superconducting vortex footsteps in a magnetic layer. *Sci. Rep.*, 6:27159 EP –, 2016.

[107] P. Flubacher, A. J. Leadbetter, and J. A. Morrison. The heat capacity of pure silicon and germanium and properties of their vibrational frequency spectra. *The Philosophical Magazine: A Journal of Theoretical Experimental and Applied Physics*, 4:273–294, 1959.

[108] C. J. Glassbrenner and Glen A. Slack. Thermal conductivity of silicon and germanium from 3°K to the melting point. *Phys. Rev.*, 134:A1058–A1069, 1964.

[109] F. Colauto, E.M. Choi, J. Y. Lee, S. I. Lee, V. V. Yurchenko, T. H. Johansen, and W. A. Ortiz. Mapping flux avalanches in MgB_2 films—equivalence between magneto-optical imaging and magnetic measurements. *Supercond. Sci. Technol.*, 20:L48, 2007.

[110] A. A. Babaei-Brojeni, Y. Mwatari, M. Benkraouda, and Clem J. R. Magnetic fields and currents for two current-arryig parallel coplanar superconducting strips in a perpendicular magnetic field. *Supercond. Sci, Technol.*, 15:1454, 2002.

[111] J. R. Clem and A. Sanchez. Hysteretic ac losses and susceptibility of thin superconducting disks. *Phys. Rev. B*, 50:9355, 1994.

[112] Z. L. Xiao, E. Y. Andrei, P. Shuk, and M. Greenblatt. Joule heating induced by vortex motion in a type-II superconductor. *Phys. Rev. B*, 64:094511, 2001.

[113] E. Altshuler, T. H. Johansen, Y. Paltiel, Peng Jin, K. E. Bassler, O. Ramos, Q. Y. Chen, G. F. Reiter, E. Zeldov, and C. W. Chu. Vortex avalanches with robust statistics observed in superconducting niobium. *Phys. Rev. B*, 70:140505, 2004.

[114] A. J. Qviller, V. V. Yurchenko, Y. M. Galperin, J. I. Vestgården, P. B. Mozhaev, J. B. Handsen, and T. H. Johansen. Quasi-one-dimensional intermittent flux behavior in superconducting films. *Phys. Rev. X*, 2:011007, 2012.

[115] S. Treiber, C. Stahl, G. Schütz, and J. Albrecht. Stability of the current-carrying state in nonhomogeneous MgB_2 films. *Phys. Rev. B*, 84:094533, 2011.

[116] J. W. McPherson. *Reliability Physics and Engineering*. Springer, New York, 2010.

[117] E. J. Gumbel. Statistical theory of extreme values and some practical applications. Technical report, National Bureau of Standards, Washington D. C., Applied mathematics Div., 1954. Applied mathematics series.

[118] Xavier D. A. Baumans, Joseph Lombardo, Jérémy Brisbois, Gorky Shaw, Vyacheslav S. Zharinov, Ge He, Heshan Yu, Jie Yuan, Beiyi Zhu, Kui Jin,

Roman B. G. Kramer, Joris Van de Vondel, and Alejandro V. Silhanek. Healing effect of controlled anti-electromigration on conventional and high-tc superconducting nanowires. *Small*, 13:1700384, 2017.

[119] Peng Li, Phillip M. Wu, Yuriy Bomze, Ivan V. Borzenets, Gleb Finkelstein, and A. M. Chang. Switching currents limited by single phase slips in one-dimensional superconducting Al nanowires. *Phys. Rev. Lett.*, 107:137004, 2011.

[120] T. Aref, A. Levchenko, V. Vakaryuk, and A. Bezryadin. Quantitative analysis of quantum phase slips in superconducting $Mo_{76}Ge_{24}$ nanowires revealed by switching-current statistics. *Phys. Rev. B*, 86:024507, 2012.

[121] Jae-Yeap Lee, Eun-Mi Choi, Hyun-Sook Lee, Hu-Jong Lee, Sung-Ik Lee, Å. A. F. Olsen, D.V. Shantsev, and T.H. Johansen. Microscopic flux density of small and dendritic flux jumps in MgB_2 thin films. *Supercond. Sci. Technol.*, 21:105021, 2008.

[122] R. G. Mints and E. H. Brandt. Flux jumping in thin films. *Phys. Rev. B*, 54:12421–12426, Nov 1996.

[123] T.H. Johansen, D.V. Shantev, Å.A.F. Olsen, M. Roussel, A.V. Pan, and S.X. Dou. Reproducible nucleation sites for flux dendrites in MgB_2. *Surface Science*, 601:5712 – 5714, 2007. Wagga Symposium on Surfaces and Interfaces - 2006.

[124] Th. Schuster, M. V. Indenbom, M. R. Koblischka, H. Kuhn, and H. Kronmüller. Observation of current-discontinuity lines in type-II superconductors. *Phys. Rev. B*, 49:3443, 1994.

[125] Th. Schuster, H. Kuhn, and E. H. Brandt. Flux penetration into flat superconductors of arbitrary shape: Patterns of magnetic and electric fields and current. *Phys. Rev. B*, 54:3514, 1996.

[126] Johansen, T. H., Baziljevich, M., Shantsev, D. V., Goa, P. E., Y. M. Galperin, Kang, W. N., Kim, H. J., Choi, E. M., Kim, M.-S., and Lee, S. I. Dendritic magnetic instability in superconducting MgB_2 films. *Europhys. Lett.*, 59:599–605, 2002.

[127] J. I. Vestgården, D. V. Shantsev, Y. M. Galperin, and T. H. Johansen. The diversity of flux avalanche patterns in superconducting films. *Supercond. Sci. Technol.*, 26:055012, 2013.

[128] E. Baruch-El, M. Baziljevich, T.H. Johansen, J. Albrecht, A. Shaulov, and Y. Yeshurun. Dendritic flux instability in MgB_2 films above liquid hydrogen temperature. *Supercond. Sci. Technol.*, 31:025005, 2018.

[129] T. Qureishy, C. Laliena, E. Martinez, A. J. Qviller, J. I. Vestgården, T.H. Johansen, R. Navarro, and P. Mikheenko. Dendritic flux avalanches in a superconducting MgB_2 tape. *Supercond. Sci. Technol.*, 30:125005, 2017.

[130] J. I. Vestgården, D. V. Shantsev, Y. M. Galperin, and T. H. Johansen. Lightning in superconductors. *Scientific Reports*, 2:886 EP –, 2012. Article.

[131] I. A. Rudnev, D. V. Shantev, T. H. Johansen, and A. E. Primenko. Avalanche-driven fractal flux distribution in nbn superconducting films. *Appl. Phys. Lett.*, 87:042502, 2005.

[132] I. Sobel and G. Feldman. A 3x3 isotropic gradient operator for image processing. Stanford Artificial Intelligence Project, 1968.